Spring 2016

Quantifying the role of the seed population in radiation belt dynamics

Alexander Boyd
University of New Hampshire, Durham

QUANTIFYING THE ROLE OF THE SEED POPULATION IN RADIATION BELT DYNAMICS

BY

ALEXANDER JUSTIN BOYD

B.A. in Astronomy & Physics, Boston University, 2010

DISSERTATION

Submitted to the University of New Hampshire

in partial fulfillment of

the requirements for the degree of

Doctor of Philosophy

in

Physics

May, 2016

This dissertation has been examined and approved in partial fulfillment of the requirements for the degree of Doctor of Philosophy in Physics by:

Dissertation Director, Harlan Spence
Director, Institute for the Study of Earth, Oceans and Space
Professor of Physics

Maurik Holtrop
Professor of Physics

Lynn Kistler
Professor of Physics

Marc Lessard
Associate Professor of Physics

Drew Turner
Member of the Technical Staff, The Aerospace Corporation

On December 21, 2015

Original approval signatures are on file with the University of New Hampshire Graduate School.

Acknowledgments

I'd like to start off by thanking my advisor Harlan Spence. I definitely consider myself lucky that you took a chance on me as an undergrad and stuck with me all these years. You were everything I could have asked for in an advisor, and I will always be grateful for the time, advice and support you gave me during this process.

To my thesis committee, thank you for your time and patience in this process. Your comments and suggestions certainly made this a better document.

I was lucky enough to work in a great and supportive research group. I'd like to thank Sonya Smith for always keeping me on task and for all the hard work she did to keep everything going smoothly. A very big thank you goes to Andrew Jordan, Chia-Lin Huang, Jody Wilson and Alex Crew. Whether it was discussing a paper, presentation or the witty lunch repartee, you were all a constant source of wisdom, support, encouragement and humor that I am very grateful for.

To my family, especially my parents and my grandpa, thank you for your continued love and support. Even if you didn't always understand what I was up to over the last few years, you were always there for me (as you always have been).

And finally, thank you to the love of my life, Luna. You've had to put up with more than anyone during the process, whether it was moving, dealing with science talk or living with a zombie while I was writing this thesis. It would be an understatement to say I couldn't have done this without you. You were a constant source of happiness, support, diversion and tough love when I needed it most. While I'm sure there were many times over the past

few years when you just wanted to punch me in the face, there was no one else I would have rather had by my side. I look forward to continuing on to our next adventure together.

The research at the University of New Hampshire presented here was supported by RBSP-ECT funding through JHU/APL contract 967399 under prime NASA contract NAS5-01072.

Table of Contents

List of Tables

List of Figures

ABSTRACT

QUANTIFYING THE ROLE OF THE SEED POPULATION IN RADIATION BELT DYNAMICS

by

Alexander Boyd

University of New Hampshire, May, 2016

The dynamics of the radiation belts depend on a delicate balance of source and loss processes. One such source process that has been shown to be effective is local acceleration, where 10s-100s keV seed electrons are accelerated via wave-particle interactions up to energies >1 MeV. Historically, much of the focus of radiation belt research has been on the dynamics of these >1 MeV electrons, and the role and importance of the seed electrons has been largely overlooked. In this thesis, we use phase space density calculated using data from the Van Allen Probes, to directly investigate seed population for a variety of events. We begin by presenting a case study of the 17 March 2013 event, providing some of the first clear observations of the seed population during a local acceleration event. Next, we present results from the first ever statistical study of the radiation belt seed population from the first 26 months of data from the Van Allen Probes. Finally, we examine all the pieces of the acceleration process together to determine what conditions produce effective radiation belt acceleration. Our results clearly demonstrate that the seed population plays a critical role in governing the dynamics of the higher energy radiation belt electrons.

Chapter 1

Introduction

1.1 Earth's Magnetosphere

The conditions of the local space environment around the Earth depend largely on the interactions between the sun and Earth's intrinsic magnetic field. Without an outside influence, Earth's magnetic field would be very similar to a simple magnetic dipole. However, the Earth is constantly bombarded by a stream of charged particles from the sun known as the solar wind. This impact of these solar wind particles causes the magnetic field to be compressed on the dayside, and stretched into a long tail on the nightside. This bullet shaped cavity in the solar wind that forms is known as the magnetosphere.

Within the magnetosphere, there are several different important regions and boundaries. Figure 1-1 shows a diagram of the magnetosphere with these major regions labeled. The outer edge of the magnetosphere, and the boundary between Earth's magnetic field and the solar wind is known as the magnetopause. On the dayside, the magnetopause location is typically $\sim$ 10 Earth radii (R_E), but this location can vary depending on the solar wind conditions [*Shue et al.*, 1998]. 3-4 R_E beyond the magnetopause lies the bow shock, a shock wave that is formed as the solar wind encounters Earth's magnetic field.

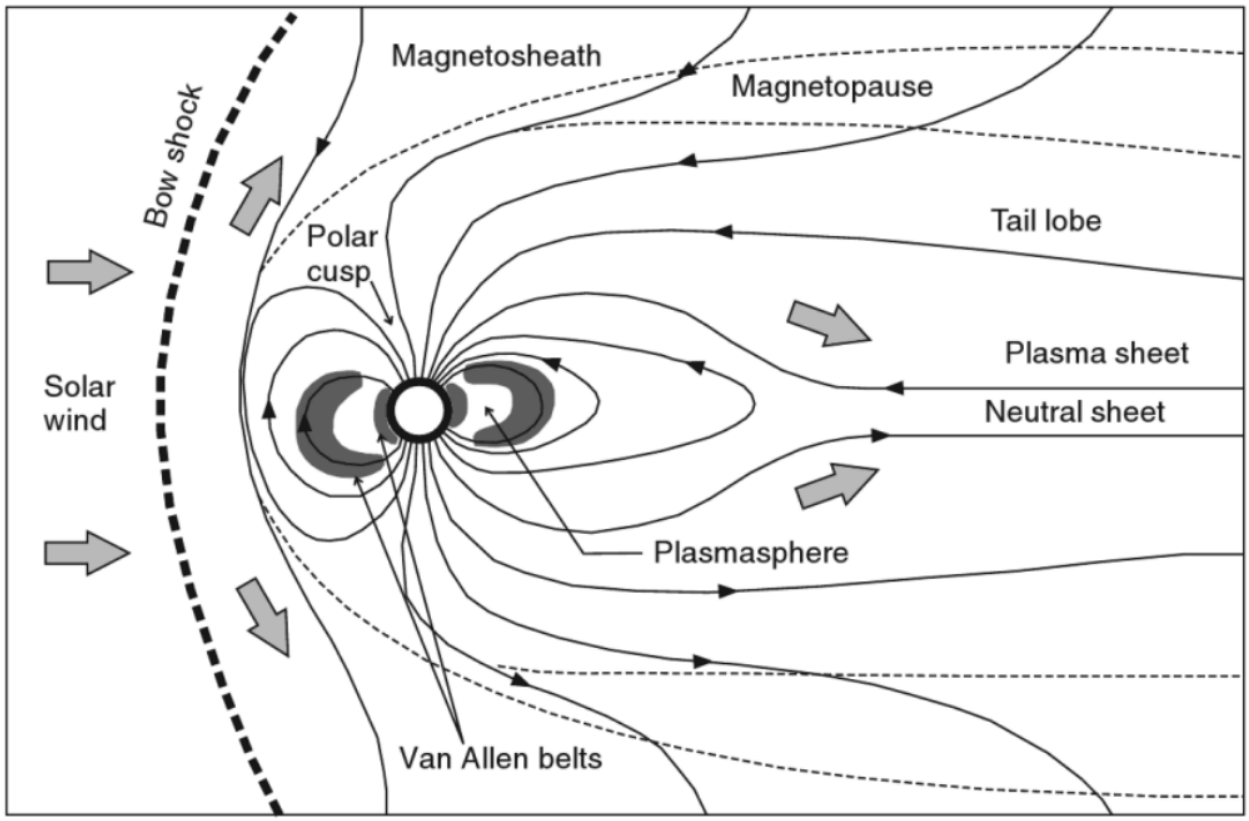

Figure 1-1: Figure from *Piel* [2011] depicting Earth's magnetosphere.

The nightside of the magnetosphere is dominated by the magnetotail, which stretches from ∼7 Earth radii (R_E) out to several hundred R_E. Spatially, most of the magnetotail is made up of the northern and southern lobes. These regions contain nearly parallel magnetic fields and have very low plasma densities (<0.01 cm^{-3}). In between the lobes lies the plasma sheet, a region with higher densities (0.1-1 cm^{-3}) of hot plasma (few keV ions and electrons). During geomagnetically active times, the plasma sheet serves as an important source of plasma for the inner magnetosphere [*Friedel et al.*, 2001]

The inner magnetosphere contains two major regions that overlap spatially, but differ greatly in their plasma properties. The first is the plasmasphere, a region of cold (∼eV) dense (10-1000 cm^{-3}) plasma that co-rotates with the Earth. The source of this plasma is the ionosphere, which is Earth's charged upper atmosphere. The other area of interest in the inner magnetosphere are the radiation belts. The belts are the focus of the remainder of this thesis, and will be discussed in detail in the following sections.

1.2 Van Allen Radiation Belts

The radiation belts were first discovered in 1958 by an experiment led by Dr. James Van Allen aboard Explorer I [*Allen and Frank*, 1959]. Although the experiment was designed to observe cosmic rays, it found an unexpected region of high energy particles trapped in Earth's magnetic field. In honor of their discovery, the regions have become known as the Van Allen radiation belts. Since their discovery, the radiation belts have been studied not only for their scientific interest, but also for the danger they pose to satellites. The energetic protons (10s MeV - few GeV) and electrons (100s keV - several MeV) in the radiation belts are capable of penetrating spacecraft shielding and causing severe damage up to and including spacecraft

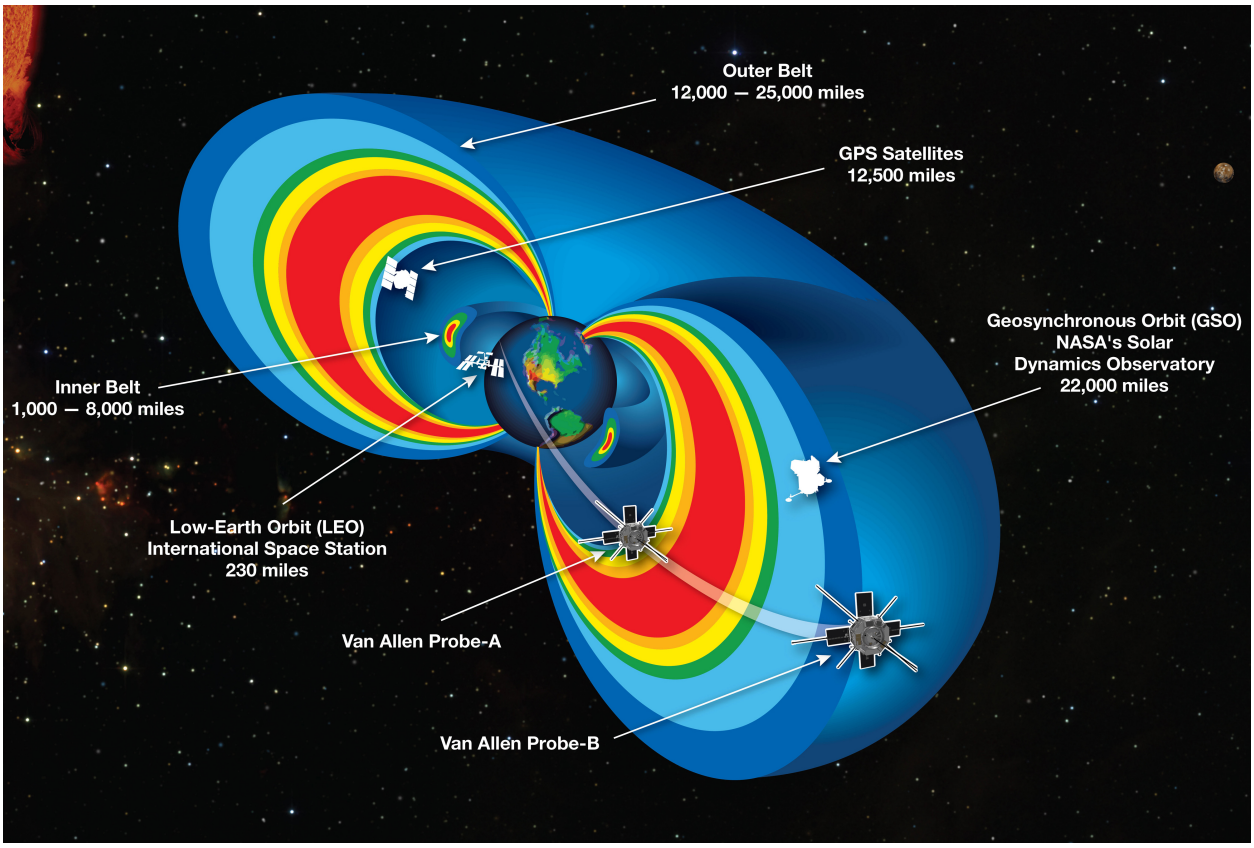

Figure 1-2: Radial cutaway of the radiation belts. Image courtesy NASA.

failure [*Lanzerotti*, 2001; *Baker*, 2002].

The nominal structure of the belts consists of two belts: an inner belt from 1.5-2.5 R_E and an outer belt from 4-7 R_E, separated by a narrow slot region. Figure 1-2 shows an illustration of this two belt structure. The two belts differ in both their composition and their variability. The inner belt is composed of high energy protons (10s MeV-few GeV) and lower energy electrons (<900 keV). Recent results from *Fennell et al.* [2015] have shown that the inner belt is completely devoid of higher energy electrons (>1 MeV). The protons in the inner belt are highly stable over long time periods, with lifetimes of several years [*Freden and White*, 1960]. The outer belt, on the other hand, is populated by high energy electrons (up to several MeV). It is also highly dynamic, with both the electron fluxes and the outer

boundary of the belt varying over the course of hours or days.

This variability becomes apparent when viewing long term observations of the outer belt. Figure 1-3 from *Li et al.* [2011] shows the 2-6 MeV electron flux from nearly 20 years of radiation belt observations by the Solar Anomalous and Magnetospheric Particle Explorer (SAMPEX). Figure 1-3 shows these fluxes as a function of L-shell, which is defined as follows:

$$r = L\cos^2(\lambda) \tag{1.1}$$

where λ is the geomagnetic latitude, and r is radial distance in Earth radii (R_E). L is a quantity that describes the equatorial radial distance of a field line mapped to a dipole. Therefore, a particle at L=5 is on a magnetic field line that crosses the magnetic equator 5 R_E from the center of the Earth. A location within the magnetosphere can be more completely described by also including magnetic local time (MLT), which describes azimuthal location, with 12 MLT (noon) facing sunward and 00 MLT (midnight) facing antisunward.

It is clear that the 2-6 MeV electrons shown in Figure 1-3 are highly dynamic, with fluctuations of more than 4 orders of magnitude. The timescales of these changes varies greatly, with gradual growth and decay over days and weeks and increases and dropouts that take place over less than a day. Many, but certainly not all, of these changes are associated with geomagnetic storms.

Renewed interest in resolving open mysteries of the radiation belts led to the recent launch of NASA's Van Allen Probes mission. The mission features a comprehensive suite of instruments to study the particles, waves and fields in the radiation belts. The spacecraft and their instrumentation are described in detail in Chapter 2. The overall goal of radiation belt research, and the main mission objective for the Van Allen Probes, is to understand the

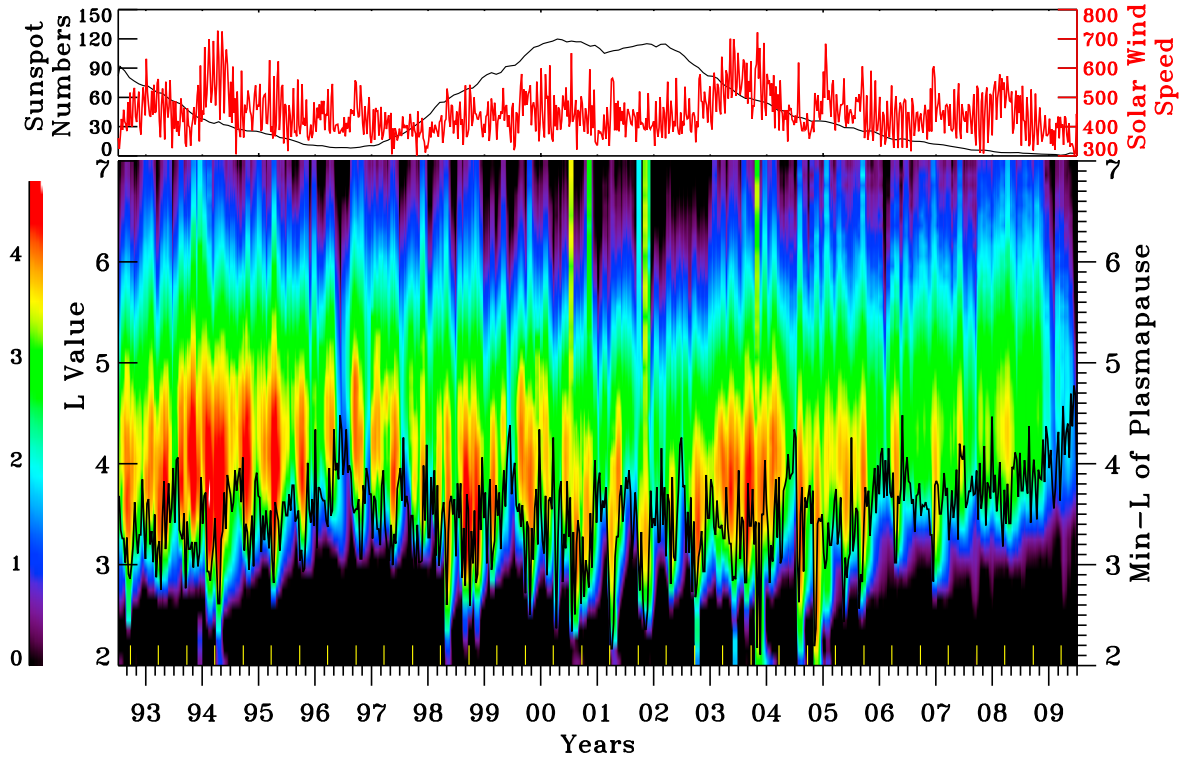

Figure 1-3: Figure from *Li et al.* [2011] showing 20 years of 2-6 MeV electron observations from SAMPEX as a function of L. The color scale on the main plot shows differential electron flux (#/cm^2-s-sr).

processes that generate the dynamics we see in the belts to the point that we can predict the response of the radiation belts. Even with nearly 60 years of research on the radiation belts, there are still many new discoveries and unanswered questions. One of the fundamental questions since the discovery has been how exactly radiation belt electrons are accelerated to such high energies. This thesis aims to address part of this wider question, and investigate the role that a lower energy (10s-100s keV) population of electrons, known as the 'seed' population, plays in the acceleration process.

1.3 Single Particle Motion

Before beginning a detailed discussion of radiation belt dynamics, it is important to review the motion of particles within the radiation belts. This will conclude in the derivation of the three adiabatic invariants μ, K and L^*, which play an important part of the phase space density calculation described in Chapter 2.

For charged particles moving in a magnetic field, the motion is described by the Lorentz force equation:

$$F = q(\vec{E} + \vec{v} \times \vec{B}) \tag{1.2}$$

where q and $\vec{v}$ are the particle's charge and velocity, and $\vec{E}$ and $\vec{B}$ are the electric and magnetic fields. The particle's velocity can be split into a component perpendicular to the magnetic field ($v_\perp$), and a component along the magnetic field ($v_\parallel$). The ratio of these velocity components define a particle's pitch angle α:

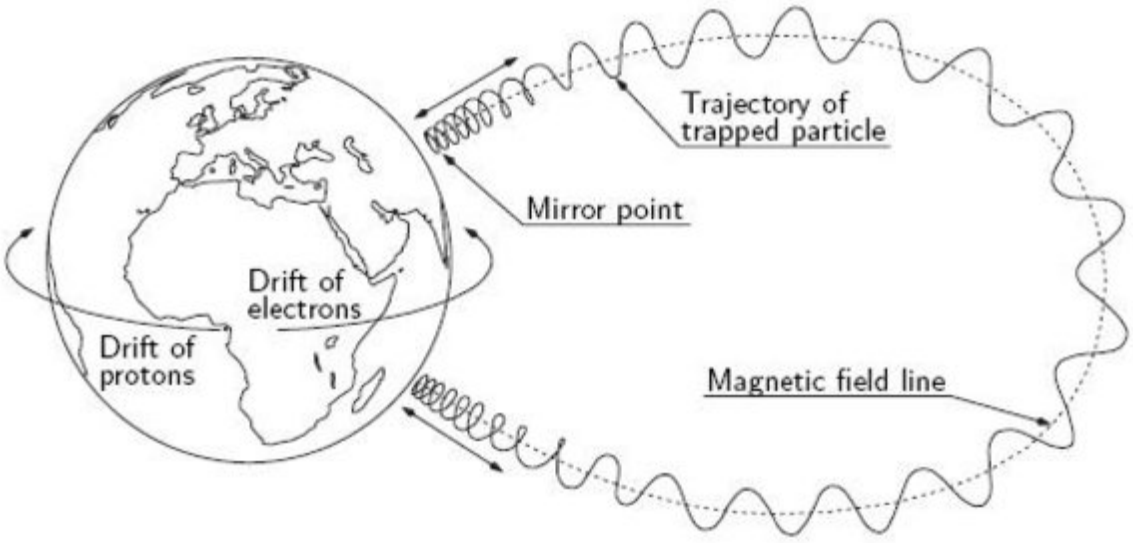

Figure 1-4: Diagram from *Baumjohann and Treumann* [2006] showing the gyro, bounce and drift motions of particles in Earth's magnetic field.

$$\alpha = \tan^{-1} \frac{v_\perp}{v_\parallel} \tag{1.3}$$

From equation 1.2, it is clear that the electric field only serves to accelerate the particle along the direction of the field. However, the magnetic field term leads to more complicated motions. As a result, in a quasi-dipole magnetic field like the Earth's, charged particles undergo three types of motion:

1. Gyration around the magnetic field line.

2. Bounce along the field line between magnetic mirror points.

3. Drift azimuthally around the Earth (eastward for electrons, westward for protons).

An illustration of these motions is shown in Figure 1-4. For radiation belt electrons, these motions have timescales on the order of milliseconds, seconds and tens of minutes respectively. Each of these motions has a corresponding adiabatic invariant, which is conserved

if the magnetic field varies slowly compared to these timescales. Following Hamiltonian mechanics, an adiabatic invariant of a periodic motion is given by the action integral J, integrated over a complete motion period [*Goldstein*, 1959]:

$$J = \oint p_i dq_i \tag{1.4}$$

where p is the canonical momentum and q is a generalized coordinate. The following sections describe the gyro, bounce and drift motions and the calculation of the associated invariants.

1.3.1 First Adiabatic Invariant

The gyro motion can be derived by starting with equation 1.2. If E = 0 and B is assumed to be homogeneous, the equation of motion becomes a harmonic oscillator. The particle rotates around the magnetic field with frequency Ω_g (known as the gyrofrequency) and radius r_g (known as the gyroradius):

$$\Omega_g = \frac{qB}{m} \qquad r_g = \frac{m_0 v_\perp}{|q|B} \tag{1.5}$$

Therefore, the particle gyrates around the magnetic field line at the above gyro frequency. To derive the first adiabatic invariant, the canonical momentum $p = m\vec{v} + q\vec{A}$, where $\vec{A}$ is the vector potential ($\vec{B} = \nabla \times \vec{A}$), is substituted into Equation 1.4, integrating over a single gyromotion:

$$J_1 = \oint (\vec{p} + q\vec{A}) \cdot d\vec{s} \tag{1.6}$$

Here, the integration is over a single gyromotion, so in the first term $\vec{p} \cdot d\vec{s} = p_\perp ds$. In addition, the second term can be rewritten using Stokes' theorem as follows:

$$J_1 = \int p_\perp ds + q \iint (\vec{\nabla} \times \vec{A}) \cdot d\vec{S}$$

$$J_1 = m_0 v_\perp \int ds + q \iint \vec{B} \cdot d\vec{S}$$

$$J_1 = m_0 v_\perp 2\pi r_g - qB\pi r_g^2$$

$$J_1 = \frac{\pi m_0^2 v_\perp^2}{qB} = \frac{2\pi m_0}{q}\mu$$

$$J_1 \propto \mu \tag{1.7}$$

$$\tag{1.8}$$

where m_0 is the particle mass and r_g is the gyroradius from Equation 1.5 and μ is the first adiabatic invariant, the magnetic moment, defined as:

$$\mu = \frac{p_\perp^2}{2m_0 B} \tag{1.9}$$

1.3.2 Second Adiabatic Invariant

The bounce motion arises as a consequence of the Earth's magnetic field geometry. A particle's $v_\parallel$ moves the particle along the magnetic field line. The Earth's magnetic field is stronger near the poles since the field lines are closer to the surface. Therefore, as a particle moves away from the magnetic equator it encounters a stronger magnetic field. Assuming the 1st invariant (Equation 1.9) is conserved, as the magnetic field increases, the energy associated with the particle's perpendicular velocity must also increase. Since the particle's

total energy is conserved, as the energy associated with the perpendicular velocity increases, the energy associated with the parallel velocity must decrease to compensate. This continues until the particle reaches a strong enough magnetic field field that $v_{\parallel} \to 0$. This point is known as the magnetic mirror point since the particle then reverses direction along the field line.

The location of the magnetic mirror point is dependent on the equatorial pitch angle. A particle will mirror when its local pitch angle is 90°. Therefore, particles with equatorial pitch angles near 90° mirror close to the magnetic equator, while particles with equatorial pitch angles near 0° or 180° will mirror far from the equator. If a particle's pitch angle is sufficiently small, its mirror point will lie inside the atmosphere. In this case, the particle will not mirror and will instead be lost due to interactions with the atmosphere. The critical angle where a particle is lost defines the 'loss cone', where all particles with smaller pitch angles are lost due to interactions with the atmosphere rather than mirroring.

The second invariant associated with the bounce motion J_2, can be found by substituting into equation 1.4, integrating over a single bounce motion:

$$J_2 = \oint p_{\parallel}\, ds = 2m_0 \int_{s_S}^{s_N} v_{\parallel}\, ds \tag{1.10}$$

where s_S and s_N are the southern and northern magnetic mirror points. This invariant describes the length of the particle's bounce motion along the magnetic field line. Assuming that 1st invariant μ is conserved, it is useful to decouple the first and second invariants and write the second invariant only in terms of the magnetic field. Using conservation of energy, along with the fact that $v_{\parallel} = 0$ at the mirror point, $v_{\parallel}$ at arbitrary location s can be expressed as follows:

$$W(s) = W_{mirror}$$

$$W_{\perp} + W_{\parallel} = W_{\perp_{mirror}}$$

$$\mu B(s) + \frac{v_{\parallel}^2}{2m_0} = \mu B_{mirror}$$

$$v_{\parallel} = \sqrt{2m_0\mu}\sqrt{B_{mirror} - B(s)} \tag{1.11}$$

where W is the particle's energy and m_0 is the particle mass. The second invariant K can therefore be written as:

$$K = \frac{J}{2\sqrt{2m_0\mu}} = \int_{s_S}^{s_N} \sqrt{B_{mirror} - B(s)}\, ds \tag{1.12}$$

1.3.3 Third Adiabatic Invariant

The third motion, the drift motion, occurs if there is a force acting on the particle perpendicular to the magnetic field line. The particle will then drift in a direction perpendicular to both the force and the magnetic field. In the case of the Earth's magnetic field, such forces are caused by the radial gradient of the magnetic field (towards the earth) and the curvature of the magnetic field lines. Both of these cause the particle to experience an inward radial force and therefore drift azimuthally around the Earth. Both the gradient and curvature drifts are charge dependent and point in the same direction, so they are often referred to collectively as the gradient-curvature drift. This causes electrons to drift eastward and ions to drift westward around the earth. The opposite motion of the charges generates a westward current in the equatorial plane known as the ring current. This current opposes the

magnetic field of the Earth. During geomagnetic activity, more particles are transported into the inner magnetosphere, strengthening the ring current and causing a decrease in strength of the Earth's dipole field measured by ground stations. This decrease is reflected in the disturbance storm time (Dst) index, which is commonly used to measure the strength of geomagnetic storms.

When all three of the particle motions (gyro, bounce and drift) are put together, the particle's path traces out a surface known as a drift shell. The third adiabatic invariant, which describes the total magnetic flux contained in a particle's drift shell is defined as follows:

$$\Phi = \oint \vec{B} \cdot d\vec{A} \tag{1.13}$$

For the radiation belts it is often more useful to use the dimensionless quantity L* [*Roederer*, 1970], defined below:

$$L^* = \frac{2\pi M}{\Phi R_E} \tag{1.14}$$

where M is the Earth's dipole moment and R_E is the radius of the Earth (6378 km). Since L* is inversely proportional to Φ, it also functions as an adiabatic invariant. In a dipole field, L* is equivalent to L (Equation 1.1). However, for a more realistic model of the Earth's magnetic field, particularly during active times, these two quantities can deviate greatly.

1.4 Wave Particle Interactions

1.4.1 Violation of Adiabatic Invariants

As mentioned earlier, each of these invariants has an associated timescale. For the 1st invariant, this is the timescale of the gyroperiod, which for a 1 MeV electron at geosynchronous orbit is ∼few milliseconds. For the 2nd invariant, this is the timescale of the bounce motion (∼few seconds). Finally, for the 3rd invariant this is the timescale of the drift motion (10s minutes). If the changes in the electric and magnetic fields are slower than these timescales, then these quantities are conserved. Much of the study of the radiation belts focuses on times when there is an irreversible increase in the relativistic electron flux, which can only occur when one or more of the invariants are violated. Therefore, putting observations in terms of these invariants provides a clearer picture as to whether an observed enhancement is caused by an adiabatic or an irreversible process.

One of the primary ways that these invariants can be violated is by wave-particle interactions. For violation of the 1st invariant, this is done by waves with frequencies close to the gyrofrequency. These types of waves, with frequencies between 1-30 kHz are know as very low frequency (VLF) waves. Similarly, for violation of second and third invariants, this is done by waves with periods close to the bounce and drift periods. These waves, with frequencies between 1 mHz - 1 Hz, are known as ultra low frequency (ULF) waves. In the following sections we will discuss these waves in more detail and describe how they interact with energetic electrons.

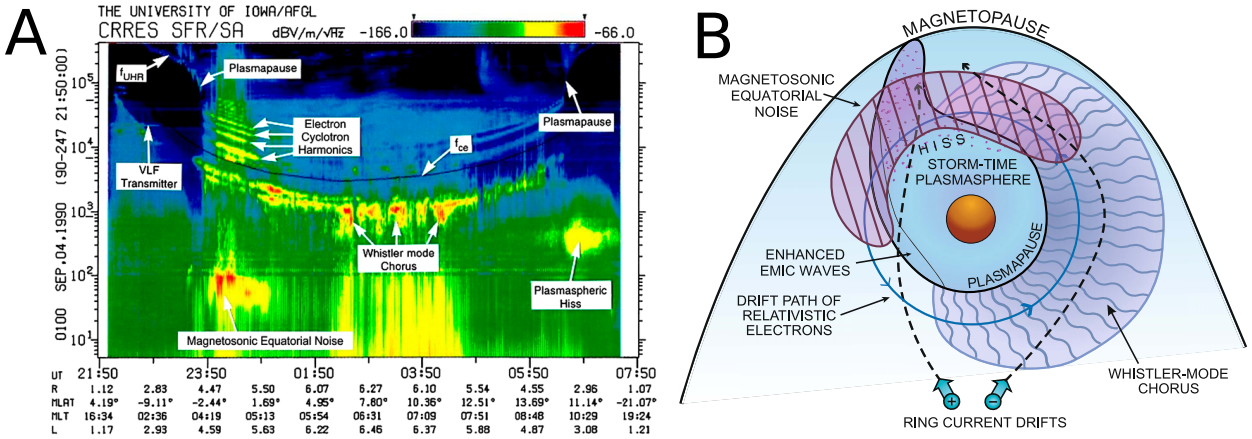

Figure 1-5: A) Figure from *Kletzing et al.* [2013] showing a wave spectrogram with the major VLF magnetospheric wave modes labeled. B) Figure from *Thorne* [2010] showing the locations within the magnetosphere that these wave are observed.

1.4.2 Magnetospheric Waves

As mentioned in the previous section, VLF and ULF waves can interact with energetic particles and violate one or more of the adiabatic invariants. The focus of this thesis will be on VLF waves and their interaction with energetic electrons. While their effects are important and will be discussed in the following sections, the exact details of these different wave types and how they are generated is beyond the scope of this thesis. For a review of ULF waves see *Menk* [2011].

Within the magnetosphere, there are several different types of VLF waves that can interact with energetic electrons. Figure 1-5A shows a spectrogram of the waves observed by the Combined Release and Radiation Effects Satellite (CRRES; a predecessor to the Van Allen Probes). The major types of waves that interact with energetic electrons including electron-cyclotron, magnetosonic, whistler-mode chorus, and hiss waves are labeled. Figure 1-5B shows the location of where these different wave types are observed within the magnetosphere.

The remainder of this thesis will focus on one type of VLF wave in particular, whistler-

mode chorus, since they play an important role in the acceleration of radiation belt electrons [e.g. *Thorne et al.*, 2013]. For a complete description of other wave types and their effects on radiation belt electrons see the review by *Thorne* [2010]. Chorus waves are circularly polarized right hand plasma waves with frequencies between ∼few 100 Hz and 10s kHz. Therefore, chorus waves are classified as VLF waves. They have been named whistlers for the distinctive descending tones the waves make when played as sound waves. The structure of chorus is dependent on the equatorial electron gyrofrequency (f_{ce}; Equation 1.5 for an equatorial electron), and typically occurs in two separate bands: a lower band between 0.1-0.5 f_{ce} and an upper band between 0.5-0.9 f_{ce} [*Tsurutani and Smith*, 1974]. An example of this two band structure can be seen between 23:50-1:50 on Figure 1-5A. As shown in Figure 1-5B, lower band chorus is predominately from pre-midnight to post-dawn in MLT and studies have shown that its occurrence is closely related to geomagnetic activity [*Li et al.*, 2011].

1.4.3 Gyro-resonance

When a particle encounters a plasma wave, it will interact strongly if the wave is Doppler-shifted with respect to its gyrofrequency. This resonance condition can be written as follows:

$$\omega - k_{\parallel} v_{\parallel} = \frac{n\Omega_g}{\gamma} \qquad n = 0, \pm 1, \pm 2, \pm 3... \tag{1.15}$$

where ω is the wave frequency, $k_{\parallel}$ and $v_{\parallel}$ are the wave number and particle velocity along the magnetic field, Ω_g is the gyrofrequency (Equation 1.5) and $\gamma = (1 - (v/c)^2)^{-1/2}$ is the relativistic correction factor. A diagram of the normal cyclotron interaction is shown in Figure 1-6. In this scenario, the wave and the particle both move along the field line in

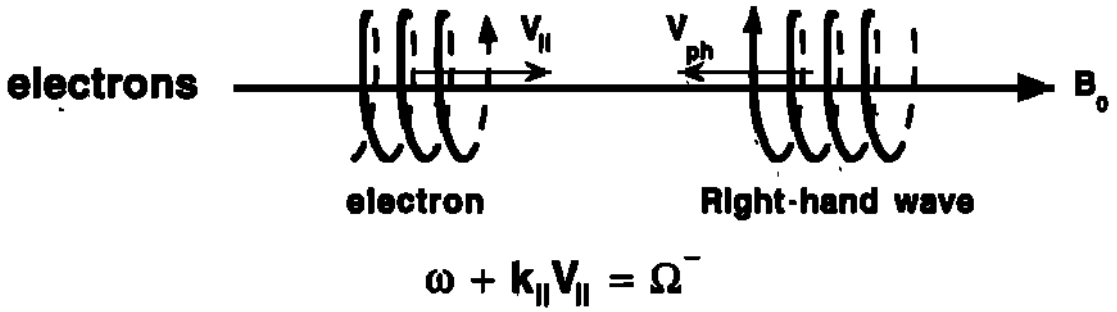

Figure 1-6: Figure from *Tsurutani and Lakhina* [1997] showing the normal cyclotron resonant interaction between electrons and right handed waves.

opposite directions and therefore propagate toward one another. While the particle encounters the wave, if the resonance condition is met, the particle experiences an electric field that accelerates (or decelerates) the particle.

This type of interaction violates the first invariant, leading to a changes in both particle energy and pitch angle [*Kennel and Petschek*, 1966]. If particle is accelerated, the wave transfers energy to the particle, causing the particle's pitch angle to move closer to 90°. If the particle is decelerated, the particle transfers energy to the wave, and the particle's pitch angle is scattered to smaller pitch angles. In some cases this can act as an important loss process if particles are scattered into the loss cone.

In either of these cases, the particle is exchanging energy with the wave. Therefore, the waves offer a medium to exchange energy between different particle populations, as the particles that lose energy help to drive wave growth that can then drive acceleration for other particles. The waves are highly localized phenomena, so the particles will encounter the waves during each drift orbit. Even if the energy gain for each interaction is small, if the waves persist for long enough, the particles can become energized over multiple drift orbits and gain a large amount of energy.

1.4.4 Bounce-Drift Resonance

In addition to the gyro-resonance condition described above, waves can also resonate with a particles bounce and drift motions, violating the second and/or third invariants. The bounce-drift resonant condition can be written as follows [*Southwood and Kivelson*, 1981]:

$$\omega_{wave} - m\omega_{drift} = N\omega_{bounce} \tag{1.16}$$

where N is an integer, m is the azimuthal wave mode number and ω_{wave}, ω_{drift}, and $\omega bounce$ are the frequencies of the wave, drift motion and bounce motion respectively. For electrons $\omega_{bounce} \gg \omega_{drift}$, so only the N=0 mode is a valid resonance condition [*Ozeke and Mann*, 2008]. This type of resonance is important for ULF waves, the impact of which will be discussed further in Section 1.5.1.

1.5 Radiation Belt Dynamics

It has long been known that radiation belt fluxes are correlated with solar activity [*Paulikas and Blake*, 1979]. This correlation can be clearly seen in Figure 1-3, which shows that belt properties correlate with sunspot number and related quantities such as solar wind speed over long time scales. On shorter timescales, this is especially true for geomagnetic storms, which often elicit a prompt response from the radiation belts. *Reeves et al.* [2003] analyzed geosynchronous data from 276 geomagnetic storms and compared the fluxes before and after each event. They found that the response of the radiation belt varied greatly from event to event, with 53% of the storms causing a net increase, 28% causing no change, and 19% causing a net decrease. These results are shown in Figure 1-7. They concluded that the

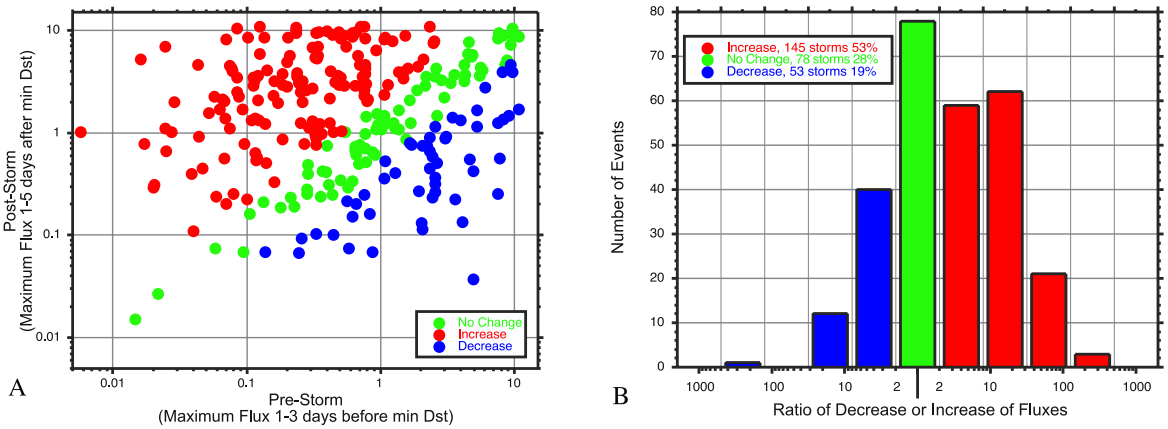

Figure 1-7: Figure from *Reeves et al.* [2003] showing statistics from 276 geomagnetic storms observed at GEO. The post and pre-storm fluxes were compared for each event. They found that 53% of the storms caused a net increase, 28% caused no change, and 19% caused a net decrease.

differences were due to the fact that the radiation belt's response to any given storm is the result of a delicate balance of source and loss processes.

There is a complex set of source and loss processes that act in the radiation belts. In the following sections, I will look separately at source and loss processes. It is important to note that effectiveness of a particular process can vary greatly from event to event. Also, these processes do not occur separately and often operate concurrently or in rapid succession, leading to the complex dynamics we see in the outer radiation belt, which makes predictability a challenge.

1.5.1 Loss Processes

There are several processes that can lead to the loss of radiation belt particles. *Millan and Thorne* [2007] provide a review of these loss processes for the outer radiation belt electrons. In addition to true loss processes, there can be apparent losses due to adiabatic effects. This is resolved by looking at phase space density (PSD) in adiabatic coordinates, which is

discussed in Chapter 2. True particle losses from the radiation belts have two possible sinks: precipitation loss into the atmosphere, and loss at the outer boundary of the magnetosphere (typically through the magnetopause).

As mentioned earlier, precipitation occurs when a particle's pitch angle is sufficiently close to 0° or 180° to be in the loss cone. This precipitation can occur slowly as particles are scattered into the loss cone by wave particle interactions with plasmaspheric hiss [e.g. *Lyons and Thorne*, 1972] (which is also responsible for the formation of the slot region between the radiation belts), electromagnetic ion cyclotron waves [e.g. *Thorne and Kennel*, 2012] or VLF chorus waves [e.g. *Thorne et al.*, 2005], which can also cause rapid bursts of precipitation known as a microbursts [e.g. *Lorentzen et al.*, 2001].

Losses through the magnetosphere can occur via a process known as magnetopause shadowing. During enhanced solar wind pressure (often during a geomagnetic storm), the magnetosphere is compressed and the magnetopause location moves closer to the Earth on a timescale shorter than a drift time. This results in particle's drift shell intersecting the magnetopause and connecting to open field lines in the solar wind. As the particle crosses the magnetopause, it is lost from the radiation belts. This process has been shown to be a rapid, highly effective loss process for radiation belt electrons [e.g. *Turner et al.*, 2012]. This loss can also be driven by outward radial diffusion pushing particles outside of the outer boundary [e.g. *Shprits et al.*, 2006].

1.5.2 Source Processes

Source processes operate by violating one or more of the adiabatic invariants (μ,K,L^*) in order to accelerate particles. Most of these processes fall into two broad categories: radial transport and local acceleration. *Friedel et al.* [2002] provides an overview of these and

other radiation belt source processes such as shock acceleration. While shock acceleration can be the dominant acceleration mechanism for certain events [e.g. *Li et al.*, 1993], it lies beyond the scope of this thesis and I will focus the discussion on radial diffusion and local acceleration.

The first type of radial transport source process is radial diffusion. Radial diffusion involves moving particles inward from the magnetotail into the radiation belts. This motion violates the third invariant while conserving the 1st and 2nd invariants. Since the first invariant is conserved, as the particles move to the stronger magnetic field in the inner magnetosphere, they are energized considerably. Much of the early work on the radiation belt acceleration focused on the effect of radial diffusion, which adequately explained the structure of the belts and long term variations that were observed in the belts [*Schulz and Lanzerotti*, 1974]. This diffusion can also be enhanced by interactions with ULF waves [e.g., *Rostoker et al.*, 1998; *O'Brien et al.*, 2001; *Mann et al.*, 2004; *Ukhorskiy et al.*, 2005]. This allows for more rapid, time variability seen during strong geomagnetic activity.

The other type of radial transport are energetic particle injections. Similar to radial diffusion, injections move particles from the magnetotail into the inner magnetosphere, but during an injection, the particles are transported significantly faster by electric fields. These injections are often associated with geomagentic substorms. The exact evolution of substorms is a complex and often controversial topic, but the basic phenomena that lead to an injection are as follows: During the early part of a substorm, magnetic reconnection allows solar wind plasma to enter the plasma sheet, adding energy to the magnetotail and causing the tail magnetic field to become more stretched. Eventually, the energy stored in the tail releases and the configuration of the magnetic field quickly becomes more dipole-like in a process known as dipolarization. This change in the magnetic field induces an electric field

that rapidly pushes particles into the inner magnetosphere. As the particles move into the stronger magnetic field of the inner magnetosphere they are energized due to conservation of the first invariant.

Once in the inner magnetosphere the particles begin to drift (electrons drift eastward, ions drift westward). Spacecraft near the injection region see all energies simultaneously, known as 'dispersionless' injection, whereas spacecraft further away see higher energies first since they drift faster, known as 'dispersed' injection. There has been considerable work [*Gabrielse et al.*, 2014, and references therein] looking at the injection region and dynamics. These injections have been shown to regularly inject particles up to 300 keV into the inner magnetosphere [*Baker et al.*, 1979], providing an ample source of 10s-100s keV electrons for subsequent acceleration.

The other type of process, and the focus of much of this thesis is known as local acceleration. Local acceleration processes accelerate the particles within the radiation belts by violating the 1st and/or 2nd invariants via wave-particle interactions with VLF (100s Hz - 10 kHz) waves. This process is capable of rapidly (less than a day) producing large radiation belt enhancements at low L-shells. However, observational challenges have historically made it difficult to definitively observe local acceleration in the radiation belts. This is due to the fact that flux observations alone are not enough to differentiate between radial diffusion and local acceleration. Clear phase space density measurements within the radiation belts, as discussed in Chapter 2, are required.

Local acceleration by VLF waves was first discussed by *Temerin et al.* [1994] and *Li et al.* [1997]. Up until that time, interactions with VLF waves were thought to be dominated by pitch angle scattering [e.g. *Lyons and Thorne*, 1972]. However, since that time, there has been considerable theoretical work and modeling that shows VLF chorus waves are capable of

accelerating radiation belt electrons [*Horne and Thorne*, 1998; *Summers et al.*, 2002; *Horne et al.*, 2005; *Summers et al.*, 2007; *Thorne et al.*, 2013]. There has also been observational evidence of local acceleration shown by *Green and Kivelson* [2004]; *Iles et al.* [2006]; *Chen et al.* [2007a]. However, these observations were limited to either high inclinations, or geostationary observations. Recently, *Reeves et al.* [2013] has presented the clearest observations to date of local acceleration using data from the Van Allen Probes during the 8-9 October 2013 storm.

1.6 Radiation Belt Seed and Source Populations

The theory of local acceleration by VLF chorus waves relies on the interaction of the waves with two populations of particles: the few-10s keV source population that generates the waves and the 10s-100s keV seed population that is accelerated by the waves. Both of the populations are transported into the inner magnetosphere by substorm injections. The pitch angle distribution of these injected particles are often strongly peaked at 90° [*Asnes et al.*, 2005]. VLF chorus waves are generated through electron cyclotron instability driven by anisotropic ($T_\perp/T_\parallel$) distributions of these few-10s keV source electrons [e.g. *Kennel and Petschek*, 1966; *Thorne et al.*, 1977]. As these particles are scattered, they transfer energy to the waves, driving wave growth. These waves generated by the source population can then resonate with higher energy particles, accelerating the particles up to higher energies.

As described earlier, the gyro-resonant interaction with chorus waves can either accelerate or decelerate particles. Lower energy particles (like those at source population energies) are predominantly scattered by the waves, whereas higher energies can experience rapid acceleration. As described by *Horne et al.* [2005], the anchor-point energy, above which

particles are accelerated faster than they are scattered is ∼300 keV. Therefore, the 100s keV seed electrons, which are supplied by substorm injections can be accelerated by the chorus waves up to higher energies.

The idea of a radiation belt seed population was first discussed in *Baker et al.* [1997] and *Baker et al.* [1998], which laid out a two step process where substorm injections bring 10s-100s keV seed electrons into the inner the magnetosphere, followed by subsequent acceleration via wave particle interactions. This was followed by *Meredith et al.* [2001] which showed that chorus wave occurrence was strongly related to substorm activity and the injection of keV electrons. They concluded substorm injections were vital to drive the sustained chorus emissions to allow for acceleration. Overall, the work of *Meredith et al.* [2001, 2004] and *Li et al.* [2009] conclude that substorms, rather than storms, play a critical role in the development of the outer radiation belt population. This idea will be revisited and discussed in Chapter 5.

1.7 Focus Questions

The overall objective of this thesis is to understand the role and ultimately the importance of the seed population in radiation belt dynamics. While the theory behind the seed population and VLF wave acceleration has been well developed, clear observations of the seed population in the radiation belts have been very limited. This thesis aims to leverage the data from the Van Allen Probes to study the radiation belt seed population through a series of focus questions:

1. Is it possible to directly observe and quantify the seed population's role in the acceleration of radiation belt electrons?

2. What correlations and causal relationships are there between enhancements in the seed population and enhancements in the core population?

3. How do differing inputs of source and seed electrons lead to acceleration (or lack thereof) in the radiation belts?

4. Can the seed population be used to predict enhancements in the core population?

In the next chapter, I will discuss the Van Allen Probes mission and the calculation of phase space density. The remaining chapters will use that dataset to address each of first three questions in detail. This will lay the framework for a discussion of the final question, which is the ultimate goal of the work presented here.

Chapter 2

Phase Space Density

2.1 Motivation

One of the main goals of this thesis is to understand the role that the seed population plays in radiation belt acceleration. In addition to acceleration and loss process, electrons within the outer belt also experience adiabatic changes. For example, as particles move slowly inward they experience a stronger magnetic field and will therefore experience an increase in energy if their first adiabatic invariant is conserved. Additionally, particles can move adiabatically away from a spacecraft and no longer be observed. When only looking at particle fluxes, these types of changes can appear as either enhancements or losses, even though the particles have only undergone adiabatic changes. In order to get a more clear picture of what is going on in the radiation belts, we need to look at phase space density (PSD) in adiabatic coordinates (μ, K, L^*). Liouville's theorem indicates that phase space density is conserved along any trajectory in invariant space so long as there are no sources or sinks. Therefore, we will explore PSD to quantify potential sources (e.g., acceleration events) or sinks (e.g., precipitation) within the system. Doing so removes the adiabatic effects, making it easier in our case to examine the acceleration of particles at different energies.

Studies using PSD to study isolated events have been around for some time [*Selesnick et al.*, 1997; *Selesnick and Blake*, 1997; *Hilmer et al.*, 2000; *Green and Kivelson*, 2004]. However, the challenges of calculating and interpreting PSD have made it difficult to implement robustly and definitively. The quality data from recent missions such as THEMIS and the Van Allen Probes along with recent studies such as *Reeves et al.* [2013] have helped to make PSD a viable and important tool for studying radiation belt dynamics. The goal of this chapter is to completely describe the phase space density (PSD) data product for the Van Allen Probes that will be used in each of the subsequent chapters. This includes a description of the Van Allen Probes instrumentation, the calculation of PSD, applications of PSD and a summary of error analysis techniques.

2.2 Van Allen Probes

The twin Van Allen Probes (originally known as Radiation Belt Storm Probes (RBSP)) spacecraft launched on 30 August 2012 with the goal to study the radiation belts. The probes were launched in low inclination, highly elliptical orbits with apogees near 5.8 R_E and perigees at $\sim$ 700 km. The orbital period is $\sim$9 hours, allowing both spacecraft to offer nearly continuous observations of both the outer and inner belt. The spacecraft spin at a cadence of 11 seconds, allowing the particle instruments to measure pitch angle-resolved fluxes.

The overall objective of the mission is to: 'Provide understanding, ideally to the point of predictability, of how populations of relativistic electrons and penetrating ions in space form or change in response to variable inputs of energy from the Sun' [*Mauk et al.*, 2014]. To address this goal, the Van Allen Probes feature a comprehensive instrument suite to study

the particles, fields and waves in the radiation belts. These instruments suites include:

- Energetic Particle Composition and Thermal Plasma Suite (ECT; *Spence et al.* [2013b]), which consists of three instruments and provides measurements of energetic electrons and ions (1 eV - 10s MeV).
- Radiation Belt Storm Probes Ion Composition Experiment (RBSPICE; *Mitchell et al.* [2013], which provides measurements of energetic electrons and ions (20 keV - 1 MeV).
- Relativistic Proton Spectrometer (RPS; *Mazur et al.* [2013]), which provides measurements of highly relativistic protons (50 MeV - 2 GeV).
- Energetic and Magnetic Field Instrument Suite and Integrated Science (EMFISIS; *Kletzing et al.* [2013]), which provides measurements of the magnetic field and plasma waves.
- Electric Field and Waves instruments (EFW; *Wygant et al.* [2013], which provides measurements of the electric fields.

This thesis will largely focus on data from two of the instruments in the ECT suite, Magnetic Electron Ion Spectrometer (MagEIS; *Blake et al.* [2014]) and the Relativistic Electron Proton Telescope (REPT; *Baker et al.* [2013]). We will now describe the operations of those instruments in detail.

2.2.1 Magnetic Electron Ion Spectrometer (MagEIS)

The MagEIS instrument actually consists of four separate instruments on each spacecraft. These are a low energy unit (20-240 keV), 2 medium energy units to provide additional pitch angle coverage (M35 and M75; 80-1200 keV), and a high energy unit (800-4800 keV).

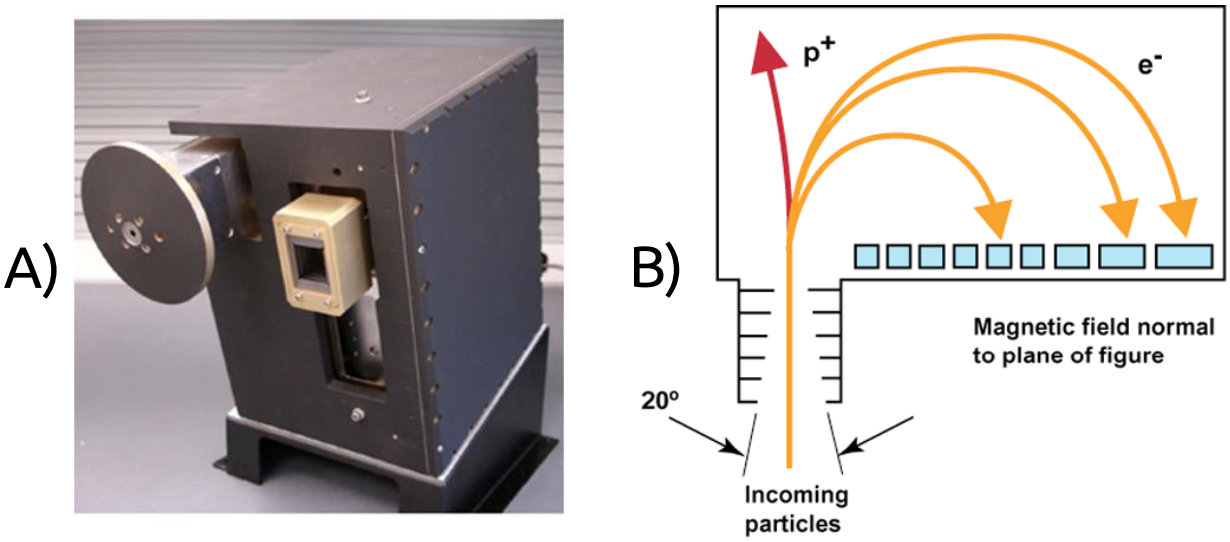

Figure 2-1: Figure from *Blake et al.* [2014] showing the one of the MagEIS instruments (Panel A) and a diagram of how the instrument operates (Panel B). A large magnet produces a magnetic field into the page directs electrons on the detector array.

Together these instruments provide pitch angle resolved particle fluxes for electrons with energies of 20-4000 keV. The LOW, M75, and HIGH units provide identical pitch angle coverage, so for the work presented here, data from the M35 unit will not be used. A picture of one of the instruments is shown in Figure 2-1A.

As the instrument name suggests, MagEIS uses a strong magnet (550, 1600, and 4800 Gauss for the LOW, MED, and HIGH units, respectively) to create a magnetic field to direct electrons into the detector array. The curvature of the particle is dependent on the particle energy, so it allows the magnet to direct different energies to the appropriate detector. In addition the magnet allows for separation of ions and electrons, since the protons gyrate in the opposite direction from electrons. The electrons are directed onto a series of detectors whose thicknesses are matched to the expected energy based on the radius of curvature. A diagram of how the instrument works is shown in Figure 2-1B. The magnet strength is the

Figure 2-2: Picture of the REPT instrument.

primary reason for having 4 instruments as different energy ranges require different strength magnets.

During certain times in the orbit, penetrating protons in the inner zone and Bremsstrahlung X-rays in the outer zone can lead to elevated background counts that can dominate over the foreground electrons. The MagEIS data recently underwent an extensive overhaul to remove these background counts, described in *Claudepierre et al.* [2015]. While this correction has greatly improved the data quality, it does come with some caveats. There are many times when the background correction is more than 100% of the measured fluxes. In these cases the corrected fluxes are set to 0, even though this does not necessarily indicate that the actual flux is 0. Additionally, when the instrument operates in high-rate mode (which offers significantly higher pitch angle resolution), the background correction cannot be performed.

2.2.2 Relativistic Electron Proton Telescope (REPT)

The REPT instrument measures the higher energy (2 - 20 MeV) electrons in the radiation belt. The instrument consists of a stack of silicon solid state detectors, a collimator and a

thick aluminum and tungsten casing to shield the detectors. Figure 2-2 shows an image of one of the REPT instruments. The detector stack is able to stop electrons with energies up to 10 MeV, so measuring the penetration of incident particles gives a measure of the electrons incident energy. The lowest energy channels in the REPT instrument overlap with the MagEIS HIGH unit, allowing for inter-calibration between the two instruments. This inter-calibration has been an ongoing effort and at the time of this thesis, the fluxes from each instrument generally differ by less than a factor of 2 in the overlap region (energies of $\sim$ 1 MeV). The following sections describe the conversion of these fluxes into phase space density.

2.3 PSD Calculation

The goal of this calculation is to transform a differential particle flux $j(E, \alpha, x, t)$, as a function of energy (E), pitch angle (α), and position (x) into phase space density $f(\mu, K, L^*, t)$ as a function of the three adiabatic invariants μ, K and L^*. The calculations described here build on the work of *Chen et al.* [2005], *Chen et al.* [2007a], *Turner and Li* [2008] and *Turner et al.* [2012], but have been tailored and refined to use data from the Van Allen Probes. While very detailed, the calculation can be broken down into three basic steps:

1. For each energy channel at each time-step, convert the differential flux into phase space density.

2. For each desired K value, match the K to a measured pitch angle. Then, for each energy channel, fit the pitch angle distributions and extract the proper PSD values, giving an energy spectrum. Finally, at each time step, match the measured pitch angle to the calculated L^* value.

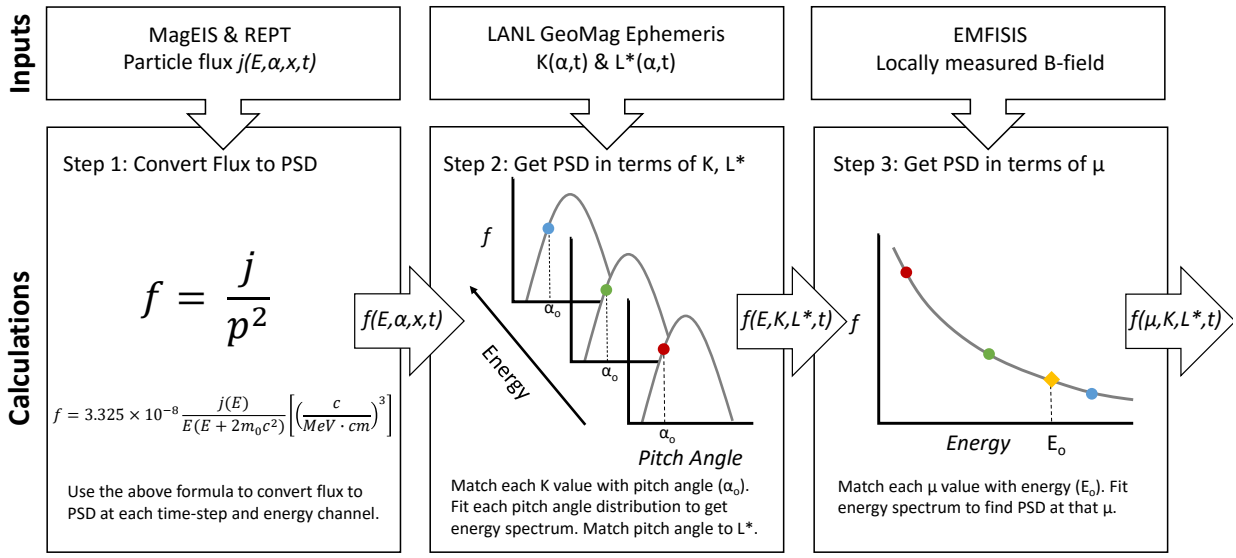

Figure 2-3: Diagram depicting each step of the PSD calculation The calculation begins with differential particle flux $j(E, \alpha, \vec{x}, t)$ and ends with PSD $f(\mu, K, L^*, t)$.

3. For each desired μ value, match the μ to an energy value. Fit the energy spectrum and extract the proper PSD for that μ and K.

These steps are illustrated in Figure 2-3. Due to the quality of the observations from the Van Allen Probes, every effort was taken to remain as true to the data as possible. Each of these calculation steps will now be described in detail.

2.3.1 Flux to PSD Conversion

Phase space density f is related to differential particle flux j by the following equation:

$$f = \frac{j}{p^2} \tag{2.1}$$

Inserting the relativistic expression for momentum for p and inserting a numerical factor

to convert the units to the GEM (Geospace Environment Modeling) unit of $(\frac{c}{MeVcm})^3$ [*Chen et al.*, 2005; *Green and Kivelson*, 2004], the equation becomes:

$$f = 3.325 \times 10^{-8} \frac{j(E)}{E(E + 2m_o c^2)} [(\frac{c}{MeVcm})^3] \tag{2.2}$$

where $j(E)$ is the differential particle flux with units of $\#/s \cdot sr \cdot cm^2 \cdot keV$, $m_o c^2$ is the rest mass of the electron and E is the energy value for each the energy channels, defined as follows:

$$E = \sqrt{E_{min} * E_{max}} \tag{2.3}$$

where E_{min} and E_{max} are respectively the minimum and maximum energies covered by an energy channel. As shown by *Chen et al.* [2005], this form offers improved accuracy over the mean energy, which tends to overestimate the calculated value of PSD.

These pitch angle resolved fluxes used in this calculation come from both the MagEIS and REPT instruments. All of the fluxes are binned into 5-minute averages in order to improve counting statistics. Additionally, since MagEIS uses dynamic energy channels, the fluxes are interpolated onto a common set of energies. These fluxes at each energy channel and pitch angle are used in Equation 2.2 to get PSD, $f(E, \alpha, \vec{x}, t)$.

2.3.2 Pitch Angle Fitting

In order to get PSD in terms of 2nd invariant K and 3rd invariant L^*, $K(\alpha,t)$ and $L^*(\alpha,t)$ are needed. For the Van Allen Probes mission, these quantities are calculated by the ECT Science Operations Center (SOC) using the LANLGeoMag model [*Henderson et al.*, 2011]. LANLGeoMag numerically solves a particle's guiding center equation of motion in the TS04D

global magnetic field model [*Tsyganenko and Sitnov*, 2005] to calculate a variety of relevant quantities, including $K(\alpha, t)$ and $L^*(\alpha, t)$.

At each time step a linear interpolation is applied to $K(\alpha)$ in order to get $\alpha(K)$. Therefore, each desired K value maps to a pitch angle. This pitch angle value also allows PSD to be tied to the proper L^* value, using the provided $L^*(\alpha, t)$.

Next, the pitch angle distributions for each energy need to be fit in order to find the PSD at the proper pitch angle to get $f(K)$. Many previous studies use a function of the form sin^n to fit the pitch angle distributions. For the Van Allen Probes data there are many times when this type of function offers a very poor fit. Therefore for this calculation, we use a linear interpolation in order to stay as true to the data as possible. Choosing the proper value from the pitch angle interpolation at each energy channel then gives an energy spectrum ($f(E, K, L^*)$) at each time-step.

2.3.3 Energy Spectrum Fitting

Given the particle kinetic energy E, pitch angle α, and the locally measured magnetic field B from EMFISIS, the first invariant μ is defined as:

$$\mu(E, B) = \frac{E(E + 2m_0c^2)sin^2(\alpha)}{2Bm_0c^2}[\frac{MeV}{G}] \tag{2.4}$$

where m_0c^2 is the electron rest mass. Table 2.1 shows the mapping between various μ and energy values at different L^*. Table 2.1 clearly demonstrates that both the MagEIS and REPT measurements are needed to cover different parts of μ-space over a range of L^*. At very high or low values of μ, the measurements from a single instrument are sufficient. However, to explore dynamics for μ between $\approx$ 500 and 3500 MeV/G across the outer

μ [MeV/G]	L^*=3.0	L^*=3.5	L^*=4.0	L^*=4.5	L^*=5.0	L^*=5.5
50	0.421	0.277	0.185	0.127	0.090	0.070
75	0.572	0.383	0.262	0.182	0.130	0.102
100	0.704	0.479	0.331	0.232	0.168	0.132
150	0.933	0.646	0.455	0.324	0.237	0.189
200	1.130	0.792	0.564	0.408	0.301	0.241
300	1.466	1.044	0.756	0.554	0.416	0.336
400	1.753	1.260	0.921	0.683	0.518	0.422
500	2.007	1.452	1.070	0.800	0.610	0.500
600	2.238	1.627	1.206	0.906	0.696	0.573
800	2.650	1.940	1.449	1.099	0.851	0.705
1000	3.014	2.218	1.666	1.271	0.990	0.825
1500	3.791	2.811	2.130	1.641	1.292	1.084
2000	4.447	3.314	2.524	1.956	1.550	1.307
2500	5.027	3.758	2.873	2.235	1.779	1.506
3000	5.551	4.160	3.189	2.489	1.987	1.687
3500	6.033	4.530	3.480	2.723	2.179	1.853
4000	6.482	4.874	3.751	2.940	2.358	2.009

Table 2.1: Table showing the energy that relates to given μ values at several L^* values. The calculation was performed for 90° pitch angle particles and for the average magnetic field values at each L^*. All energies shown have units of MeV. The red shaded boxes indicate when the energy lies in the range of the REPT instrument. The unshaded boxes are in the range of the MagEIS instrument.

belt ($3.0 < L^* < 5.5$), measurements from MagEIS and REPT must be combined. This underscores the importance of the cross-calibration of MagEIS and REPT.

If Equation 2.4 is rewritten to give E(μ):

$$E(\mu, B) = -m_0c^2 + \frac{1}{2}\sqrt{\frac{8\mu B m_0 c^2}{sin^2(\alpha)} + 4m_0^2c^2} \tag{2.5}$$

At each time-step, the energy spectrum $f(E, K, L^*)$ is fit using a uni-variate spline. Using Equation 2.5, for each μ value, the correct energy is selected to complete the calculation and give $f(\mu,\ K,\ L^*)$. As an important note, the spline fit is not used to extrapolate. If the energy falls below the lowest energy channel or above the highest energy channel, the value is not used.

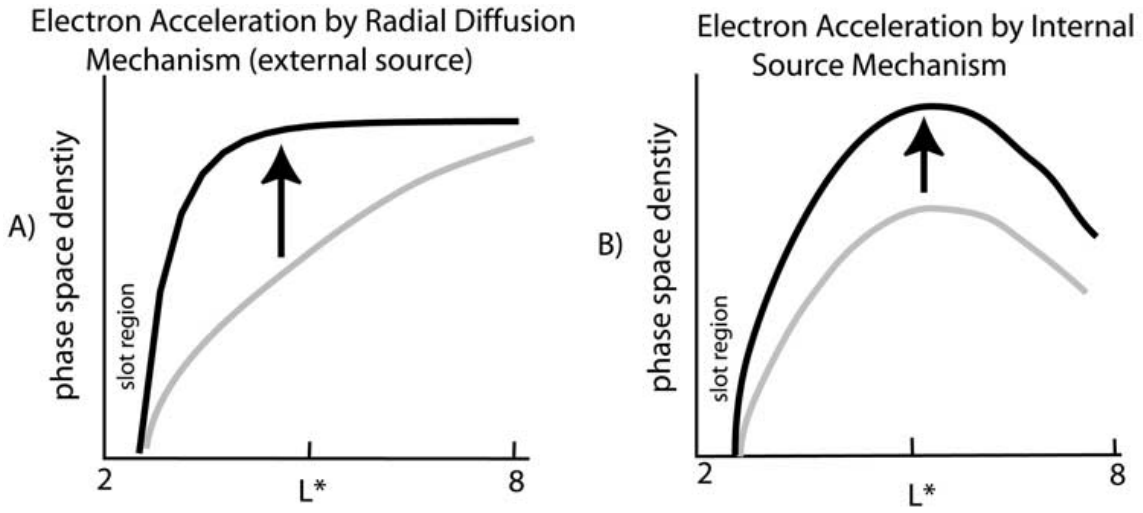

Figure 2-4: Figure from *Green and Kivelson* [2004] depicting the different signatures of radial diffusion (Panel A) and local acceleration (Panel B).

2.4 Using Phase Space Density

2.4.1 Distinguishing Acceleration Sources

One of the main uses for PSD is to distinguish between radial diffusion and local acceleration. Figure 2-4 from *Green and Kivelson* [2004] depicts the signatures for each of the acceleration processes. Radial Diffusion has a source at high L^*, so the PSD profile increases or remains constant toward higher L^*. Local acceleration has a source at low L^*, so a peak develops in PSD that increases with time. As noted in *Green and Kivelson* [2004], diffusion eventually smooths out peaks that develop in PSD.

These simple criteria for identifying different acceleration processes does come with some caveats. While a peaked distribution is indicative of local acceleration, there are other processes that can produce peaked PSD distributions. For example, a loss at large L^* can produce a peaked distribution even though no local acceleration had taken place. Therefore, growing PSD peaks at a fixed L^* value need to be observed to indicate local acceleration.

However, even if growing peaks are observed, great care must be taken to eliminate other possible sources for the observations. One of the few examples of another process that can also produce growing peaks is that of an on-off source at high L^*. Therefore observations at high L^* are needed to constrain this possibility and show that there is a source at low L^*.

An excellent example of local acceleration exhibited by growing PSD peaks comes from *Reeves et al.* [2013], which looked at the 8-9 October 2012 storm. The radial PSD profiles from that event are shown in Figure 2-5. The peaked distribution begins to develop on the 3:32 pass on 9 October. The peak continues to grow for the next 10 hours until outward radial diffusion smooths out the peak. In the supplementary material, *Reeves et al.* [2013] goes to great lengths to show that: 1) the peaks are significant compared to the errors produced by the magnetic field and 2) The PSD beyond the Van Allen Probes orbit has a negative gradient throughout the event, eliminating the possibility of an on-off source producing the growing peaks.

2.4.2 Van Allen Probes Limitations

While the quality of the observations from the Van Allen Probes is unprecedented, the orbital configuration of the spacecraft leads to several limitations in adiabatic invariant space. The first is that the L^* of the spacecraft apogee is often limited to $L^* < 5$, particularly during active times. This can cause uncertainly in identifying the acceleration mechanism if the PSD profile appears to be peaked at or near apogee. The second limitation is on second invariant K. While the Van Allen Probes' orbit is near the magnetic equator, the spacecraft do spend a significant amount of time off of the equator. Therefore, it is not possible to see all K values (particularly near K=0) at all times. As was shown in *Reeves et al.* [2013], $K = 0.11\ \ \mathrm{R_E G^{1/2}}$ is the smallest K value that allows for coverage at nearly all L^* values.

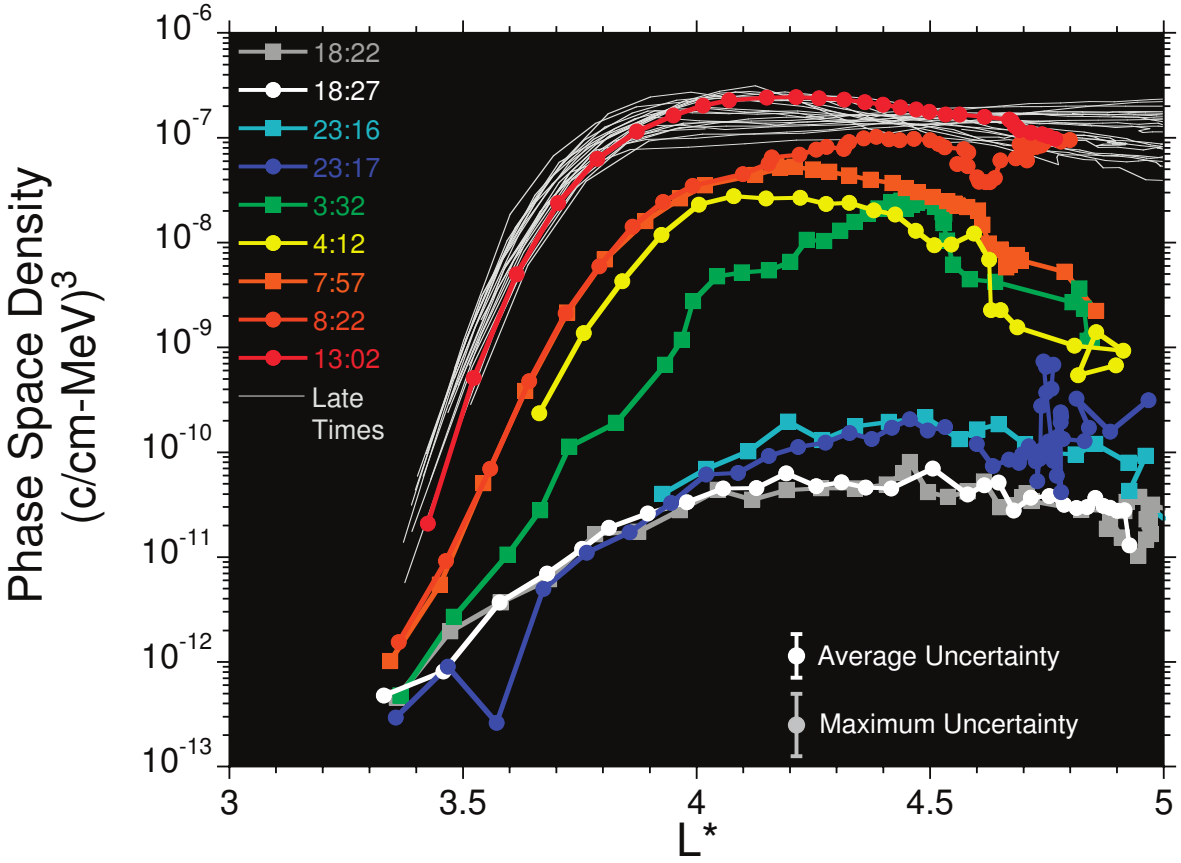

Figure 2-5: Figure from *Reeves et al.* [2013] show growing PSD peaks (μ = 3433MeV/G, K = 0.11 $R_E G^{1/2}$) during the 8-9 October 2012 Storm. All times shown are the L^*=4.2 crossing times.

2.5 Error Estimation

The error in the PSD calculation largely comes from errors in the calculation of K and L^* from the global magnetic field models. *Green and Kivelson* [2004] offers a complete discussion of how these errors can affect the interpretation of PSD results. Previous studies have utilized different techniques to attempt to estimate the error in the PSD calculation. *Turner et al.* [2012] estimated the error in the THEMIS PSD calculations by calculating the error in pitch angle measurements and carrying these errors though the PSD calculation. *Chen et al.* [2007a,b] utilized the technique of phase space density matching for the calculation of PSD for the LANL geosynchronous satellites. This technique was later used for the Van Allen Probes by *Morley et al.* [2013] and will be the used throughout this thesis to estimate errors.

Phase space density matching works on the application of Liouville's theorem, which states in the absence of sources or losses, phase space density should be constant. Therefore, during magnetic conjunctions of two spacecraft (looking at the same μ,K and L^*), the spacecraft should observe the same value for PSD. Assuming the spacecraft are well calibrated, any differences in the measured PSD are a result of errors in K or L^*, or a source or loss operating during the conjunction [*Morley et al.*, 2013]. This technique gives an estimate of the errors from the global magnetic field model, which can produce large errors in the PSD calculation [*Green and Kivelson*, 2004].

As suggested above, the PSD matching technique requires at least two separate and well calibrated measurements to be effective. Fortunately, PSD matching is a particularly effective technique for the Van Allen Probes, since the instruments are well calibrated and the dual spacecraft frequently overlap in adiabatic invariant space. [*Morley et al.*, 2013] presents phase space density matching results from the REPT instrument for the 8-9 October 2012

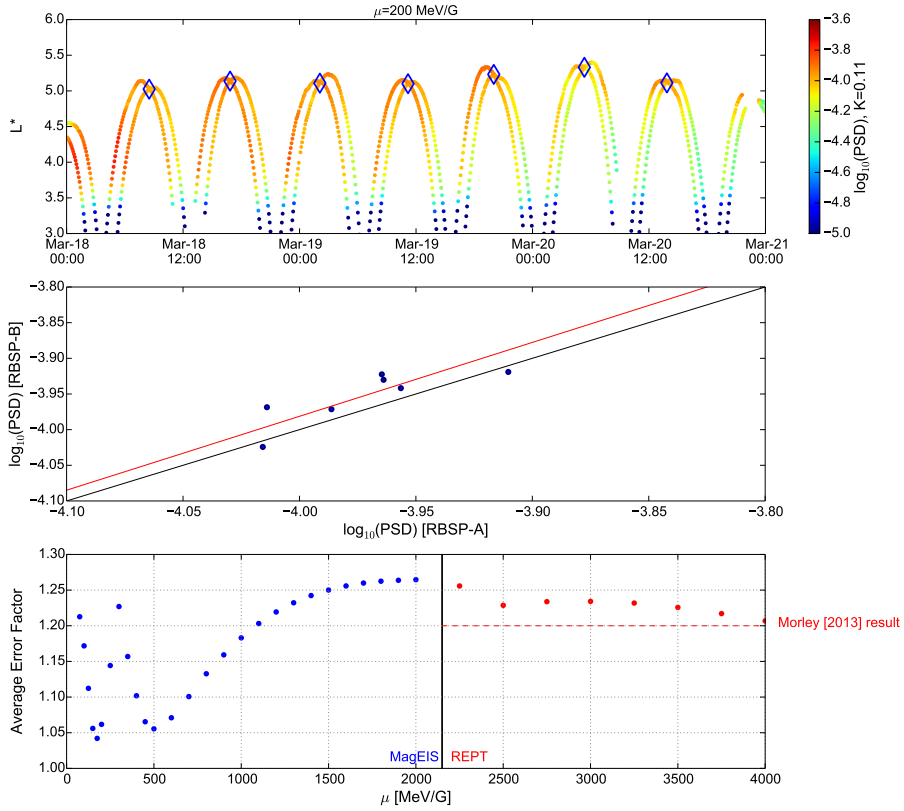

Figure 2-6: PSD matching results from 17 March 2013 Storm. Top panel shows PSD as a function of time for μ=200 MeV/G and K=0.11 $R_E G^{1/2}$. Conjunctions in K and L^* are denoted with blue diamonds. Middle panel shows the PSD matching results from each of the conjunctions. The red line is the best-fit line and the black line shows y=x. The bottom panel shows the average error factor as a function of 1st invariant μ. The average error from *Morley et al.* [2013] is shown with a dashed red line.

storm. Using the techniques described in *Morley et al.* [2013], the PSD matching results for the 17 March 2013 storm are shown in Figure 2-6.

Morley et al. [2013] tested several magnetic field models and found that the TS04D magnetic field model gave the smallest errors, with an average error of a factor of 1.2 for the 8-9 October 2012 storm. This technique was used to generate the error bars seen in *Reeves et al.* [2013]. PSD matching was able to show that the errors were smaller than the observed PSD peaks. This same technique is used in Chapter 3 for the 17 March 2013 event, a critical

element in the analysis that quantifies the significance of the peak determination and hence that local acceleration is operative.

2.6 Studies using Phase Space Density

The Van Allen Probes PSD data product I produced as part of this thesis have been used to enable several science studies beyond those described in the subsequent chapters. The first is *Li et al.* [2014] which modeled radial diffusion during March 2013. The PSD product that I derived from the ECT and EMFISIS data served as the outer boundary condition for the model and provided a data-model comparison to check how well the model performed. In general the model performed very well until 17 March 2013, when the model underestimated the PSD. This supports the conclusion that radial diffusion was the dominant mechanism leading up to the 17 March 2013 event, when local acceleration dominated. The next study in which the key PSD data product I developed was used is in *Foster et al.* [2015] which looked at the shock acceleration event on 8 October 2013. The PSD data described here was used to illustrate how effective the shock was at rapidly accelerating electrons. The PSD data showed that across a wide range of μ values, electrons inside of L^*=4.2 were accelerated, whereas electrons outside were lost.

The final example of my PSD contributions that enabled other collaborative studies is the calculation of the Total Radiation Belt Content (TRBEC) [*Spence et al.*, 2013a; *Huang et al.*, 2016]. Previous estimates of this quantity by *Baker et al.* [2004]; *Selesnick and Kanekal* [2009] used flux measurements by SAMPEX and POLAR respectively. Therefore to try and improve on this measurement, PSD from the Van Allen Probes can be integrated across μ, K and L^* to get a single number, the total number of electrons. An overview of this

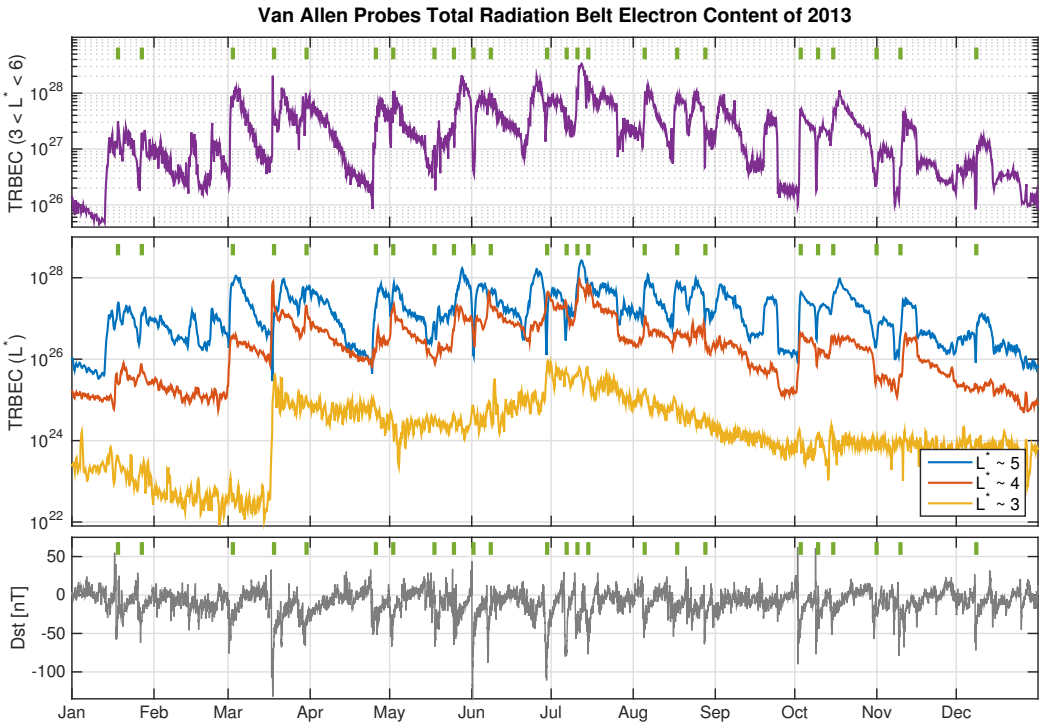

Figure 2-7: Figure from *Huang et al.* [2016] showing the Total Radiation Belt Content (TRBEC) for 2013. The top panel shows TRBEC for the entire outer radiation belt, with large (Dst <-50nT) storm marked with green dashes. The middle panel shows TRBEC over smaller L^* ranges. The bottom panel shows Dst.

quantity for 2013 is shown in Figure 2-7. While only a single quantity, ongoing work with TRBEC has shown it to be a great way to quantify losses and enhancements. In addition, the integration can be limited to particular ranges in either μ or L^*, allowing for studies of different particle populations such as the seed and core populations.

As described earlier, the PSD data product described in this chapter will be used in work presented in the subsequent chapters. The PSD data also played a critical role in the examples described above. While only described briefly here, these studies represent some of my important contributions outside of the work presented in the remainder of the thesis.

Chapter 3

Seed Population Case Study: 17 March 2013 Storm

3.1 Motivation

Up until recently, most radiation belt research has focused on the dynamics of the highly relativistic electrons that populate the outer belt. One possible source for these electrons, local acceleration, has been shown to be capable of quickly producing enhancements in relativistic electrons. *Reeves et al.* [2013] recently provided evidence of local acceleration of MeV electrons for an event on 8-9 October 2012 but that paper did not examine, in any detail, the relative effects of local acceleration and radial diffusion as a function of energy. This leaves open the question of the origin and evolution of the initial, lower-energy electrons (10s to 100s keV) that serve as a 'seed' population for the radiation belts. The instrumentation aboard the Van Allen Probes mission allows for the simultaneous observation of both the seed and core radiation belt populations to see how they behave and interact during acceleration events. This chapter examines phase space density data from one such event: the 17 March 2013 storm. The goal is to answer the focused question: *'Is it possible to directly observe and quantify the seed population's role in the acceleration of radiation belt electrons?'*

3.2 17 March 2013 Storm

A strong geomagnetic storm occurred on 17 March 2013. The relevant solar wind conditions for this event are shown in Figure 3-1. The event began with a strong interplanetary shock at 06:00 UT on 17 March [*Baker et al.*, 2014a], driving fast solar wind (>700 km/s) and elevated dynamic pressure (>10 nPa) (Figure 3-1d). This storm was one of the most geoeffective of the early Van Allen Probes mission, with Dst reaching -132 nT and Kp reaching 6+ (Figure 3-1f). The IMF Bz remained southward for the majority of the next 18 hours (Figure 3-1e), allowing for strong substorms, shown by the elevated AE index (Figure 3-1g). In particular, *Foster et al.* [2014] observed a large substorm at 20:17 UT.

The orbital positions for the Van Allen Probes spacecraft are shown in Figure 3-1a. The spacecraft were ideally suited to study the event, with their orbits straddling magnetic midnight. In addition, the spacecraft were closely spaced in their orbits, with RBSP-B leading RBSP-A by about 1 hour. The RBSP electron observations from two energy channels (211 keV and 1016 keV) are shown in Figures 3-1b-c. The observations show a strong loss of the relativistic electrons, likely due to the compression of the magnetopause, leading to magnetopause shadowing losses [*Baker et al.*, 2014a; *Hudson et al.*, 2015]. This loss was followed by a rapid enhancement of relativistic electrons deep within the outer radiation belt. This rapid enhancement, and the role the seed population plays in it will be the focus of the remainder of the chapter.

3.3 Phase Space Density Gradients

Figure 3.3 shows the MagEIS-B PSD for a range of μ values for a single inbound pass. The μ-dependent error estimates at 10 minute intervals are shown as error bars on each curve.

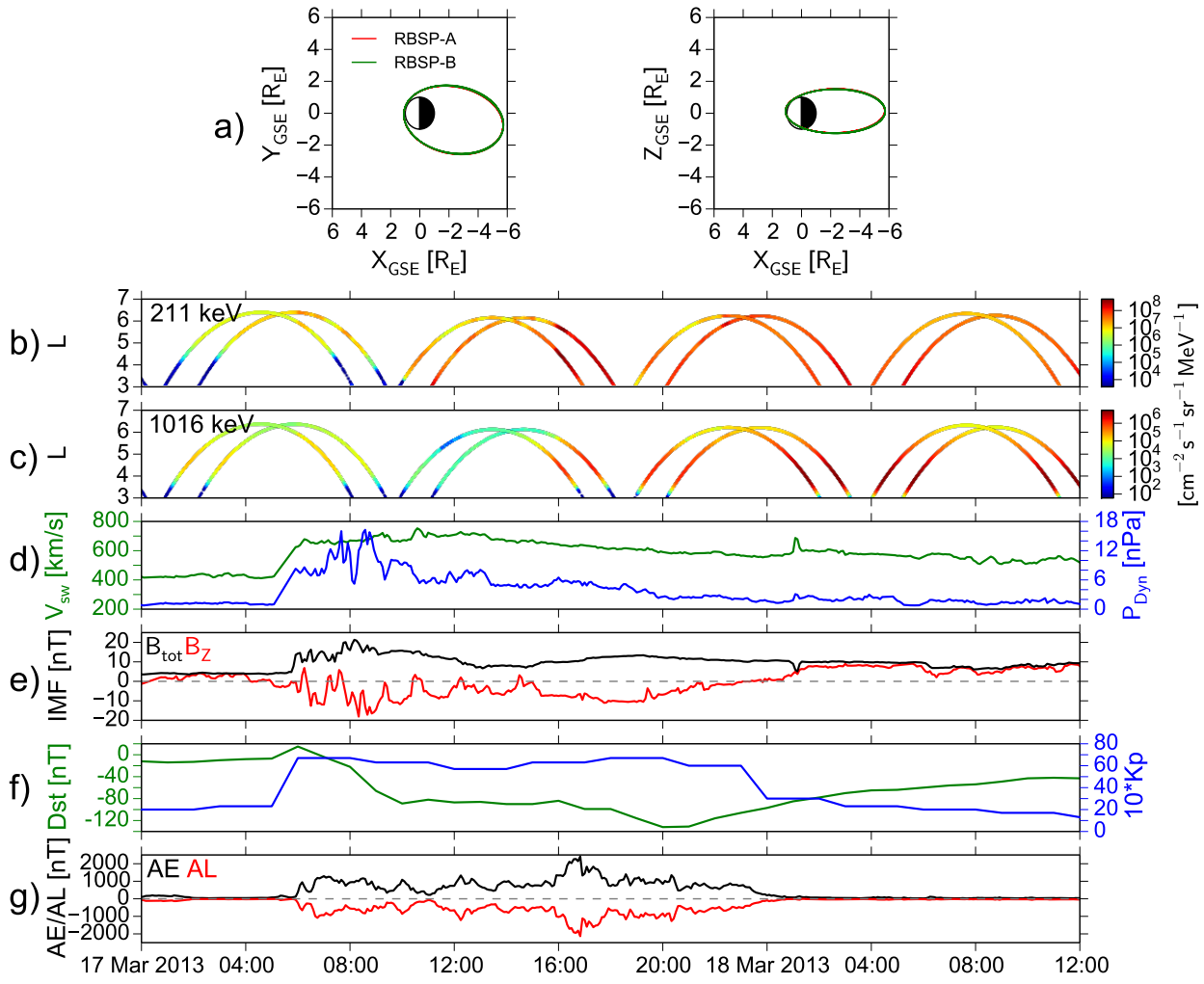

Figure 3-1: OMNI solar wind and RBSP electron fluxes from 17 March 2013 storm as follows: a) Orbital Positions, b) 211 keV electron omni-directional flux, c) 1016 keV electron onmi-directional flux d) Solar wind speed and dynamic pressure, e) IMF total B and B_Z , f) AE and AL indicies.

For this study we used phase space density matching on the period from March 19-21 to estimate the errors in PSD. For this period, conjunctions in L^* occurred close to apogee. We found that these errors were somewhat μ dependent, but were consistent with the REPT PSD errors found by *Morley et al.* [2013], with an average error factor of 1.3, and larger errors at the highest μ values. The pass shown in Figure 3.3 covered a period from 23:10 UT on March 17th to 3:02 UT on March 18th, placing it early in the recovery phase of the storm. Plotting this pass as a function of L^* allows us to quantify the PSD gradients throughout the entire outer radiation belt as a function of μ. We chose to look at the gradients during this pass to characterize the structure of the belt immediately after the acceleration event.

From Figure 3.3 it is clear that the PSD has a positive gradient in L^* for μ <200 MeV/G and flat or negative gradients for μ >200 MeV/G. This transition at 200 MeV/G is consistent with previous estimates by *Turner and Li* [2008], *Kim et al.* [2010], and *Turner et al.* [2012]. While this study does confirm previous results, these results also represent the first time these gradients have been quantified for a broad range of μ in the heart of the radiation belts during storm-time. Previous studies have been limited to measurements that were either beyond GEO, off-equatorial, or at higher μ. This μ dependence in the gradients persists through most of the recovery phase, until outward radial diffusion moves the PSD peaks beyond the Van Allen Probe apogee, resulting in positive gradients for all μ values. During quiet times the PSD peaks for relativistic electrons are typically at or beyond the Van Allen Probe apogee [*Turner et al.*, 2012], which makes it difficult to locate the transition point between positive and negative gradients. However, these observations are not unique to this storm. Figure 3.3 shows that the same transition at ∼200 MeV/G is also seen during the recovery phase of the 8-9 October 2012 storm.

As discussed in *Green and Kivelson* [2004], PSD profiles tend to be peaked in their

source regions. Therefore, since the <200 MeV/G population has a positive PSD gradient, this suggests the source region is beyond the Van Allen Probe apogee and these particles likely come from the plasma sheet. Conversely, the PSD profile of larger μ particles is peaked within (and therefore has a source within) the radiation belt. As suggested by *Turner et al.* [2012], the transition of these gradients around 200 MeV/G is consistent with the theory of local acceleration by wave-particle interaction with chorus waves. The <200 MeV/G particles that originate in the plasma sheet can be locally accelerated by interactions with waves to produce the higher μ particles that have a source within the radiation belt. A value of μ = 200 MeV/G corresponds to an energy of 400 keV at L^* = 4. *Horne et al.* [2005] showed that this is a critical energy for acceleration by chorus waves, where energies below it are scattered into the loss cone faster than they are accelerated. This suggests that this μ<200 MeV/G population could be the 'seed' population for the relativistic electrons in the outer radiation belt.

3.4 Storm Evolution

Next, we explore the evolution of the PSD over the course of the 17/18 March storm. In Figure 3.4, we plot the PSD from each inbound and outbound pass for six values of μ between 03:05 UT on March 17th, just before the storm, and 5:10 UT on March 18th, during the recovery phase. This allows us to examine how the PSD profile evolves in time over the course of the storm. All the given times correspond to the L^*=4.2 crossing time and are marked and color coded on the Dst plot in Figure 3.4 for context. For this section we looked at a higher K value (0.11 $R_E G^{1/2}$) in order to have sufficient coverage in L^* for the whole time period. In addition to the PSD observations, the integrated lower band chorus power

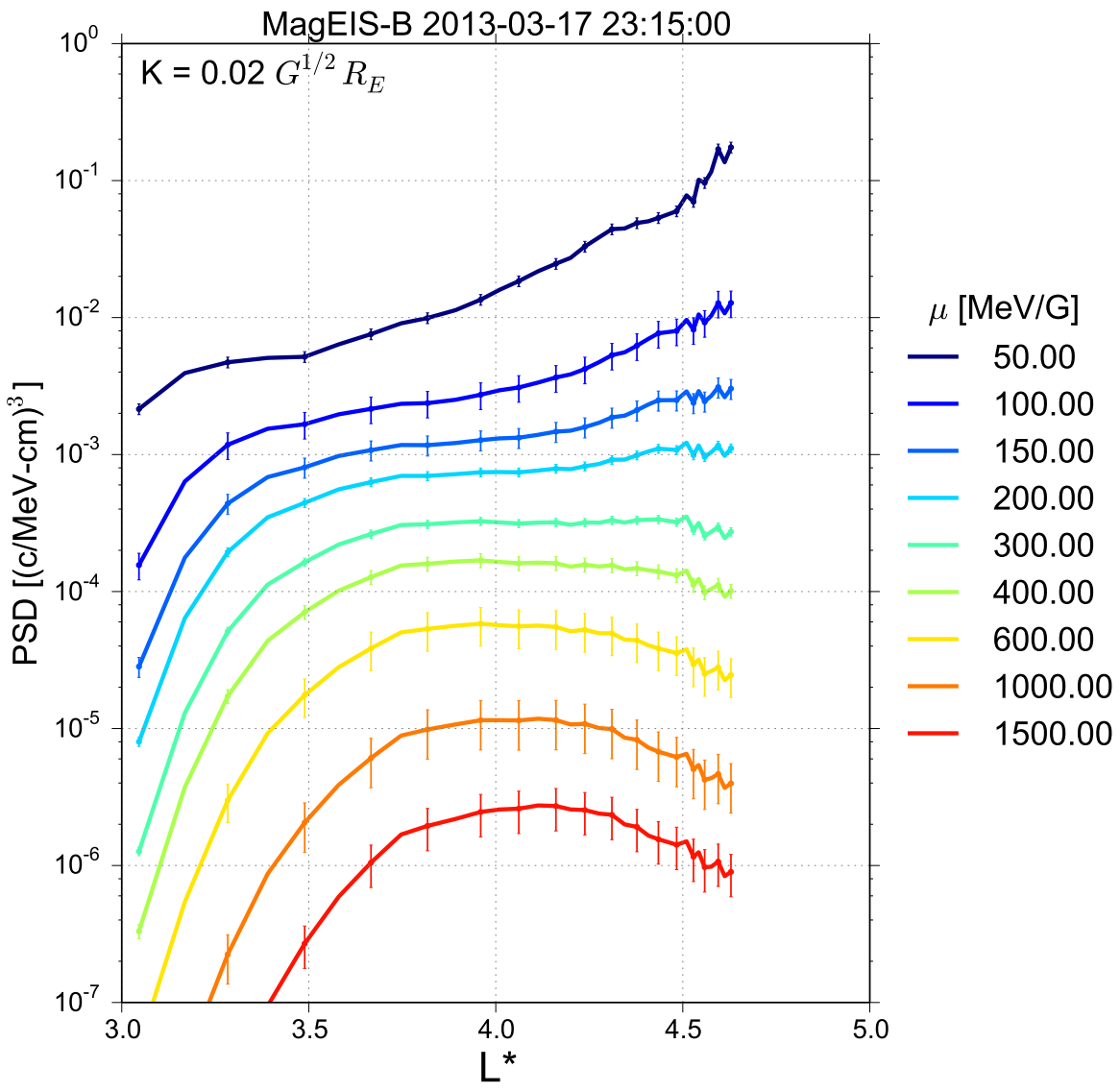

Figure 3-2: Radial PSD profiles from the 17 March 2013 Storm for various μ values during one inbound pass observed by MagEIS-B. Error bars are shown at 10 minute intervals.

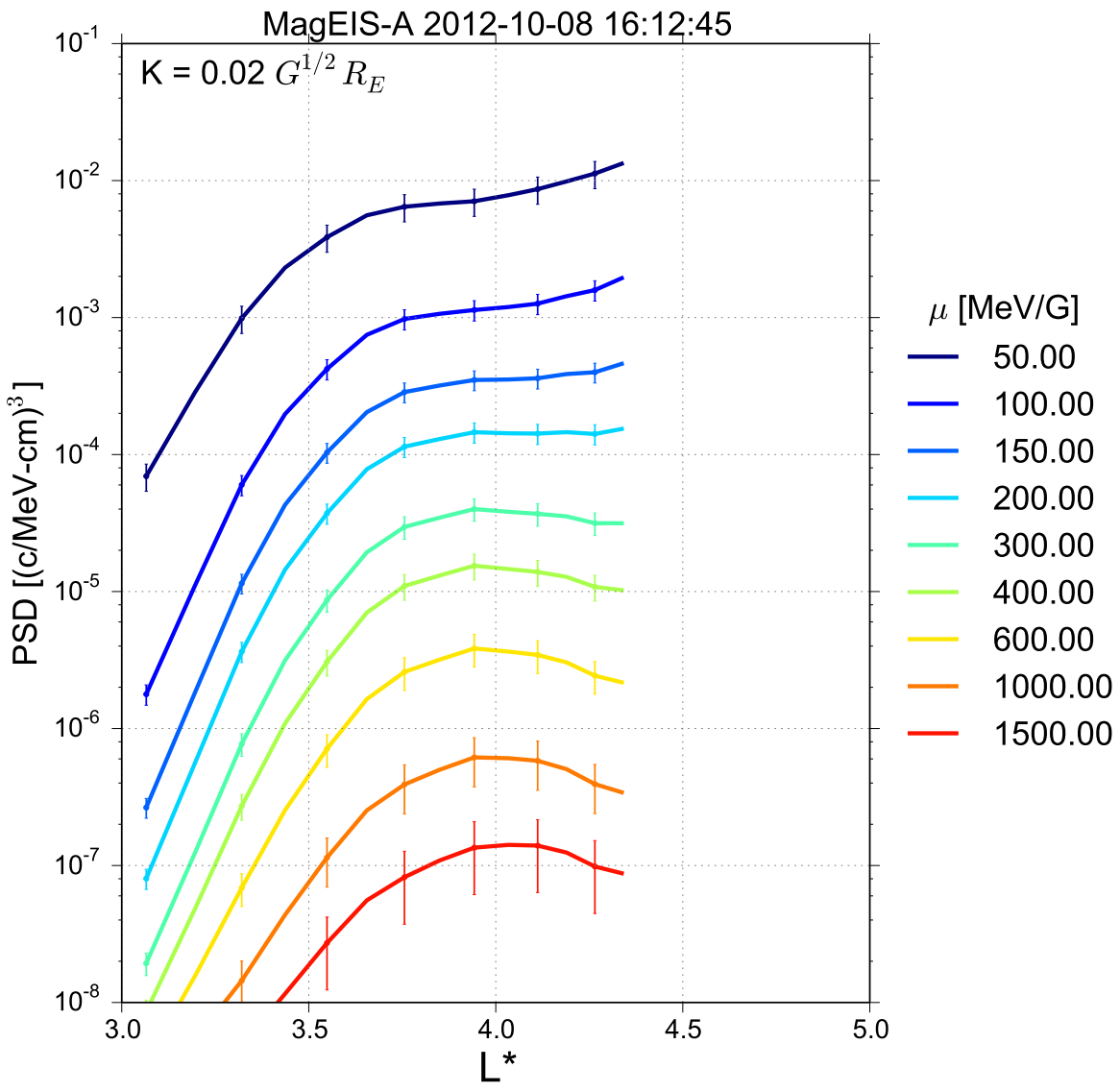

Figure 3-3: Radial PSD profiles from the 8-9 October 2012 storm for various μ values during one inbound pass observed by MagEIS-A. Error bars are shown at 10 minute intervals.

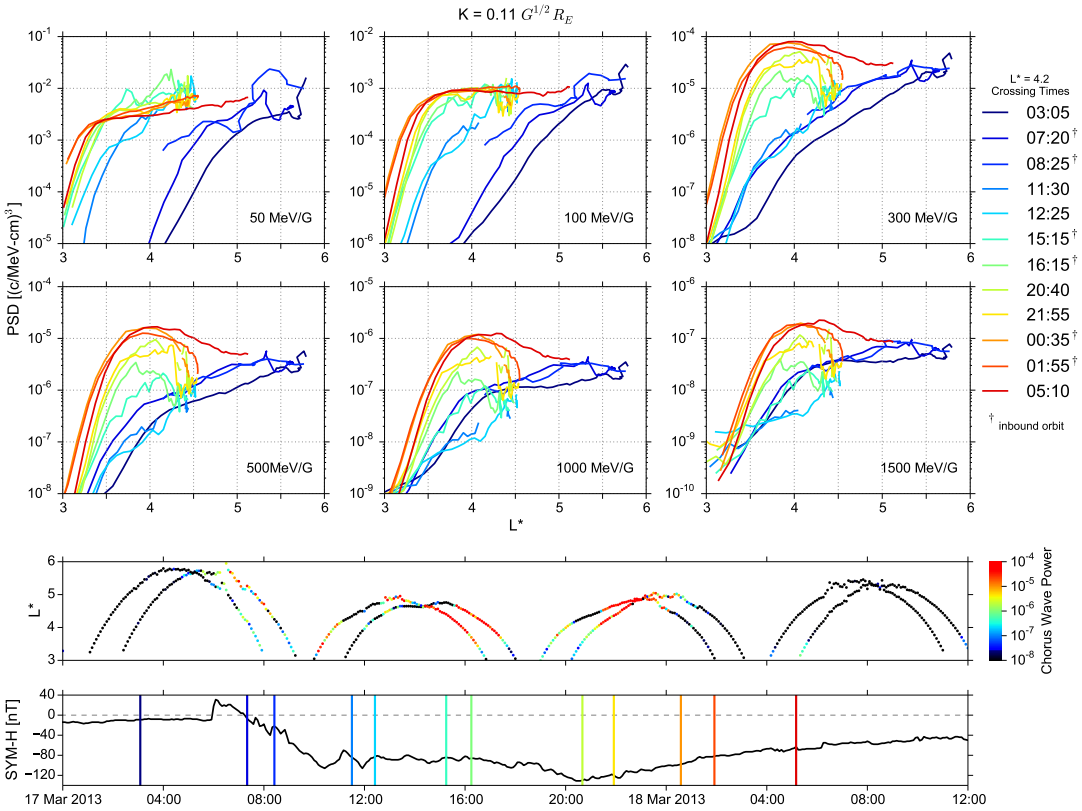

Figure 3-4: Phase Space Density evolution of the 17 March 2013 event. All times are the L^*=4.2 Crossing Times. Also shown are the SYM-H index and integrated lower band chorus wave power as measured by EMFISIS. The colored lines in the SYM-H plot correspond to each of the orbital passes shown in the PSD plots.

as measured by EMFISIS and the Dst index are shown in Figure 3.4.

It is clear that, over the course of the storm, the PSD evolves very differently for different μ values. For $\mu = 50$ MeV/G and $\mu = 100$ MeV/G, there is a large, sudden increase in PSD near the Van Allen Probes apogee, i.e. L^*>5.5 for the 3:05 UT orbit (outbound). This feature is likely associated with a substorm injection seen by GOES around this time (see Figure 3.4) and identified by the peak in AE at 8:00 UT. In the two subsequent inbound orbits, the peak emerges and grows inside $L^* = 5.5$ first for Probe A, the trailing spacecraft.

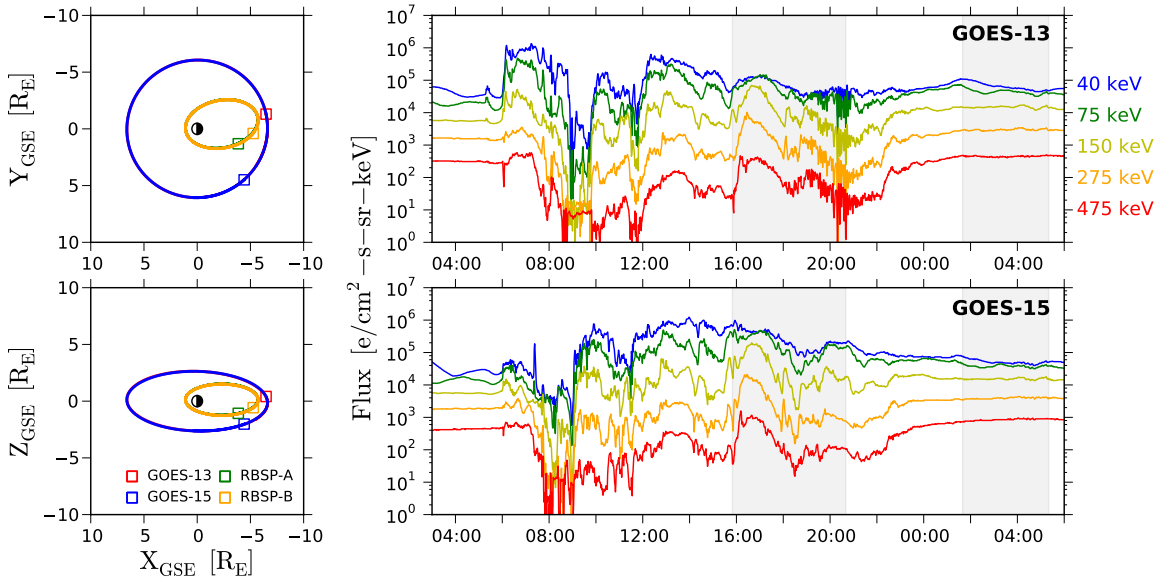

Figure 3-5: GOES-13 and GOES-15 observations from the 17 March 2013 event. The shaded regions are the times when the Van Allen Probes did not observe beyond L^* >4.4.

By the time the next two outbound passes come 3.5 hours later, the PSD has been enhanced at all L^*. For the μ=100 MeV/G population, this is followed by enhancement over a wide range of L^*, indicative of acceleration by radial diffusion. Later in the event, beginning at 15:00 UT, there is another enhancement seen at L^*<3.2 for μ = 50 MeV/G. This is associated with another substorm injection, coinciding with the peak in AE and observed by GOES around the same time (Figure 3.4). This reinforces the notion that injections of fresh lower energy electrons from the inner magnetotail are an important initial step that precedes local acceleration to higher energies.

The direct effects of the injections were not seen for μ>300 MeV/G. Instead there are clear PSD peaks that form at low L^* and then increase with time. During the 11:30/12:25 UT passes, the 50 MeV/G population has already been enhanced, and the 100 MeV/G begins to show signs of enhancement, and the >500 MeV/G population shows signs of a strong

loss process, which was related to a flux dropout during the main phase of this storm. On the following orbit 15:23/16:25 UT, the 100 MeV/G population continues to enhance, and 300-1000 MeV/G population begins to show peaks in PSD at low L^*. Finally, on 20:40/21:55 UT orbit, the 1500 MeV/G population begins to show a significant PSD peak. As shown in Figure 3.4, strong chorus wave activity was also observed during these orbits. Although not shown here, the REPT PSD at higher μ is qualitatively similar to the PSD at μ=1500 MeV/G.

As shown in *Green and Kivelson* [2004] and *Reeves et al.* [2013], an increasing phase space density peak may be an indication of local acceleration. Another possibility for the increasing PSD peaks is an on-off source at high L^*. However, for this storm such a source is unlikely. While the acceleration process is active, there were two periods when neither of the spacecraft were beyond the observed PSD peak (L^* >4.4). During the first, 15:53 - 20:41 UT, substorm injections were observed by GOES (Figure 3.4). However, for the second, 1:42 - 5:15 UT, there was no evidence of substorm injections in the GOES observations making an on-off source unlikely. Additionally, none of the injections seen earlier in the storm caused increases in the >300 MeV/G electrons. It is unlikely that this on-off source for >300 MeV/G electrons would only operate during the time periods when one of the spacecraft was not in a position to observe it.

Another possibility is that errors in the PSD calculation could account for some of the increases. Details on how errors in the global magnetic field models can lead to errors in PSD are discussed in Chapter 2. It is unlikely that these errors can account for the nearly two orders of magnitude increase in PSD seen over the course of the storm. While it is not possible to completely eliminate these other possibilities, local acceleration is the most likely explanation for the growing PSD peaks observed during this storm.

This set of observations shows clear evidence of a sequence of acceleration occurring sequentially with the injection of a lower-energy seed population from the plasma sheet radially inward. That process accelerates electrons up to a few hundred keV in the heart of the radiation belts [*Baker et al.*, 1998; *Baker and Kanekal*, 2008]. The higher energy electrons later show increasing PSD peaks, showing evidence of local acceleration. These peaks occur at the same time that chorus waves were observed by EMFISIS. This suggests that acceleration via wave-particle interactions with whistler-mode chorus is the most likely candidate for the observed acceleration. Modeling of the storm by *Li et al.* [2014] has also confirmed this conclusion. These two different acceleration processes for the populations below and above $\mu \sim 200$ MeV/G are clearly shown in Figure 3.4 and are consistent with a <200 MeV/G seed population preceding subsequent local acceleration to enhance the relativistic populations within the heart of the outer belt.

This timing of this acceleration process is shown more clearly in Figure 3.4, which shows the ratio of PSD to the pre-storm level (3:05 UT orbit) at $L^* = 4$. This figure clearly shows that at L^*=4, the initial acceleration of the seed electrons is followed by a strong loss of the >500 MeV/G population. This is then followed by acceleration at all values. The acceleration process for the relativistic electrons does not seem to begin until this seed population is in place at low L^* values. After the seed population is in place, the acceleration up to multi-MeV occurs over a period of less than 12 hours. More specific timescales for this acceleration process are difficult to determine without greater time resolution. However, the orbital configuration and instrumentation from the Van Allen Probes for this event allowed the observation of this progression from seed electrons up to multi-MeV energies with high precision and with excellent and unprecedented resolution and specification of the adiabatic coordinates.

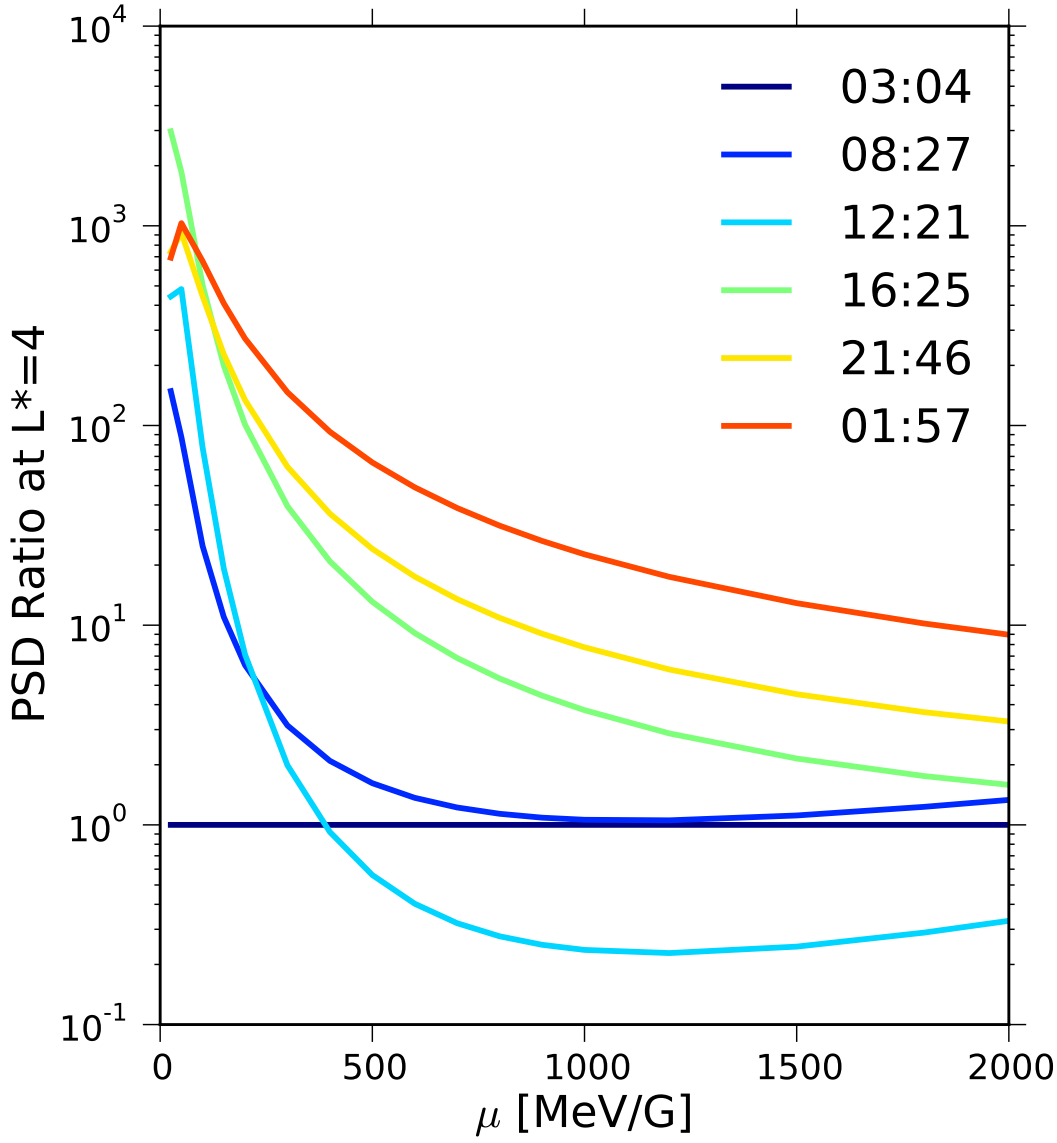

Figure 3-6: The ratio of the PSD at L^*=4 to the pre-storm level observed during the 3:05 UT orbit. For simplicity only the PSD from MagEIS-A is shown here. The colors of the curves correspond to those in Figure 3.4.

3.5 Conclusions

The goal of the chapter was to observe and to quantify the seed populations' role in the acceleration process. To address this goal, we presented electron PSD distributions from MagEIS over a broad range of μ values for the 17 March 2013 electron acceleration event. We have quantified the μ dependence of PSD gradients inside GEO for the first time, confirming the results of previous studies, with $\mu <$ 200 MeV/G showing positive gradients and $\mu >$ 200 MeV/G showing peaks in the heart of the radiation belts and flat or negative gradients at higher L^*.

We combine these observations with results showing local acceleration in the heart of the radiation belts [e.g. *Reeves et al.*, 2013]. Taking advantage of the comprehensive measurements available from the Van Allen Probes we can now connect the two steps of the acceleration process with a single, unified, set of observations. Our results demonstrate that the acceleration process for this storm begins with multiple injections of the seed population from the plasma sheet between 08:00 UT - 15:00 UT on 17 March 2013. This is followed by the local acceleration of the μ=300-1000 MeV/G population beginning around 16:00 UT. This ultimately leads to local acceleration up to multi-MeV energies by 21:00 UT.

Additionally, for this event, strong chorus wave activity was observed while the peaks in phase space density were developing. This provides strong evidence that wave-particle interactions with chorus waves is responsible for driving the acceleration process. In this scenario, the seed population plays a critical role of interacting with the waves and accelerating up to the highly relativistic energies for which the radiation belts are known.

Chapter 4

Statistical Properties of the Radiation Belt Seed Population

4.1 Introduction

In the previous chapter, we examined the role of the seed population during a single event, the 17 March 2013 storm. In this chapter, we extend the analysis to a wider time period: the first 26 months of the Van Allen Probes mission. In particular, we will examine the correlation between the core and seed populations for each enhancement event during this period. This builds on the work of *Li et al.* [2005] and *Turner and Li* [2008], who analyzed fluxes at geosynchronous orbit over a five-year time period. They found that when a time-lag was applied, the seed electron population fluxes were well correlated with the >1 MeV electron fluxes. However, since these observations were at geosynchronous orbit, they were not able to see the acceleration process itself, as it was happening in the heart of the radiation belt. In this chapter, we examine both the seed and core populations inside of the radiation belt over a long time period to see exactly for the first time how these two populations interact to produce radiation belt acceleration. In particular, we look to answer the focus

question: *'What correlations and causal relationships are there between enhancements in the seed population and enhancements in the core population?'*

4.2 Data

The dual Van Allen Probes spacecraft were launched on August 30, 2012 with a comprehensive suite of instruments to study the fields, waves and particles within the Earths radiation belts [*Mauk et al.*, 2014]. For this study we used data from the Relativistic Electron Proton Telescope (REPT) [*Baker et al.*, 2014b], which measures high energy (∼1-20 MeV) electrons, and the Magnetic Electron-Ion Spectrometer (MagEIS) [*Blake et al.*, 2014] which measures low and medium energy (∼20-4000 keV) energetic electrons. Both of these instruments are part of the Energetic Particle, Composition, and Thermal (ECT) plasma instrument suite [*Spence et al.*, 2013b]. These particle measurements, together with the magnetic field measurements from the Electric and Magnetic Field Instrument Suite and Integrated Science (EMFISIS) [*Kletzing et al.*, 2013] were used to calculate phase space density (PSD) for the Van Allen Probes mission from launch through the end of 2014.

To calculate the PSD, we follow the method laid out in Chapter 2. Pitch angle-resolved fluxes from MagEIS and REPT along with the magnetic field data from EMFISIS were used to calculate PSD as a function of the three adiabatic invariants μ, K and L^*. *Tsyganenko and Sitnov* [2005] was used as the global magnetic field model for these calculations. Using the phase space density at fixed 2nd and 3rd invariants, we focused on how phase space density evolved as a function of 1st invariant μ. In particular we investigated three distinct electron populations at different values. These populations are the seed population; which we define to be $\mu \approx 150$ MeV/G (∼200 keV at L^*=5); the core population ($\mu \approx 1000$

MeV/G; 1 MeV); and the ultra-relativistic population ($\mu \approx 4000$ MeV/G; 2.5 MeV).

Our goal of this study was to use these data-sets to investigate two questions: 1) What correlations exist between these populations and what are the relevant acceleration timescales? and 2) What conditions in the seed population lead to enhancements in the core and ultra-relativistic populations?

4.3 Correlations and Timing

To investigate their correlations, we examine the phase space density of the seed, core and ultra-relativistic populations for a period of 26 months between October 2012 and December 2014. These observations are shown in Figure 1. For this time period, we restrict our attention to those particles that are mirroring relatively close to the magnetic equator(K=0.11 $\mathrm{R_E G^{1/2}}$) and well into the outer radiation belt ($L^* = 5$). Figure 4-1 illustrates that each of these populations behave very differently and have different characteristic timescales. The seed population varies rapidly, with sharp increases on the timescale of hours. The core population varies less dynamically and follows a pattern of rapid increases followed by slow decay. The ultra-relativistic population follows a similar pattern to the core population, possessing even less dynamism. Despite these differences, there are many events, such as the 8-9 October 2012 event and the 17 March 2013 event, which elicit a coordinated response in all three of the populations, demonstrating that these populations are sometimes strongly correlated.

To understand these connections, we next quantify the properties of such events. Since the seed population is believed to play a key role in the acceleration process, we focused on enhancement events in the core ($\mu = 1000$ MeV/G) electrons. Similar to *Reeves et al.* [2003],

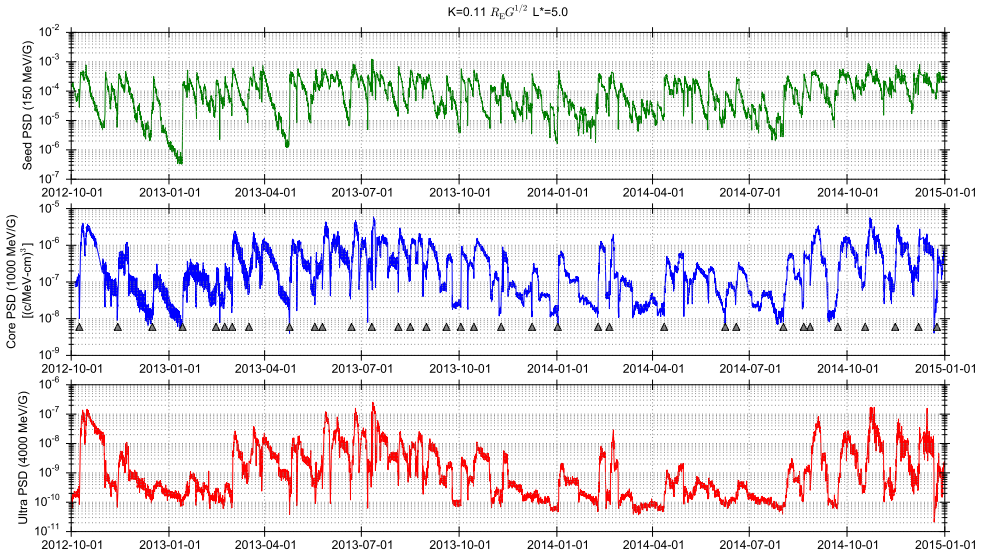

Figure 4-1: Overview of the phase space density for 3 different μ values: Seed (150 MeV/G), Core (1000 MeV/G) and Ultra-relativistic (4000 MeV/G) for a period from October 2012 through December 2014. All the data are for K=0.11 $R_E G^{1/2}$ and $L^* = 5$. The gray triangles in the core panel denote core enhancement events.

we require enhancement events to meet the following criteria:

1. The core population must increase by at least a factor of 2

2. The enhancement must be isolated, with no other events within ±48 hours

3. There must be no data gaps of more than 10 hours during the event

Implementing these criteria with second invariant K=0.11 $R_E G^{1/2}$ and $L^* = 5$ gave 34 enhancement events over the 26-month period. These K and L^* values were chosen since they represent the smallest K value continuously observed by the Van Allen Probes, and the typical L^* where the peak fluxes are observed. Although we did not place a requirement on any geomagnetic indices, the events represent an equal mixture of non-storm and storm-times, with 17 of the 34 events having a minimum Dst $\geq$ -40nT. In addition, all 34 of the

events are associated with an elevated Auroral Electrojet (AE) index. Table 4.1 shows a summary of these events, and they are marked with gray triangles in Figure 4-1.

Our first goal is to investigate the correlation between the different electron populations. Following *Li et al.* [2005] and *Turner and Li* [2008], we implement the technique of cross correlation analysis. For a number of μ value steps between 200 and 3000 MeV/G, we calculate the linear correlation coefficient between that population and the 150 MeV/G seed population. We then apply a series of time-lags between -2 and -48 hours to the seed population and repeat the calculation of the correlation coefficient. For each μ value, we record the time-lag that gave the maximum correlation coefficient. The time-lags as a function of μ for three L^* values are shown in the Panel A of Figure 4-2. Panel B shows the correlation coefficient as a function of μ for $L^* = 5$ with and without the time-lag applied. Panels C and D show the same calculation using only data for the 5 days leading up to the maximum core phase space density for each event. Data for L^*=5.5 is not shown for the active times, as the L^* of Van Allen Probes apogee is often less than 5.5 for periods of strong geomagnetic activity. The shaded regions in panels A and C represent the range of time-lags at L^*=5 where the correlation coefficient was within 1% of the maximum value. For the purposes of this study, we only consider the correlation to be significant if R $\geq$ 0.7. The lines in panels A and C are dashed when the maximum correlation coefficient goes below this threshold.

As shown in Figure 4-2, the core population has its maximum correlation at 10-25 hours with a correlation coefficient between 0.7 and 0.8. These results are consistent between $L^* = 4.5$ and $L^* = 5.5$, with marginally highest correlations at L^*=5. The value of the coefficient is similar for the active times, but the maximum correlation time-lag is much shorter, with a maximum between 0-13 hours. These results agree with the findings of

Date	L^*_{en}	Max/Min PSD	Post/Pre PSD	Clear PSD Peaks?	Min Dst [nT]
2012-10-08	4.2	472.1	232	Yes	-105
2012-11-13	4.5	92	19.3	Yes	-108
2012-12-17	Apogee	25.5	12.9	No	-27
2013-01-13	Apogee	34.4	24.5	No	-30
2013-02-14	Apogee	11.3	6.2	No	-36
2013-02-22	Apogee	41.6	8.6	No	-32
2013-03-01	5.0	166.4	21.9	No	-55
2013-03-17	4.2	148.2	22.8	Yes	-132
2013-04-24	5.0	343.4	36.2	No	-50
2013-05-18	4.5	75.2	9.1	Yes	-57
2013-05-25	4.5	17.1	16.7	No	-50
2013-06-21	5.0	114.2	13.4	No	-21
2013-07-10	4.7	13.6	20.8	No	-45
2013-08-04	4.7	200.5	9.4	No	-44
2013-08-16	Apogee	15.1	3.9	No	-35
2013-08-31	Apogee	38.9	5.5	No	-37
2013-09-19	Apogee	11.2	7.9	No	-19
2013-10-02	5.0	49.4	37	No	-60
2013-10-14	Apogee	12.1	4.9	No	-43
2013-11-09	4.6	61.5	17.2	Yes	-81
2013-12-08	Apogee	28.8	5.7	No	-66
2014-01-01	Apogee	111.6	36.8	No	-40
2014-02-08	Apogee	116.9	72.5	No	-30
2014-02-19	Apogee	78.8	36.7	No	-116
2014-04-12	Apogee	44	26.5	No	-81
2014-06-08	Apogee	8.7	3.0	No	-38
2014-06-18	Apogee	14.5	5.0	No	-33
2014-08-02	Apogee	15.1	10.4	No	-18
2014-08-21	5.25	38	6.7	No	-32
2014-08-27	4.5	153.9	14.1	Yes	-80
2014-09-22	Apogee	99.9	44.9	No	-22
2014-10-17	5.0	29.8	24.5	No	-21
2014-11-15	Apogee	139.9	42.8	No	-50
2014-12-07	4.8	68.9	16.7	No	-24
2014-12-24	4.7	46.2	5.1	No	-38

Table 4.1: Properties of the core enhancement events used in this study. Columns describe the date of the enhancement, the L^* where the maximum enhancement is seen, the ratio of the maximum to minimum PSD, the ratio of average post-event PSD to pre-event PSD, whether the event had clear observations of PSD peaks, and the minimum Dst for the event.

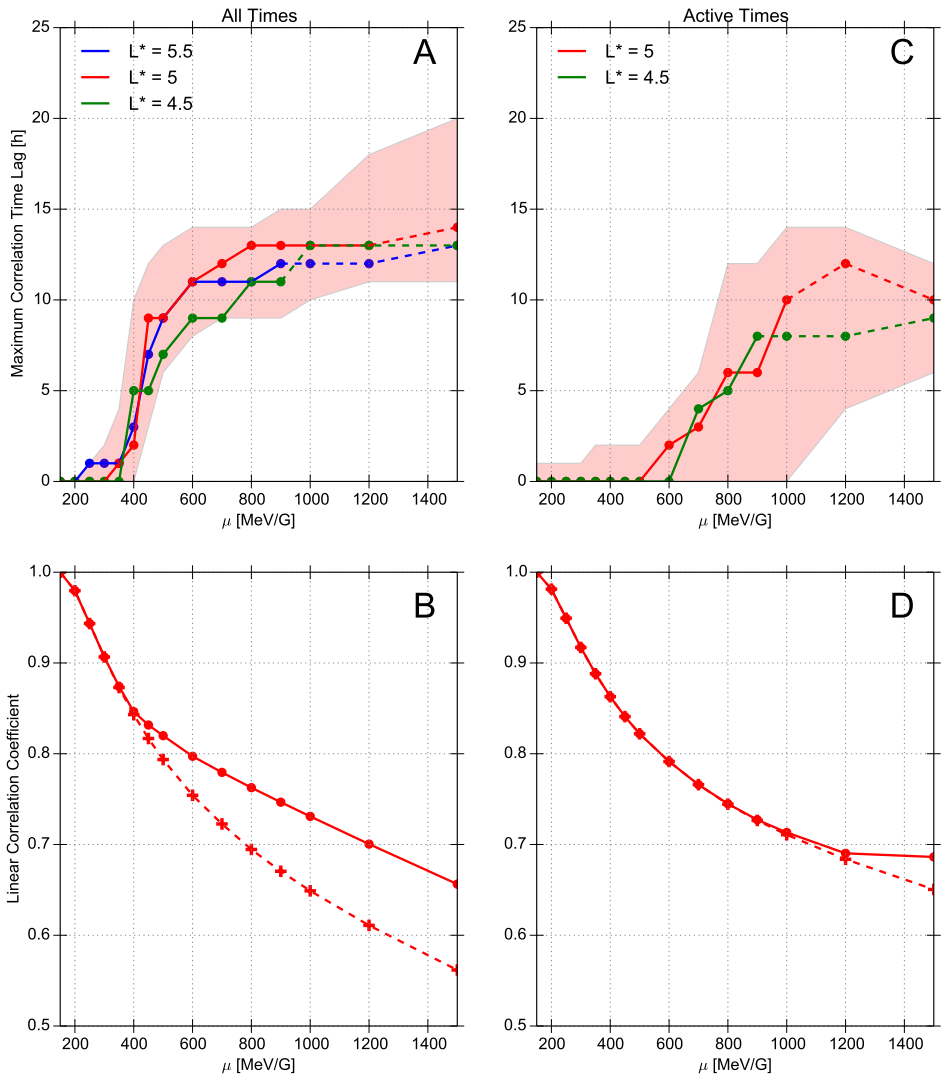

Figure 4-2: Results of the cross correlation analysis. Panels A and B show results with all available data, panels C and D only includes results from times within 3 days of a core enhancement event. Panels A and C show the time-lag that gives the maximum correlation coefficient with respect to the μ=100 MeV/G population as function of μ for 3 different L^* values. Panels B and D show the correlation coefficient at L^*=5 as a function of μ with no time-lag (dashed line) and the time-lag applied (solid line).

Turner and Li [2008], who performed a similar study using fluxes at geostationary orbit. For similar energies, *Turner and Li* [2008] found a similar correlation coefficient (0.8) and a slightly larger time-lag (between -17 and -34 hours).

As shown in panels A and C, this correlation is only significant up to ≈800-1000 MeV/G. This indicates that while the seed population is well correlated with the core population it is not directly connected to the ultra relativistic population. However, when performing a similar analysis with respect to the 1000 MeV/G core population, we find that the core and ultra-relativistic populations were very well correlated, with R >0.8 up to 5000 MeV/G. These results are consistent with the stepwise acceleration processes described in *Boyd et al.* [2014], where the seed population is accelerated up to 1 MeV and then subsequent acceleration brings that population up to multi-MeV energies.

The correlation coefficients shown in Figure 4-2 give the average timing for all of the events, but the timing for individual events can vary greatly. Figure 4-3 shows the distribution of time-lags for each of the enhancement events that meet the criteria described above for $\mu = 1000$ MeV/G and $\mu = 4000$ MeV/G. For the core population, in the majority of the events the maximum seed population PSD occurs 10-20 hours before the core, but there are several events with much shorter timescales (<10 hours). Similarly, for the ultra-relativistic population, the maximum seed population occurs 15-25 hours earlier, but several of the events have much shorter or longer timescales. As shown in both panels, for all of the events, the seed population enhancement preceded the enhancement at higher energies.

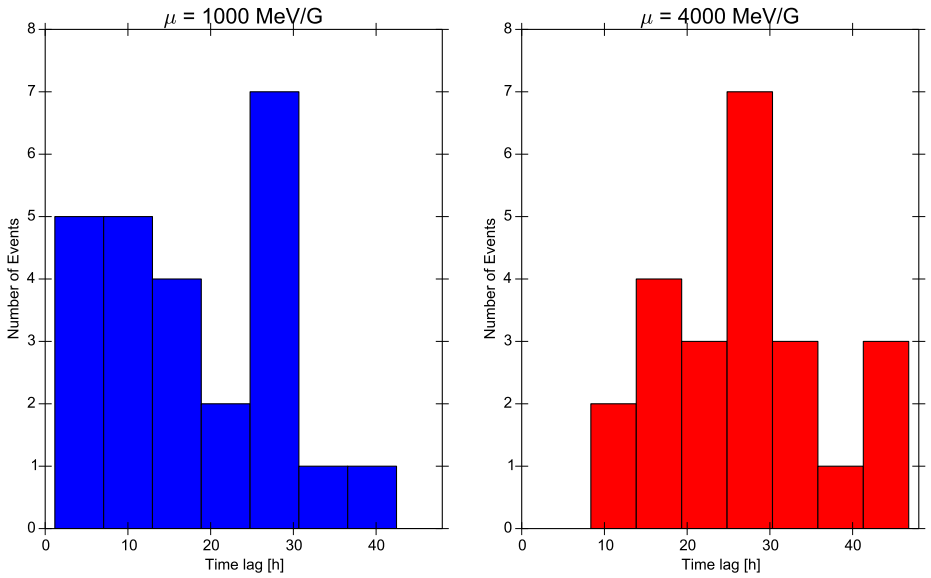

Figure 4-3: Distribution of time-lags for all core enhancement events relative to the μ=150 MeV/G seed population. Left panel shows μ = 1000 MeV/G, right panel shows μ = 4000 MeV/G.

4.4 Superposed Epoch Analysis

Our next focus is to investigate the seed population conditions that lead to radiation belt acceleration. Therefore, we needed to know what the seed population conditions were for each of the core enhancement events. We use superposed epoch analysis to investigate this. For each event, we use the L^* where the largest enhancement was observed. As shown in Table 4.1, for more than half (18) of the events, this was at or near the Van Allen Probes apogee (L^*>5.25), but several of the events featured enhancements inside of L^* = 5. In addition, 7 of the events showed clear evidence of PSD peaks at low L^*. The t=0 epoch time was defined to be at the maximum core population PSD for each event.

The results of this analysis are shown in Figure 4-4. The three panels show the ultra-relativistic, core and seed population PSDs respectively. In all panels, the median (thick line) and the upper and lower quartiles are shown. The sequence of the acceleration process

is shown clearly in Figure 4-4, with the seed population reaching its maximum first (t=-0.8), followed by the core population (t=0), and ultimately the ultrarelativistic population (t=0.3).

The initial conditions for all three of the populations vary by about an order of magnitude. The final values for the core and ultra-relativistic populations vary by roughly the same amount. However, this is not the case for the seed population. All of the events end up with nearly the same number of seed electrons (to within a factor of 5). This is despite the fact that the initial conditions of the seed population varies by several orders of magnitude. Given that all of these events showed an enhancement in the core population, it is possible that this represents the minimum, or threshold value for the seed population. This value at 1×10^{-4} $(\frac{c}{cm \cdot MeV})^3$ is labeled in Figure 4-4.

4.5 Seed Population Threshold

The seed population threshold can also be investigated by looking at all seed population enhancements, rather than just those that are associated with increases in the core population. For each of the seed population enhancements, we compare the maximum PSD value with the fractional change in the core population PSD in the following 48 hours. This comparison at L^*=4.5 and L^*=5, is shown in Figure 4-5. In both panels, the shaded region indicates where the maximum PSD is above the threshold from Figure 4-4. For all values of the maximum seed PSD, there were many events that did not lead to core enhancements, so it is immediately clear that larger seed population values do not necessarily lead to enhancements in the core population. However, all of the events that did lead to core enhancements (shown by the red markers) have maximum seed populations near or above 1×10^{-4} $(\frac{c}{cm \cdot MeV})^3$.

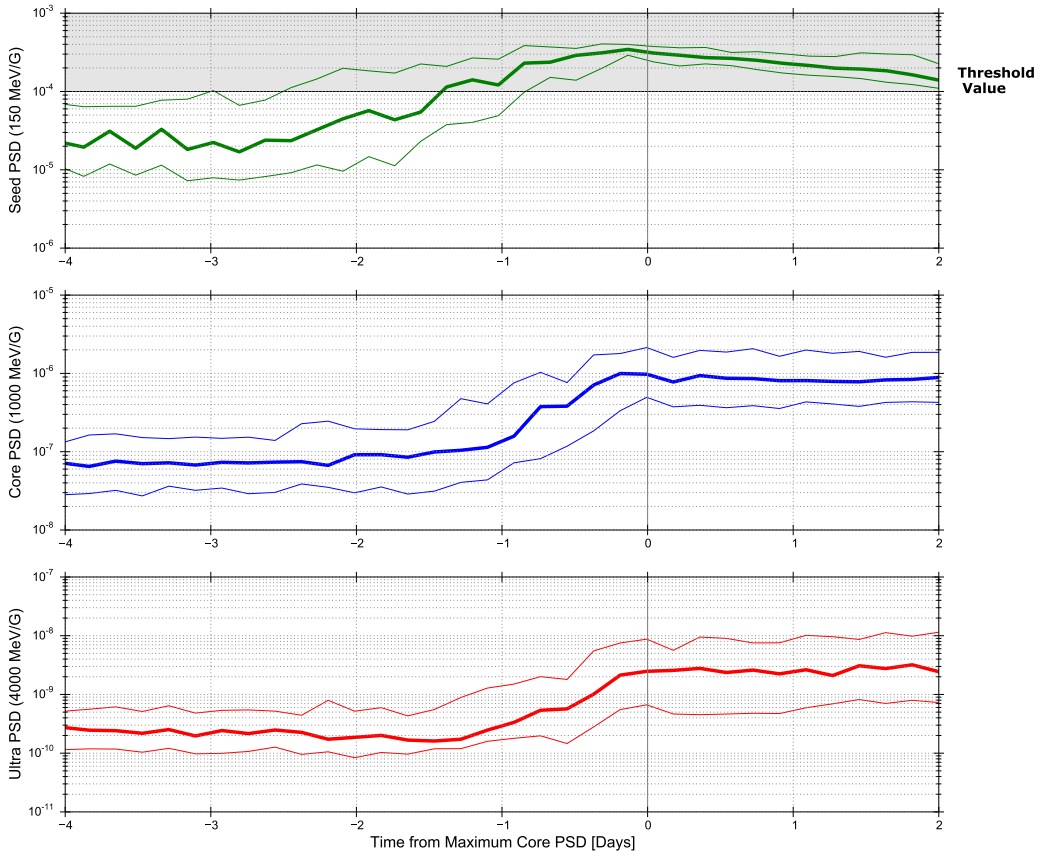

Figure 4-4: Superposed epoch analysis for all core enhancement events. Top panel shows the seed population (μ = 100 MeV/G), the middle panel shows the core population (μ = 1000 MeV/G) and the bottom panel shows the ultrarelativistic population(μ = 4000 MeV/G). In each panel, the thick line is the median, and the thinner lines the upper and lower quartiles. T=0 epoch time was taken to be the maximum core PSD for each event. Data for each event is taken at the L^* where the largest core enhancement was observed. The apparent threshold value and/or saturation limit at 1×10^{-4} $(\frac{c}{cm \cdot MeV})^3$ is marked on the seed population plot.

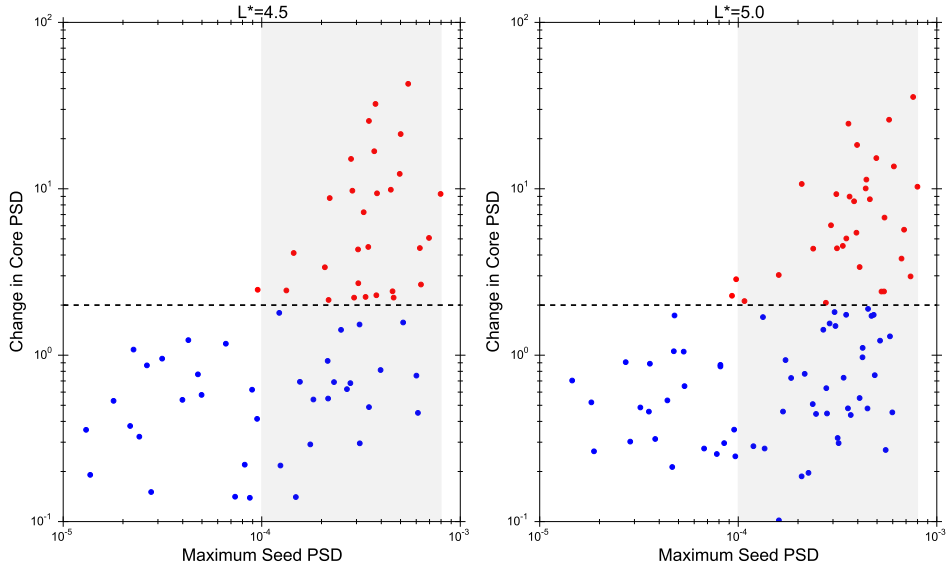

Figure 4-5: Comparison of the maximum seed PSD value and the fractional change in the core PSD for the 48 hours following each seed population enhancement. Left panel shows data from L^*=4.5, right panel shows L^*=5. The horizontal dashed line marks where the core population increased by a factor of 2. Points above this value are shaded red. The shaded region shows where the maximum seed population PSD is above the threshold value and/or saturation limit of 1×10^{-4} $(\frac{c}{cm \cdot MeV})^3$

This provides further evidence that this value represents a necessary threshold for the seed population in order to produce a core population enhancement.

As noted earlier, the superposed epoch shown in Figure 4-4 was done at the L^* where the acceleration was taking place. It is plausible that the seed population plays a role in controlling the location of the acceleration for each event. To investigate this, for each event, we compare the minimum L^* where the seed population was above the threshold value to the minimum L^* (to within $\pm$ 0.25) where the core population increased by at least a factor of 2.

The relationship between the minimum L^* at which the core acceleration takes place and minimum L^* penetration of the seed population is shown in Figure 4-6. These values are very well correlated, with a linear correlation coefficient of 0.84. In addition, for nearly all

L^*	Fraction of Time above Threshold	Total Events	Enhancement Events (%)	Acceleration, no Enhancement (%)	No Acceleration (%)
4	0.075	25	14 (56 %)	2 (8 %)	9 (36 %)
4.5	0.301	52	31 (59 %)	14 (26 %)	7 (13.5 %)
5	0.532	55	33 (60 %)	9 (16 %)	13 (24 %)
5.5	0.707	62	35 (56 %)	10 (16 %)	17 (27 %)

Table 4.2: Statistics for the fraction of time seed population is above threshold.

of the events, to within $L^* \pm 0.25$, the enhanced seed population penetrates further inward than where the acceleration is observed. This suggests that the seed population forms an inner boundary. Only outside of this boundary are there enough seed electrons to facilitate the acceleration process.

The majority of the time, when the seed population is above the threshold, there are enhancement events in the core population. Additionally, all of the core enhancement events seen in the 26-month interval are preceded by a seed population enhancement, indicating they are one key ingredient to core population enhancements. However, the seed population is only one part of the acceleration process. Without waves to accelerate the seed electrons, there would be no enhancements to the > 1 MeV populations. As noted in Table 4.2 at $L^* = 5.5$, the seed population is above the threshold value more than 70% of the time. Even with an elevated seed population, continued chorus wave activity driven by substorm activity is needed to drive MeV electron enhancements [*Meredith et al.*, 2001, 2002]. In addition, these acceleration processes take place at the same time as loss processes. As shown in Table 4.2, there are many instances when loss processes overwhelm any acceleration taking place, or there is no acceleration seen in the higher energy populations. All of these results point to the fact that the seed population is a critical piece in a very delicate acceleration process. While an enhanced seed population is necessary, alone it is not sufficient for radiation belt acceleration.

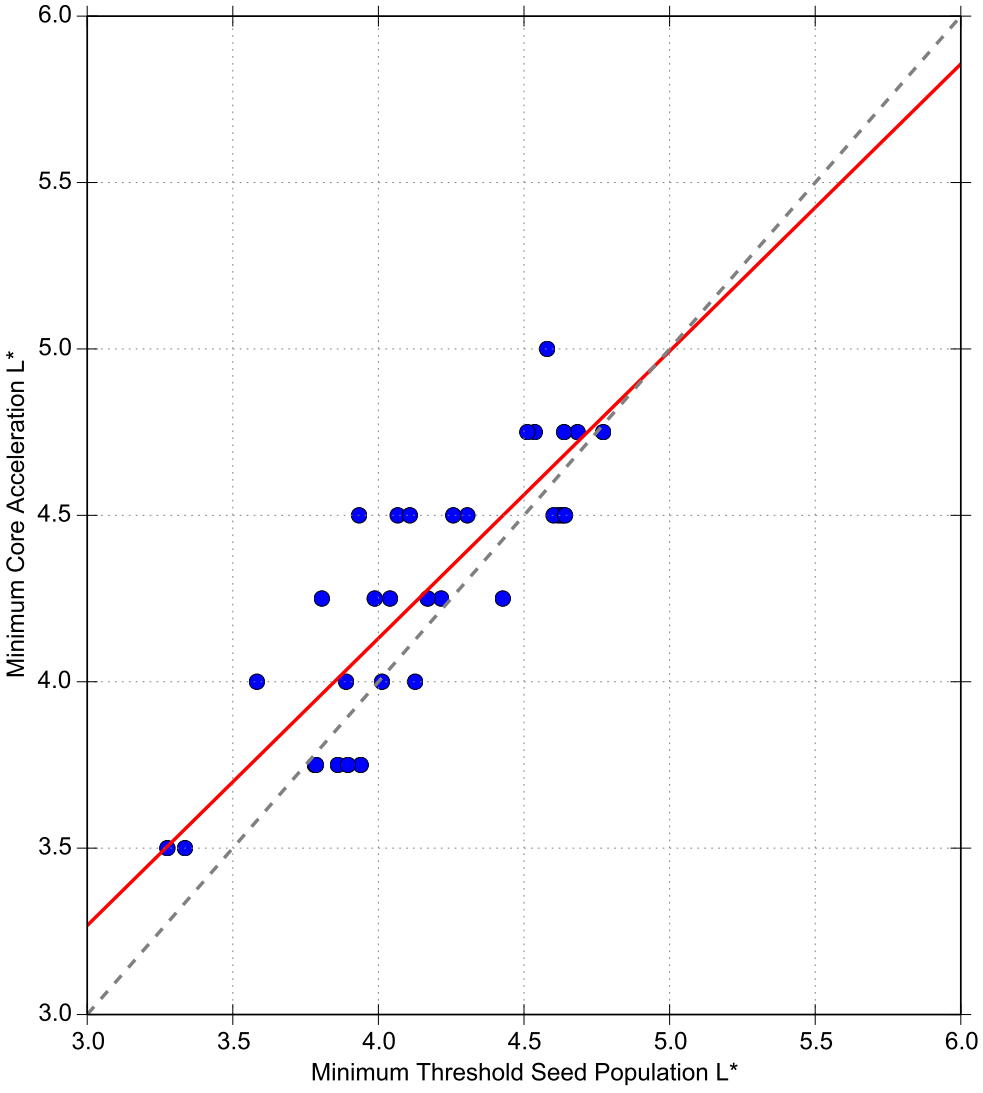

Figure 4-6: Relation between the minimum L^* where the seed population is above the threshold value and/or saturation limit of 1×10^{-4} $(\frac{c}{cm \cdot MeV})^3$ and the minimum L^* where the core population was enhanced by at least a factor of 2. The red line is the best-fit line with a linear correlation of 0.84.

4.6 Discussion

Beginning with the work of *Baker et al.* [1998], the seed population has been recognized as a key part of the acceleration process. While the seed population has been well studied for particular events, this paper represents the first substantial statistical studies of the seed population in the radiation belts and how these properties relate to the variability in the core population. The results presented here confirm the results of *Turner and Li* [2008], where the seed population enhancement precedes the core population by 20-25 hours. However, we offer a substantial improvement on previous results by looking at phase space density at fixed invariants in the heart of the radiation belts.

As noted in *Turner and Li* [2008] and *Li et al.* [2005], in addition to local acceleration, radial transport processes can also explain the time-lags seen between the 100s keV and MeV electrons. This is due to the fact that lower energy electrons move inward faster, so they are observed earlier. While it would be difficult, if not impossible, to completely separate the radial transport and local acceleration effects for each event, we note that, on average, we observe smaller time-lags than the studies at geosynchronous orbit. If radial transport were the dominant mechanism for most of these events, we would expect to see larger time-lags, as the particles take longer to drift into lower L-shells. Therefore, while radial transport is undoubtedly responsible for some of the results in this study, local acceleration likely plays an important role in most of the events, particularly those at lower L^*.

The work presented here makes it clear that the seed population plays a critical role in controlling both where and when core population enhancements will take place. All of the core enhancement events seen in this 26-month period were associated with seed population enhancements up to a particular level. This level likely represents a threshold value that

the seed population must reach in order for the acceleration process to take hold. It is possible that this threshold represents a saturation point for these electrons in the inner magnetosphere. As shown in Figure 4-6, acceleration can only begin when a given L^* is filled or saturated with seed electrons. It is probable that this saturation point is associated with the Kennel-Petschek limit. As described in *Kennel and Petschek* [1966], the fluxes of electrons of this energy range are subject to an upper limit imposed by pitch angle scattering via wave particle interactions. For average strength magnetic field, at L^*=5, μ=150 MeV/G corresponds to ∼230 keV. Therefore, from Equation 2.2, a PSD value of 1×10^{-4} $(\frac{c}{cm \cdot MeV})^3$ will correspond to a flux of $9.56 \times 10^3 \frac{\#}{s \cdot sr \cdot cm^2 \cdot keV}$. From the values provided by *Schulz and Davidson* [1988], the Kennel-Petschek differential limiting flux of at this energy at L-value would be $\sim$ $5.09 \times 10^4 \frac{\#}{s \cdot sr \cdot cm^2 \cdot keV}$. We have shown that observations of these events are consistent with local acceleration by these same waves. Therefore, since these waves would be active during these periods, it is not surprising that this threshold is comparable with the Kennel-Petschek limit, and the seed population must be close to this saturation limit in order to produce an enhancement of MeV electrons.

However, as mentioned here, the seed population is only one part of the acceleration process. Future studies will also involve incorporating the source population and chorus and ULF wave activity to investigate the other ingredients required for the acceleration process. In addition, further investigation into the relationship between the seed population and geomagnetic indices such as AE could yield useful results that could be useful for models and for the use of the seed population as a predictor of core population enhancements.

4.7 Conclusions

The goal of this chapter was to understand the statistical relationship between the radiation belt seed, core and ultrelativistic populations. To investigate this we used phase space density observations for the first 26 months of the Van Allen Probes mission taken at fixed second and third invariant. We have three main conclusions:

1. The seed population (150 MeV/G) is strongly correlated with the core population (1000 MeV/G), but is not directly connected to the ultra-relativistic population (4000 MeV/G).

2. The strongest correlation between the seed and core populations is at a 10-15 hour time-lag. This time-lag is smaller (0-13 hours) during enhancement events.

3. The seed population is subject to a threshold value or saturation limit that is a necessary condition for the enhancement of MeV electrons.

All of these conclusions are consistent with a step-wise acceleration picture where a 10s-100s keV seed population is accelerated up to $\sim$1 MeV and then is subsequently accelerated up to multi-MeV energies. While this picture has been previously shown for individual events (as shown in Chapter 3), this study shows that the seed population plays an important role in governing radiation belt dynamics.

Chapter 5

Investigating the Source and Seed Populations

5.1 Introduction

The previous two chapters focused on the role of the seed population in the enhancement of MeV electrons. However, as demonstrated in the previous chapter, the seed population is only one part of the acceleration process. In particular, the 10s-100s keV seed population needs to interact with the waves in order to be accelerated up to MeV energies, and these waves are in turn generated by the few-10s keV source population. A schematic diagram of these populations, along with role that VLF chorus waves play in transferring energy from the seed to the higher energy populations is shown in Figure 5-1.

For many events, such as the 17 March 2013 event presented in Chapter 3, all of these elements work together to rapidly produce MeV electrons. However, this is not always the case. *Jaynes et al.* [2015] looked at a period in September 2014 where one or more of these pieces were missing and the acceleration process broke down. Although the solar wind had favorably high velocity during the period of 14-19 September 2015, the IMF B_Z remained northward for a long period over that interval. Despite elevated levels of seed electrons, there

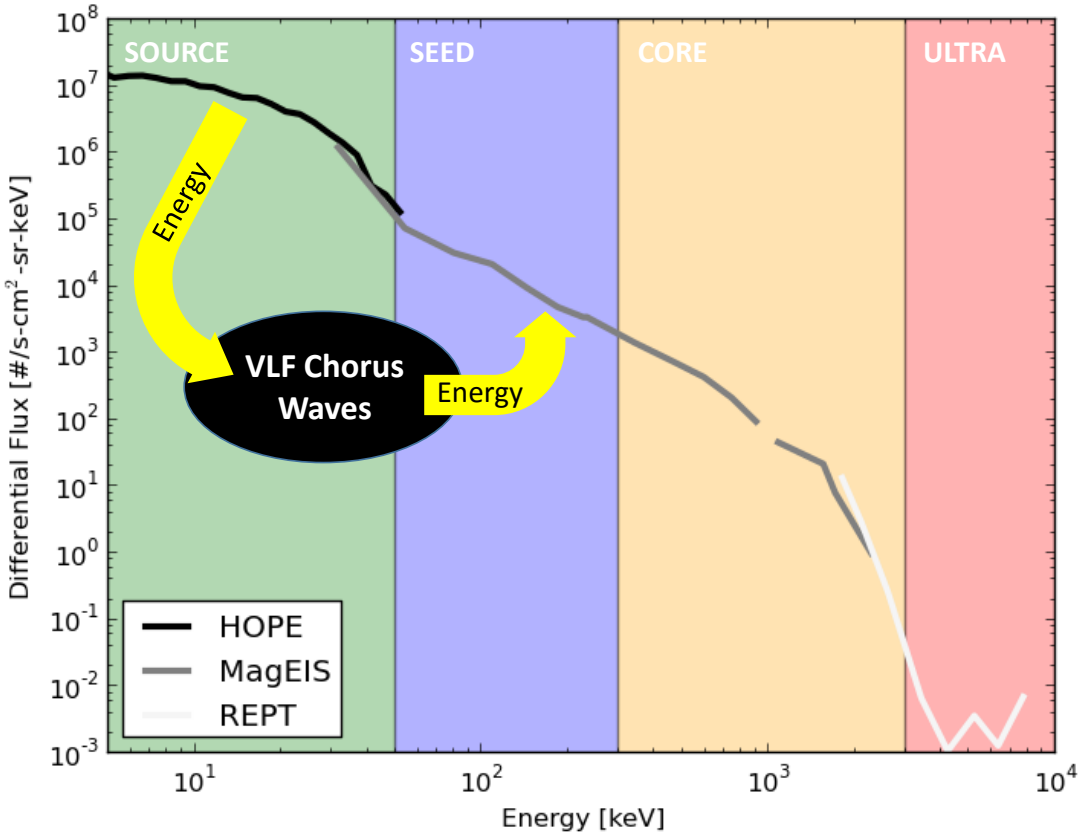

Figure 5-1: Diagram showing the different particle populations (source, seed, core) and the role that VLF chorus waves play to transfer energy between the populations.

was little/no injections of source electrons, leading to weak wave activity and no enhancement in the higher energy electrons. This event offered a clear example that when a piece of the acceleration process is missing, the process breaks down and does not lead to relativistic electron enhancements.

In this chapter, we build on the work of *Jaynes et al.* [2015] and look at several events with varying levels for the source and seed populations. Exploring these populations in conjunction with observations of the higher energy core population will give a more complete picture of the entire acceleration process and what role these low energy populations play in it. In particular, we aim to finish addressing the focus question: *'How do differing inputs of source and seed electrons lead to acceleration (or lack thereof) in the radiation belts?'*

5.2 October 2014 Case Study

The first time period we will we examine is 14-25 October 2014. The period, which culminated in a relativistic electron enhancement, was relatively quiet with Dst >-40 nT for the entire interval. During this time the Van Allen Probes apogee was in the post-midnight sector. The observations of the source and seed electrons from MagEIS are shown in Figure 5-2. It should be noted that for the source population we are examining particle fluxes rather than phase space density. This is due to the fact that at source population energies (few-10s keV), electric fields become increasingly important in determining the particles' motion. Therefore, the value of third invariant L^*, which is based on the global magnetic field, no longer accurately describes the position of these particles. While the first and second invariants are likely still valid, much of the advantage of using PSD in adiabatic coordinates is lost and it becomes more convenient and accurate to instead look at particle fluxes to explore

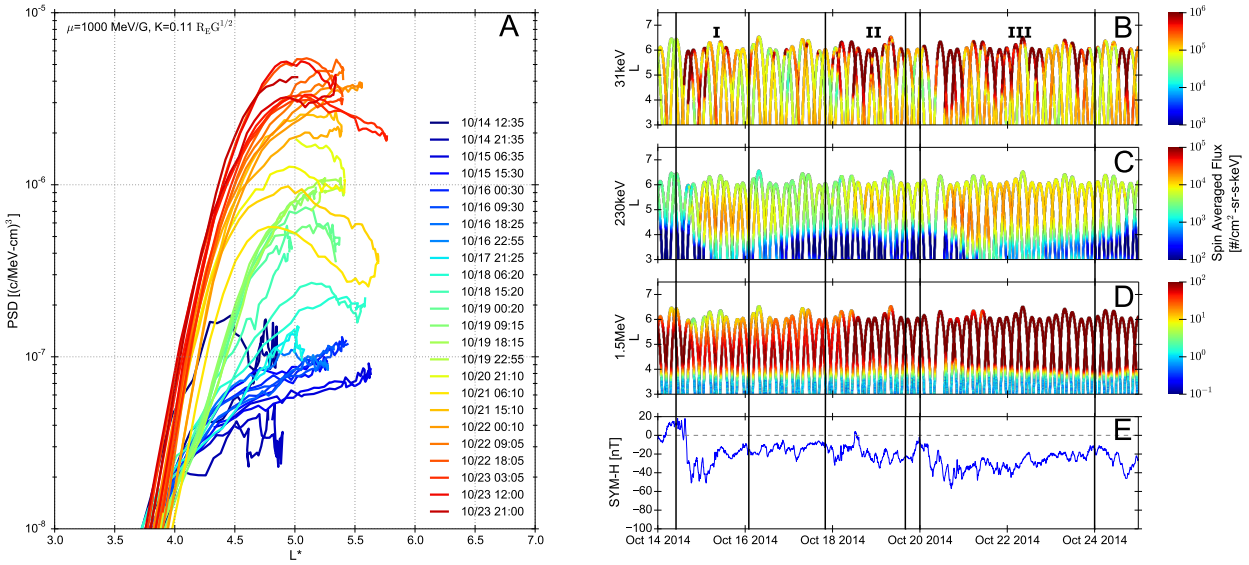

Figure 5-2: Overview of the 14-25 October 2014 period. A) μ = 1000 MeV/G PSD observations for the entire interval, B-D) Spin averaged fluxes of the source (31 keV), seed (230 keV) and core (1.5 MeV) electrons respectively and E) SYM-H index. The periods marked I, II and III mark the three time periods of interest for this event.

the source population dynamics.

In order to analyze this event, we have divided it into three time periods denoted as I, II and III, on Figure 5-2. Each of these time periods has a different behavior of the source and seed populations leading to different outcomes for the core population. More specifically, The first time period (I) features a strong source and seed population at different times along with very little change at core population energies. The second time period features a strong source population and a moderate seed population along with a small increase in the core population. Finally, the third time period (III) featured strong core and seed populations, leading to a large enhancements of the core population. In addition to observations of the source and seed populations, we examined the changes in the relativistic population phase space density. In particular, we looked at the μ = 1000 MeV/G PSD observations, which are shown in Figure 5-2A. The PSD observations for each time period are shown in the colored traces and the traces from other times are shown in gray for context.

The final set of observations for this time period are the chorus wave measurements from EMFISIS. For each time period (I,II,III) the lower band chorus wave power was obtained by integrating between 0.1 and 0.5 f_{ce}. Since waves are a highly localized phenomena, waves may be active (and consequently affecting the particles) even if they are not locally observed by the spacecraft. However, local observations of the wave activity can offer the best available indication of whether these waves are active. Combining these wave observations with the core PSD measurements and the seed and source flux observations gives a picture of each part of the acceleration process. In the following sections, we examine each of the time periods (I,II,III) individually to determine how different levels of source and seed electrons lead to changes in the relativistic population.

5.2.1 Time Period I: No Acceleration

A summary of the first time period is shown in Figure 5-3. This time period begins with strong substorm activity, noted by the elevated AE index (Figure 5-3G) and the injection of source electrons beginning at 14:00 UT on 14 October (Figure 5-3B). These injections persist until 03:00 UT on 15 October when B_Z turns northward for an extended period. As shown in Figure 5-3E, these injections also generated strong chorus activity at L=5 around 18:00 UT on 14 October. However, as seen in Figure 5-3A, the was little to no change in the core PSD for this time period, indicating that there was no acceleration of the MeV electron population during this time. This is due to the fact that the seed population (Figure 5-3C) was missing during the early part of this period. The seed population only goes above the threshold value at 23:00UT on 14 October, after the strong chorus activity and near the end of the injections of source electrons. Even though this period saw injections of source electrons generating chorus, the seed population was not above the threshold while the waves

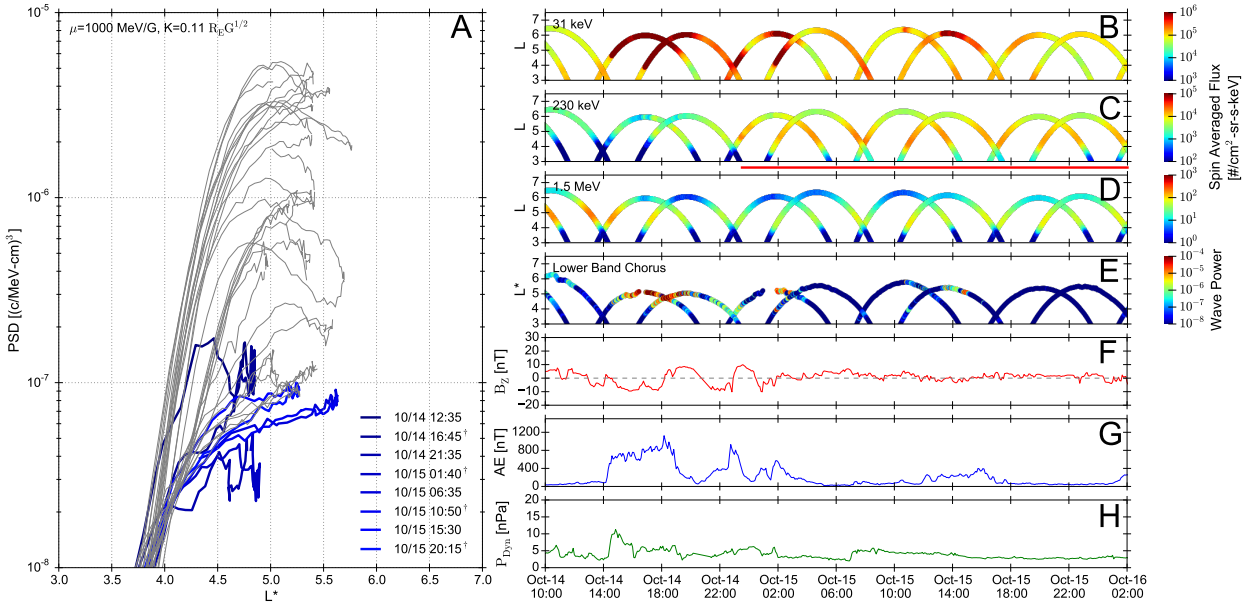

Figure 5-3: Overview of the time period I in the 14-25 October 2014 event. A) $\mu = 1000$ MeV/G PSD observations. B-D) Spin averaged fluxes of the source (31 keV), seed (230 keV) and core (1.5 MeV) electrons respectively. The red line under panel C denotes times when the seed population is above the threshold described in Chapter 4. E) Integrated lower band chorus power, F) IMF B_Z, G) AE index and H) Solar wind dynamic pressure.

were active. Therefore, there were not enough seed electrons to be accelerated by the waves, stopping the acceleration process before it could lead to MeV electron enhancements.

5.2.2 Time Period II: Small Acceleration

A summary of the second time period is shown in Figure 5-4. Similar to the previous period, the second time period begins with substorm activity and injections of the source electrons, beginning at 03:00 UT on 18 October and persisting for the next ~30 hours, until B_Z turns northward. As shown in Figure 5-4E, these injections were effective in generating lower band chorus activity throughout the entire time period. However, unlike the first time period, these waves overlap with an enhanced seed population, which goes above the threshold beginning at 17:00 UT on 18 October. With all the pieces in place, the acceleration process can be seen

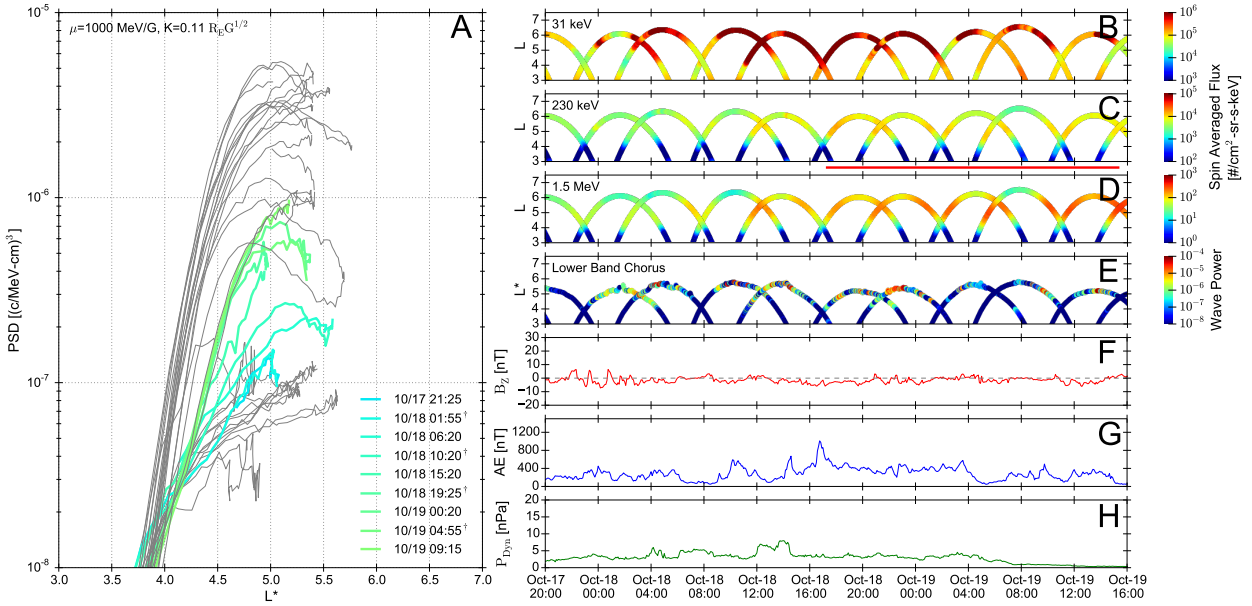

Figure 5-4: Overview of the time period II in the 14-25 October 2014 event. A) μ = 1000 MeV/G PSD observations. B-D) Spin averaged fluxes of the source (31 keV), seed (230 keV) and core (1.5 MeV) electrons respectively. The red line under panel C denotes times when the seed population is above the threshold described in Chapter 4. E) Integrated lower band chorus power, F) IMF B_Z, G) AE index and H) Solar wind dynamic pressure

to be working in core population PSDs, with peaks forming at L^*=5.2 and growing in time (Figure 5-4A). These PSD peaks only begin to form once the seed population is above the threshold value, even though there was chorus activity earlier in the time period. Overall the core PSD increases by a factor of ∼8 during this time period. This acceleration slows during the end of the period, coinciding with the end of the source electron injections.

5.2.3 Time Period III: Strong MeV Enhancements

A summary of the second time period is shown in Figure 5-5. The final time period begins with more than 48 hours of substorm activity and the injection of source electrons. Additionally, the strongest seed population levels seen in the entire event are observed during this time period, and the seed population above the threshold for nearly the entire period

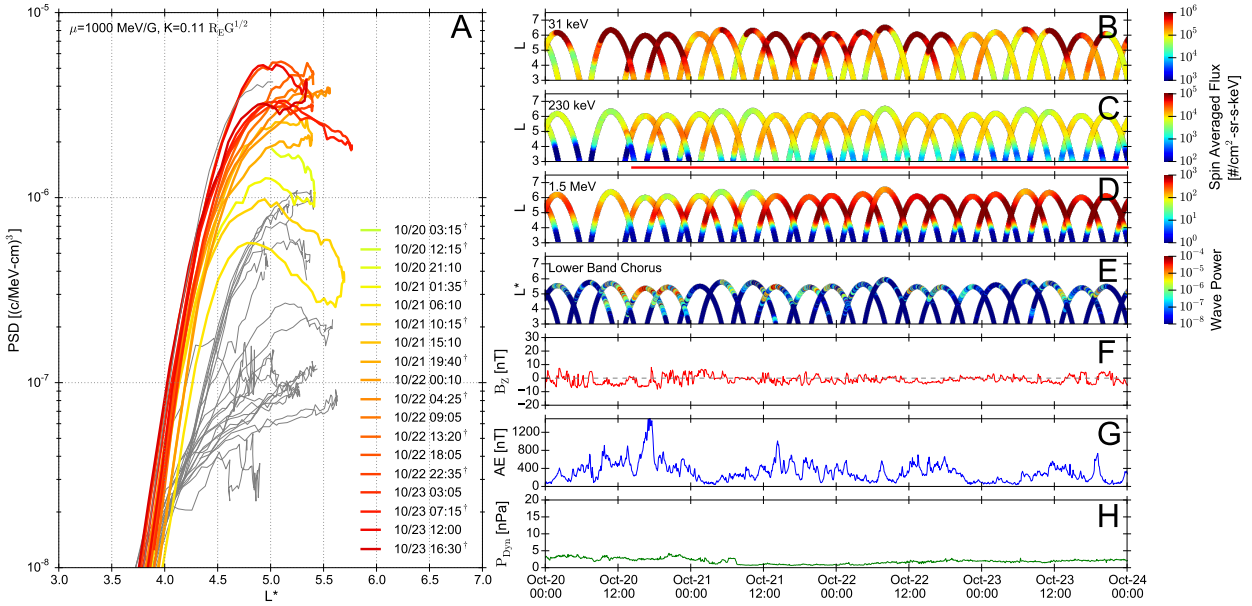

Figure 5-5: Overview of the time period III in the 14-25 October 2014 event. A) $\mu = 1000$ MeV/G PSD observations. B-D) Spin averaged fluxes of the source (31 keV), seed (230 keV) and core (1.5 MeV) electrons respectively. The red line under panel C denotes times when the seed population is above the threshold described in Chapter 4. E) Integrated lower band chorus power, F) IMF B_Z, G) AE index and H) Solar wind dynamic pressure

beginning at 13:00 UT on 20 October. As shown in Figure 5-5E, chorus activity is observed throughout the time period, especially early in the event, just after the enhancement of the seed population above the threshold value. This leads to large enhancements in the core population, evidenced by the growing peaks at L^*=4.9 shown in Figure 5-5A. During this time period, the core PSD increases by a factor of ∼12.

This event definitively shows that continued injections of source electrons, coinciding with an enhanced seed population above the threshold value is needed to produce an enhancement in the MeV electrons. If a piece of this process is missing, or as in time period I if the pieces do not come together at the same time, then the process breaks down and does not accelerate the seed population up to higher energies. The interrelated responses of the varied elements of the ensemble acceleration during this event (and others not shown here) are similar to that reported by *Jaynes et al.* [2015], demonstrating that this is a consistent and robust

feature of the dynamic system.

5.3 Acceleration Timescales

In the 15-25 October 2014 event described above, once all the pieces were in place, the acceleration process took place over the course of more than two days. This stands in sharp contrast with events with much faster timescales such as the 8-9 October 2012 storm [*Reeves et al.*, 2013] or the 17 March 2013 storm described in Chapter 3. In this section we compare two events that both produce strong enhancements to the MeV core population but at very different timescales. In particular we explore how the behavior of the source and seed population contributes to the different timescales.

The first event we explore occurred on 12 April 2014. This enhancement event was produced during a moderate storm, with minimum Dst = -81 nT. The Van Allen Probes apogee was located in the pre-noon sector during this event. The second event was a much larger storm (minimum Dst = -204 nT) on 22 June 2015. During this event, apogee was located in the dusk sector. Despite the large difference in Dst, both storms featured similar levels of enhancements to the 1 MeV core population. The μ=1000 MeV/G PSD traces for each of the events are shown in Figure 5-6. Both of the events feature growing PSD peaks, a clear indication that local acceleration was active. However, the timescales for the local acceleration is very different for each of the events. The 12 April 2014 event takes place over the course of more than 48 hours as evidenced by the steady rise in PSD between $4<L^*<5$ from ∼21:50 UT on 4/11 (medium blue curve) until ∼22:05UT on 4/13 (orange curve). This contrasts with the 22 June 2015 event which takes place in nearly half the time (∼30 hours) with the major enhancement starting at 22:40 UT on 6/22 (dark blue curve)

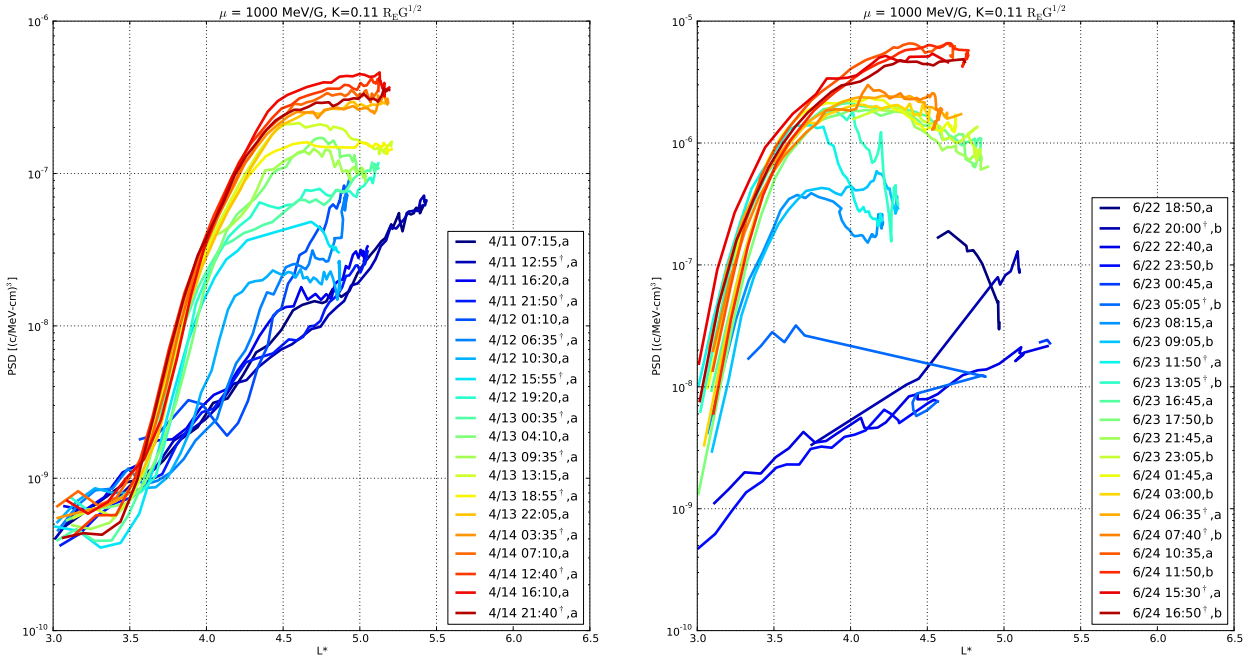

Figure 5-6: PSD profiles from the 12 April 2014 and 22 June 2015 events. Panel A shows RBSP-A observations from the April 2014 event and Panel B shows RBSP-A and B observations of the June 2015 event. Both panels show PSD with μ = 1000 MeV/G and K=0.11 $R_E G^{1/2}$.

between 3.5<L^*<5, with an initial abrupt increase of ∼6 hours lasting until ∼5:05UT on 6/23 (medium blue curve, followed by a slower increase lasting another 24 hours until ∼6:35UT on 6/24 (orange curve). Unlike the first event, the 22 June 2015 began with a strong loss of relativistic electrons, so with respect to the pre-storm levels at this energy, both storms featured a very similar increase of a factor of ∼15.

A side-by-side comparison of the source and seed electrons for these events is shown in Figure 5-7. The differences between the two events are immediately apparent. First, the flux of the seed population (second panels of Figure 5-7) during the 22 June 2015 is higher by more than an order of magnitude. Second, the source population (top panels of Figure 5-7) for the 22 June 2015 featured brief but intense substorm activity, including a large injection of source electrons into low L-shells. While intense, the injections in this storm lasted for

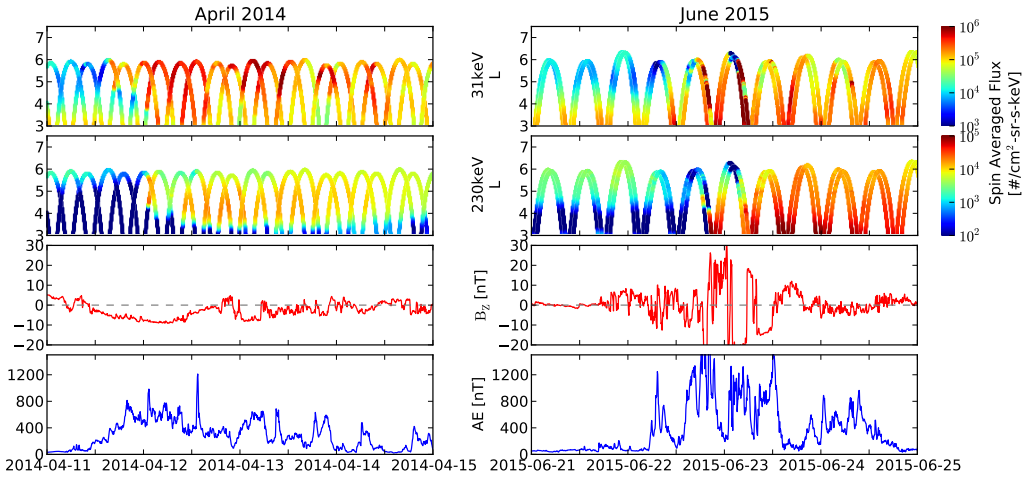

Figure 5-7: Comparison of the 12 April 2014 and 22 June 2015 events. The plots on the left side show observations of the 12 April 2014 event, and the right side plots show the 22 June 2015 events. For each event, the first two panels show spin averaged fluxes of the source population (31 keV) and the seed population (230 keV). The bottom two panels show IMF B_Z and the AE index.

less than 18 hours. The April 2014 event, on the other hand featured a long period ($\sim$48 hours) of nearly continuous small injections.

These observations suggest that there is a fundamental difference in the way that larger storms operate in comparison to smaller storms, even if the end result for the core radiation belt electrons appears to be the same. To test whether this pattern generally holds, we looked a subset of the enhancement events shown in Table 4.1. In order to reduce the ambiguity between radial diffusion and local acceleration events, only the events with enhancements inside of the Van Allen Probes apogee were chosen. To quantify how long we see injections of the seed population, we used AE >300 nT as a proxy for the strong substorm activity that drives these injections. The number of hours with AE >300 nT for these events is shown in Table 5.1.

With the exception of the 21 August 2013 event, these events all follow the same pattern where the largest events feature injections for shorter timeperiods than for smaller storms.

Date	Hours with AE >300 nT	Max AE [nT]
2012-10-08	21	1240
2013-11-13	19.5	400
2013-03-01	26.25	1350
2013-03-17	17.5	2430
2013-04-24	35.91	890
2013-05-18	34.25	1250
2013-06-21	40.58	950
2013-07-10	53.83	1130
2013-08-04	28.75	1120
2013-10-02	28.67	2070
2013-11-09	31.75	1040
2013-08-21	18.08	790
2014-08-27	43.08	1180
2014-10-17	32.33	580
2014-12-07	29.33	1408
2014-12-24	22.25	940

Table 5.1: Table showing the number of hours with AE above 300 nT for various events. Highlighted events are large storms (Minimum Dst <-100 nT).

While this is a small sample size, particularly for the larger storms, this suggests that there is a balance between the required level of seed and source populations. For the largest events, the acceleration process is more efficient, and highly enhanced seed populations can be accelerated faster and therefore do not require the waves and more indirectly the source population to be active for as long a time period to get MeV particle enhancements.

As shown for these events, and more generally by *Reeves et al.* [2003], a stronger storm in Dst does not guarantee a larger response of the radiation belts. In addition, storms that produce a similar overall effect on the radiation belts can have important difference in how the acceleration process plays out. Both the 22 June 2015 and the 12 April 2014 events produce similar enhancements in the MeV electron population, but the source and seed populations behave differently leading to very different acceleration timescales.

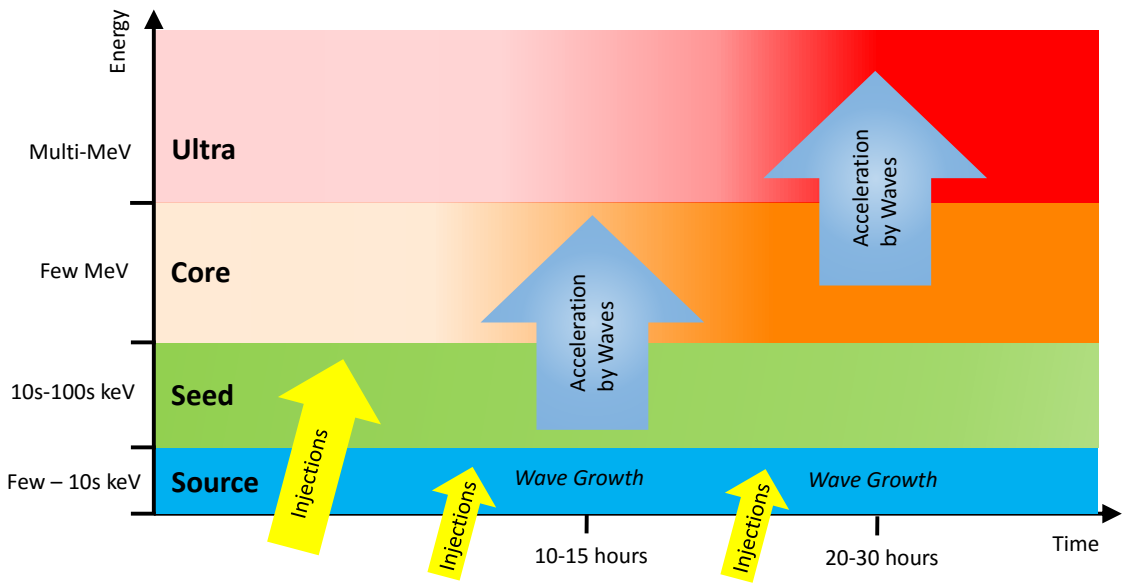

Figure 5-8: Diagram of the local acceleration process depicting the role of the source and seed populations.

5.4 Discussion

Coupled with the work presented in the previous chapters, we can paint the following picture of the acceleration process: The process begins with a large injection of both source (few-10s keV) and seed (10s-100s keV) electrons associated with substorm activity in the outer magnetosphere, impulsively transporting warm (source) and hot (seed) electrons into the inner magnetosphere. These source electrons drive wave growth and these waves resonate with and accelerate the seed population up to ~1 MeV ~10-15 hours after the initial injection. Continued injections of the source population drive further wave growth. These waves then accelerate the ~1 MeV population up to multi-MeV energies. The whole process takes 20-30 hours on average. If any piece of the process is missing, it will not result in multi-MeV electron enhancements. This process is shown in conceptually in Figure 5-8.

This picture of the acceleration process stresses the importance of substorm injections in shaping the outer radiation belt population, which agrees with the work of *Meredith et al.* [2001, 2004] and *Li et al.* [2009]. While this picture does well in describing the acceleration process, we have shown here that the details and timing of this acceleration process can vary greatly event to event. Future work will include also looking at solar wind parameters to investigate how these tie into the acceleration process and influence the results we have shown here.

5.5 Conclusions

The overall goal of this chapter was to extend the discussion beyond the seed population and finish answering the question: *'How do differing inputs of source and seed electrons lead to acceleration (or lack thereof) in the radiation belts?'* To this end, we have three main conclusions:

1. An enhanced seed population, injections of source electrons and chorus wave activity are all necessary to drive acceleration to MeV energies.

2. Continued injection of source electrons is needed to maintain the acceleration process.

3. There are two classes of events:

    - Rapid enhancement driven by a highly enhanced seed population and brief intense injections of source electrons.

    - Slower enhancement driven by a less enhanced seed population and prolonged periods of smaller injections of source electrons.

The work presented here shows definitively that the seed population is only one of the important pieces of the acceleration process that needs to be in place in order to produce MeV electron enhancements.

Chapter 6

Summary & Conclusions

6.1 Overall Summary

The overarching goal of this thesis was to characterize and quantify the importance of the seed population in producing the MeV electrons we see in the radiation belt. This work was made possible in large part due to the observations made by the Van Allen Probes mission. For the first time we have access to clean, simultaneous, multipoint measurements of both the low energy seed electrons and the higher energy >1 MeV core electron populations as well as measurements of the plasma waves responsible for local acceleration. We have used this dataset to calculate phase space densities which we then used to analyze each part of the acceleration process.

The thesis was framed around four focus questions. Each of the chapters addressed one or more of these questions leading to the final question, which guides the future work of implementing the seed population observations presented here to build a predictive model for the radiation belts.

6.2 Focus Questions Revisited

The goal of the first question: 'Is it possible to directly observe and quantify the seed population's role in the acceleration of radiation belt electrons?' was to get clear observations of the seed population's evolution during a radiation belt enhancement event. As mentioned earlier, prior to the Van Allen probes simultaneous observations of the seed and core populations were not readily available. In addition, earlier studies, such as *Reeves et al.* [2013] focused on observations of the multi-MeV electrons. Therefore, observing the seed population in action during a local acceleration event was an important and new observation.

We presented clear observations of the seed population's role in the 17 March 2013 event, showing conclusively that the local acceleration process began with an enhanced seed population that was accelerated up to 1 MeV, then subsequently accelerated up to multi-meV energies. In addition, we quantified the radial gradients of PSD as a function of first invariant μ for the first time inside of geostationary orbit. Our results confirmed the transition at 200 MeV/G between particles originating in the magnetotail and particles with a local source within the belts. Finally, we clearly demonstrated that the PSD at different μ values (or equivalently energy) evolved very differently over the course of the event.

With clear observations from a single event, the next logical step was to look at longer time range to understand the connection between the seed and core populations. This motivated the second question: 'What correlations and causal relationships are there between enhancements in the seed population and enhancements in the core population?'

To address this question we completed the first comprehensive statistical study of the radiation belt seed population. Using data from the first 26 months of the Van Allen Probes mission, we performed a cross correlation analysis between the seed and higher μ populations.

We demonstrated that the seed was strongly correlated up to ∼1 MeV at a 10-15 hour time lag. At higher μ values, the correlation was much weaker, indicating that they were not directly connected to variations in the seed population. These results match with multi-step acceleration process seen in the 17 March 2013 storm.

Along the same vein as the second question, the third question is: 'How do differing inputs of source and seed electrons lead to acceleration (or lack thereof) in the radiation belts?' This question addresses two parts of the acceleration process: the source population that generates the waves and the seed population that is accelerated by the waves. Beginning with the seed population, we showed the first evidence of a seed population threshold. This threshold, which is related to the Kennel-Petschek limit represents the minimum level of seed electrons that must be present to get relativistic electron enhancements. For the the source population, we showed that the acceleration process is only active during injections of the source electrons, and the necessary duration of these injections is related to the strength of the event and the level of the seed population.

The work presented for the first three questions all leads to the final question: 'Can the seed population be used to predict enhancements in the core population?' which serves as the ultimate goal for the work presented in this thesis. While this is not directly addressed in this thesis, the work presented here informs the basic groundwork for building a predictive model. As shown in Figure 5-8, we have developed a clear picture of how this acceleration process evolves. It begins with a large injection of both the source and seed populations. The source electrons provide free energy to drive the growth of VLF chorus waves. These waves then resonate with the enhanced seed population and accelerate the electrons up to ∼1 MeV. This initial stage of the acceleration process takes 10-15 hours. Than, continued injections of the source electrons drive further wave growth. The waves resonate with and

accelerate the enhanced ∼1 MeV electrons up to multi-MeV energize. The entire process, from the initial source injection to the acceleration of multi-MeV electrons takes 20-30 hours. If a piece is missing, then the process breaks down and does not result in the enhancement of multi-MeV electrons.

One of the primary challenges of developing a predictive model would be to capture the dynamics of this complex process using quantifiable parameters. A robust predictive model would need to be build around parameters like AE or consistent particle measurements like those from the GOES spacecraft. As shown in Chapter 5, injections of the source population that drive the wave growth are closely related with substorm activity and it might be possible to develop a parameter based off of AE that quantifies the injection of the source and seed populations. Chorus wave activity could be quantified using a technique like the one outlined in *Li et al.* [2013]. Rather than using measurements from the Van Allen Probes, measurements from the GOES spacecraft or ground based observations could be used to give long lasting reliable inputs to the model. While there is considerable work that needs to be done before such a model is viable, this represents an important path moving forward for the work presented in this thesis.

6.3 Conclusions

Historically, the study of the radiation belts has focused on the dynamics of the >1 MeV electron population. This is understandable, given that these so-called 'killer' electrons are what make the radiation belts an interesting area to study and a dangerous one for satellites to traverse. Consequently, the ultimate goal of radiation belt research has been to understand the system to the point that we can predict the fluxes of >1 MeV electrons.

The work presented in this thesis definitively shows that to accomplish this goal we also need to first understand the dynamics of the lower energy source and seed populations. The work presented here marks some of the first steps towards that understanding and underscores the importance of looking beyond just the relativistic electrons in the radiation belts. Their appearance is the result of a multi-step process that involves waves generated through instabilities in the lower energy electron populations that resonate with and accelerate medium energy electrons.

With the prediction of the MeV fluxes as the ultimate goal, a better understanding of the lower source and seed population is therefore needed, as are the full conditions needed to quantify the strength and location of wave generation. A fundamental outcome of this thesis is a new appreciation and understanding of how these populations play a critical role in the acceleration of higher energy radiation belt electrons.

Bibliography

Allen, J. A. V., and L. A. Frank (1959), Radiation Around the Earth to a Radial Distance of 107,400 km, *Nature*, *183*(4659), 430–434, doi:10.1038/183430a0.

Asnes, A., R. Friedel, J. Stadsnes, M. F. Thomsen, N. Ostgaard, and T. E. Cayton (2005), Statistical pitch angle properties of substorm-injected electron clouds and their relation to dawnside energetic electron precipitation, *J. Geophys. Res.*, *110*(A5), A05,207, doi:10.1029/2004JA010838.

Baker, D., X. Li, N. Turner, J. Allen, L. Bargatze, J. Blake, R. Sheldon, H. Spence, R. Belian, G. Reeves, S. Kanekal, B. Klecker, R. Lepping, K. Ogilvie, R. Mewaldt, T. Onsager, H. Singer, and G. Rostoker (1997), Recurrent geomagnetic storms and relativistic electron enhancements in the outer magnetosphere: ISTP coordinated measurements, *J. Geophys. Res.*, *102*(A7), 14,141, doi:10.1029/97JA00565.

Baker, D., X. Li, J. Blake, and S. Kanekal (1998), Strong electron acceleration in the Earth's magnetosphere, *Adv. Sp. Res.*, *21*(4), 609–613, doi:10.1016/S0273-1177(97)00970-8.

Baker, D. N. (2002), How to Cope with Space Weather., *Science*, *297*(5586), 1486–7, doi:10.1126/science.1074956.

Baker, D. N., and S. G. Kanekal (2008), Solar cycle changes, geomagnetic variations, and energetic particle properties in the inner magnetosphere, *J. Atmos. Solar-Terrestrial Phys.*, *70*(2-4), 195–206, doi:10.1016/j.jastp.2007.08.031.

Baker, D. N., R. D. Belian, P. R. Higbie, and E. W. Hones (1979), High-Energy Magnetospheric Protons and Their Dependence on Geomagnetic and Interplanetary Conditions, *J. Geophys. Res.*, *84*(A12), 7138–7154, doi:10.1029/JA084iA12p07138.

Baker, D. N., S. G. Kanekal, and J. B. Blake (2004), Characterizing the Earth's outer Van Allen zone using a radiation belt content index, *Sp. Weather*, *2*(2), 1–7, doi:10.1029/2003SW000026.

Baker, D. N., S. G. Kanekal, V. C. Hoxie, M. G. Henderson, X. Li, H. E. Spence, S. R. Elkington, R. H. W. Friedel, J. Goldstein, M. K. Hudson, G. D. Reeves, R. M. Thorne, C. A. Kletzing, and S. G. Claudepierre (2013), A long-lived relativistic electron storage ring embedded in Earth's outer Van Allen belt., *Science*, *340*(6129), 186–90, doi:10.1126/science.1233518.

Baker, D. N., A. N. Jaynes, X. Li, M. G. Henderson, S. G. Kanekal, G. D. Reeves, H. E. Spence, S. G. Claudepierre, J. F. Fennell, M. K. Hudson, R. M. Thorne, J. C. Foster, P. J. Erickson, D. M. Malaspina, J. R. Wygant, A. J. Boyd, C. A. Kletzing, A. Drozdov, and Y. Y. Shprits (2014a), Gradual diffusion and punctuated phase space density enhancements of highly relativistic electrons: Van Allen Probes observations, *Geophys. Res. Lett.*, *41*(5), 1351–1358, doi:10.1002/2013GL058942.

Baker, D. N., S. G. Kanekal, V. C. Hoxie, S. Batiste, M. Bolton, X. Li, S. R. Elkington, S. Monk, R. Reukauf, S. Steg, J. Westfall, C. Belting, B. Bolton, D. Braun, B. Cervelli, K. Hubbell, M. Kien, S. Knappmiller, S. Wade, B. Lamprecht, K. Stevens, J. Wallace, A. Yehle, H. E. Spence, and R. Friedel (2014b), The Relativistic Electron-Proton Telescope (REPT) Instrument on Board the Radiation Belt Storm Probes (RBSP) Spacecraft: Characterization of Earth's radiation belt high-energy particle populations, *Van Allen Probes Mission*, *179*(1-4), 337–381, doi:10.1007/978-1-4899-7433-4-11.

Baumjohann, W., and R. A. Treumann (2006), *Basic Space Plasma Physics*, 329 pp., World Scientific.

Blake, J. B., P. A. Carranza, S. G. Claudepierre, J. H. Clemmons, W. R. Crain, Y. Dotan, J. F. Fennell, F. H. Fuentes, R. M. Galvan, J. S. George, M. G. Henderson, M. Lalic, A. Y. Lin, M. D. Looper, D. J. Mabry, J. E. Mazur, B. McCarthy, C. Q. Nguyen, T. P. O'Brien, M. A. Perez, M. T. Redding, J. L. Roeder, D. J. Salvaggio, G. A. Sorensen, H. E. Spence, S. Yi, and M. P. Zakrzewski (2014), The Magnetic Electron Ion Spectrometer (MagEIS) instruments aboard the Radiation Belt Storm Probes (RBSP) spacecraft, *Van Allen Probes Mission*, *9781489974*(1-4), 383–421, doi:10.1007/978-1-4899-7433-4-12.

Boyd, A. J., H. E. Spence, S. G. Claudepierre, J. F. Fennell, J. B. Blake, D. N. Baker, G. D. Reeves, and D. L. Turner (2014), Quantifying the radiation belt seed population in the 17 March 2013 electron acceleration event, *Geophys. Res. Lett.*, *41*(7), 2275–2281, doi:10.1002/2014GL059626.

Chen, Y., R. H. W. Friedel, G. D. Reeves, T. G. Onsager, and M. F. Thomsen (2005), Multisatellite determination of the relativistic electron phase space density at geosynchronous orbit: Methodology and results during geomagnetically quiet times, *J. Geophys. Res.*, *110*(A10210), doi:10.1029/2007JA012314.

Chen, Y., R. H. W. Friedel, G. D. Reeves, T. E. Cayton, and R. Christensen (2007a), Multisatellite determination of the relativistic electron phase space density at geosynchronous orbit: An integrated investigation during geomagnetic storm times, *J. Geophys. Res.*, *112*(11), A10,210, doi:10.1029/2007JA012314.

Chen, Y., G. D. Reeves, and R. H. W. Friedel (2007b), The energization of relativistic electrons in the outer Van Allen radiation belt, *Nat. Phys.*, *3*(9), 614–617, doi:10.1038/nphys655.

Claudepierre, S. G., T. P. O'Brien, J. B. Blake, J. F. Fennell, J. L. Roeder, J. H. Clemmons, M. D. Looper, J. E. Mazur, T. M. Mulligan, H. E. Spence, G. D. Reeves, R. H. W. Friedel, M. G. Henderson, and B. A. Larsen (2015), A background correction algorithm for Van Allen Probes MagEIS electron flux measurements, *J. Geophys. Res.*, *120*(7), 5703–5727, doi:10.1002/2015JA021171.

Fennell, J. F., S. G. Claudepierre, J. B. Blake, T. P. O'Brien, J. H. Clemmons, D. N. Baker, H. E. Spence, and G. D. Reeves (2015), Van Allen Probes show that the inner radiation zone contains no MeV electrons: ECT/MagEIS data, *Geophys. Res. Lett.*, *42*(5), 1283–1289, doi:10.1002/2014GL062874.

Foster, J. C., P. J. Erickson, D. N. Baker, S. G. Claudepierre, C. A. Kletzing, W. Kurth, G. D. Reeves, S. A. Thaller, H. E. Spence, Y. Y. Shprits, and J. R. Wygant (2014), Prompt energization of relativistic and highly relativistic electrons during a substorm interval: Van Allen Probes observations, *Geophys. Res. Lett.*, *41*(1), 20–25, doi:10.1002/2013GL058438.

Foster, J. C., J. R. Wygant, M. K. Hudson, A. J. Boyd, D. N. Baker, P. J. Erickson, and H. E. Spence (2015), Shock-induced prompt relativistic electron acceleration in the inner magnetosphere, *J. Geophys. Res.*, *120*(3), 1661–1674, doi:10.1002/2014JA020642.

Freden, S. C., and R. S. White (1960), Particle fluxes in the inner radiation belt, *J. Geophys. Res.*, *65*(5), 1377–1383, doi:10.1029/JZ065i005p01377.

Friedel, R., G. Reeves, and T. Obara (2002), Relativistic electron dynamics in the inner magnetosphere a review, *J. Atmos. Solar-Terrestrial Phys.*, *64*(2), 265–282, doi:10.1016/S1364-6826(01)00088-8.

Friedel, R. H. W., H. Korth, M. G. Henderson, M. F. Thomsen, and J. D. Scudder (2001), Plasma sheet access to the inner magnetosphere, *J. Geophys. Res.*, *106*(A4), 5845–5858, doi:10.1029/2000JA003011.

Gabrielse, C., V. Angelopoulos, A. Runov, and D. L. Turner (2014), Statistical characteristics of particle injections throughout the equatorial magnetotail, *J. Geophys. Res.*, *119*(4), 2512–2535, doi:10.1002/2013JA019638.

Goldstein, H. (1959), *Classical Mechanics*, Addison-Wesley, Reading, MA, doi:10.1063/1.3057243.

Green, J. C., and M. G. Kivelson (2004), Relativistic electrons in the outer radiation belt: Differentiating between acceleration mechanisms, *J. Geophys. Res.*, *109*(A3), A03,213, doi:10.1029/2003JA010153.

Henderson, M., S. K. Morley, and B. A. Larsen (2011), LanlGeoMag 1.5.13 - LA-CC-11-104, Tech. rep., *Tech. rep.*, Los Alamos National Labratory, Los Alamos, NM.

Hilmer, R. V., G. P. Ginet, and T. E. Cayton (2000), Enhancement of equatorial energetic electron fluxes near L= 4.2 as a result of high speed solar wind streams, *J. Geophys. Res*, *105*(A10), 23,311, doi:10.1029/1999JA000380.

Horne, R. B., and R. M. Thorne (1998), Potential waves for relativistic electron scattering and stochastic acceleration during magnetic storms, *Geophys. Res. Lett.*, *25*(15), 3011, doi:10.1029/98GL01002.

Horne, R. B., R. M. Thorne, Y. Y. Shprits, N. P. Meredith, S. a. Glauert, A. J. Smith, S. G. Kanekal, D. N. Baker, M. J. Engebretson, J. L. Posch, M. Spasojevic, U. S. Inan, J. S. Pickett, and P. M. E. Decreau (2005), Wave acceleration of electrons in the Van Allen radiation belts, *Nature*, *437*(7056), 227–230, doi:10.1038/nature03939.

Huang, C.-L., H. Spence, A. Boyd, A. Jordan, L. Chen, Y. Zheng, G. Reeves, J. B. Blake, D. Baker, and Y. Shprits (2016), Spatial, Temporal and Energy Dependence of the Total Radiation Belt Electron Content, *Geophys. Res. Lett.*, (in preparation).

Hudson, M. K., J. Paral, B. T. Kress, M. Wiltberger, D. N. Baker, J. C. Foster, D. L. Turner, and J. R. Wygant (2015), Modeling CME-shock-driven storms in 2012-2013: MHD test particle simulations, *J. Geophys. Res.*, *120*(2), 1168–1181, doi:10.1002/2014JA020833.

Iles, R. H. A., N. P. Meredith, A. N. Fazakerley, and R. B. Horne (2006), Phase space density analysis of the outer radiation belt energetic electron dynamics, *J. Geophys. Res.*, *111*(A3), 1–15, doi:10.1029/2005JA011206.

Jaynes, A. N., D. N. Baker, H. J. Singer, J. V. Rodriguez, T. M. Loto'aniu, a. F. Ali, S. R. Elkington, X. Li, S. G. Kanekal, J. F. Fennell, W. Li, R. M. Thorne, C. A. Kletzing, H. E. Spence, and G. D. Reeves (2015), Source and seed populations for relativistic electrons: Their roles in radiation belt changes, *J. Geophys. Res.*, *120*(9), 7240–7254, doi:10.1002/2015JA021234.

Kennel, C. F., and H. E. Petschek (1966), Limit on stably trapped particle fluxes., *J. Geophys. Res.*, *71*(1), 1–28, doi:10.1029/JZ071i001p00001.

Kim, H. J., E. Zesta, K. C. Kim, Y. Shprits, Y. Shi, and L. R. Lyons (2010), Estimation of radial gradients of phase space density from POLAR observations during a quiet period prior to a sudden solar wind dynamic pressure enhancement, *J. Geophys. Res.*, *115*(12), 1–9, doi:10.1029/2010JA015722.

Kletzing, C. A., W. S. Kurth, M. Acuna, R. J. MacDowall, R. B. Torbert, T. Averkamp, D. Bodet, S. R. Bounds, M. Chutter, J. Connerney, D. Crawford, J. S. Dolan, R. Dvorsky, G. B. Hospodarsky, J. Howard, V. Jordanova, R. a. Johnson, D. L. Kirchner, B. Mokrzycki, G. Needell, J. Odom, D. Mark, R. Pfaff, J. R. Phillips, C. W. Piker, S. L. Remington, D. Rowland, O. Santolik, R. Schnurr, D. Sheppard, C. W. Smith, R. M. Thorne, and J. Tyler (2013), The Electric and Magnetic Field Instrument suite and Integrated Science (EMFISIS) on RBSP, *Van Allen Probes Mission*, *179*(1), 127–181, doi:10.1007/978-1-4899-7433-4-5.

Lanzerotti, L. (2001), Space weather effects on communications, in *Sp. storms Sp. Weather hazards*, edited by P. Song, H. J. Singer, and G. L. Siscoe, Geophysical Monograph Series, American Geophysical Union, Washington, D. C., doi:10.1007/978-3-540-34578-7_9.

Li, L. Y., J. B. Cao, G. C. Zhou, and X. Li (2009), Statistical roles of storms and substorms in changing the entire outer zone relativistic electron population, *J. Geophys. Res.*, *114*(A12), A12,214, doi:10.1029/2009JA014333.

Li, W., B. Ni, R. M. Thorne, J. Bortnik, J. C. Green, C. a. Kletzing, W. S. Kurth, and G. B. Hospodarsky (2013), Constructing the global distribution of chorus wave intensity using measurements of electrons by the POES satellites and waves by the Van Allen Probes, *Geophys. Res. Lett.*, *40*(17), 4526–4532, doi:10.1002/grl.50920.

Li, X., I. Roth, M. Temerin, J. R. Wygant, M. K. Hudson, and J. B. Blake (1993), Simulation of the prompt energization and transport of radiation belt particles during the March 24, 1991 SSC, *Geophys. Res. Lett.*, *20*(22), 2423–2426, doi:10.1029/93GL02701.

Li, X., D. N. Baker, M. Temerin, T. E. Cayton, E. G. D. Reeves, R. a. Christensen, J. B. Blake, M. D. Looper, R. Nakamura, and S. G. Kanekal (1997), Multisatellite observations of the outer zone electron variation during the November 34, 1993, magnetic storm, *J. Geophys. Res.*, *102*(A7), 14,123–14,140, doi:10.1029/97JA01101.

Li, X., D. N. Baker, M. Temerin, G. D. Reeves, R. H. Friedel, and C. Shen (2005), Energetic electrons, 50 keV to 6 MeV, at geosynchronous orbit: Their responses to solar wind variations, *Sp. Weather*, *3*(4), 1–10, doi:10.1029/2004SW000105.

Li, X., M. Temerin, D. N. Baker, and G. D. Reeves (2011), Behavior of MeV electrons at geosynchronous orbit during last two solar cycles, *J. Geophys. Res.*, *116*(11), A11,207, doi:10.1029/2011JA016934.

Li, Z., M. Hudson, A. Jaynes, A. Boyd, D. Malaspina, S. Thaller, J. Wygant, and M. Henderson (2014), Modeling gradual diffusion changes in radiation belt electron phase space density for the March 2013 Van Allen Probes case study, *J. Geophys. Res.*, *119*(10), 8396–8403, doi:10.1002/2014JA020359.

Lorentzen, K. R., M. D. Looper, and J. B. Blake (2001), Relativistic electron microbursts during the GEM storms, *Geophys. Res. Lett.*, *28*(13), 2573–2576, doi:10.1029/2001GL012926.

Lyons, L. R., and R. M. Thorne (1972), Parasitic pitch angle diffusion of radiation belt particles by ion cyclotron waves, *J. Geophys. Res.*, *77*(28), 5608–5616, doi:10.1029/JA077i028p05608.

Mann, I. R., T. P. O'Brien, and D. K. Milling (2004), Correlations between ULF wave power, solar wind speed, and relativistic electron flux in the magnetosphere: Solar cycle dependence, *J. Atmos. Solar-Terrestrial Phys.*, *66*(2), 187–198, doi:10.1016/j.jastp.2003.10.002.

Mauk, B. H., N. J. Fox, S. G. Kanekal, R. L. Kessel, D. G. Sibeck, and A. Ukhorskiy (2014), Science objectives and rationale for the Radiation Belt Storm Probes mission, *Van Allen Probes Mission*, *179*(1), 3–27, doi:10.1007/978-1-4899-7433-4-2.

Mazur, J., L. Friesen, A. Lin, D. Mabry, N. Katz, Y. Dotan, J. George, J. B. Blake, M. Looper, M. Redding, T. P. O'Brien, J. Cha, A. Birkitt, P. Carranza, M. Lalic, F. Fuentes, R. Galvan, and M. McNab (2013), The Relativistic Proton Spectrometer (RPS) for the Radiation Belt Storm Probes mission, *Van Allen Probes Mission*, *179*(1), 221–261, doi:10.1007/978-1-4899-7433-4-7.

Menk, F. W. (2011), *The Dynamic Magnetosphere*, chap. Magnetosph, pp. 223–256, Springer Netherlands, Dordrecht, doi:10.1007/978-94-007-0501-2_13.

Meredith, N. P., R. B. Horne, R. R. Anderson, and B. Horne (2001), Substorm dependence of chorus amplitudes: Implications for the acceleration of electrons to relativistic energies, *J. Geophys. Res.*, *106*(A7), 13,165, doi:10.1029/2000JA900156.

Meredith, N. P., R. B. Horne, R. H. A. Iles, R. M. Thorne, D. Heynderickx, and R. R. Anderson (2002), Outer zone relativistic electron acceleration associated with substorm-enhanced whistler mode chorus, *J. Geophys. Res.*, *107*(A7), 1144, doi: 10.1029/2001JA900146.

Meredith, N. P., R. B. Horne, R. M. Thorne, D. Summers, and R. R. Anderson (2004), Substorm dependence of plasmaspheric hiss, *J. Geophys. Res.*, *109*(A6), A06,209, doi: 10.1029/2004JA010387.

Millan, R. M., and R. M. Thorne (2007), Review of radiation belt relativistic electron losses, *J. Atmos. Solar-Terrestrial Phys.*, *69*(3), 362–377, doi:10.1016/j.jastp.2006.06.019.

Mitchell, D. G., L. J. Lanzerotti, C. K. Kim, M. Stokes, G. Ho, S. Cooper, A. Ukhorskiy, J. W. Manweiler, S. Jaskulek, D. K. Haggerty, P. Brandt, M. Sitnov, K. Keika, J. R. Hayes, L. E. Brown, R. S. Gurnee, J. C. Hutcheson, K. S. Nelson, N. Paschalidis, E. Rossano, and S. Kerem (2013), Radiation Belt Storm Probes Ion Composition Experiment (RBSPICE), *Van Allen Probes Mission*, *179*(1), 263–308, doi:10.1007/978-1-4899-7433-4-8.

Morley, S. K., M. G. Henderson, G. D. Reeves, R. H. W. Friedel, and D. N. Baker (2013), Phase Space Density matching of relativistic electrons using the Van Allen Probes: REPT results, *Geophys. Res. Lett.*, *40*(18), 4798–4802, doi:10.1002/grl.50909.

O'Brien, T. P., R. L. McPherron, D. Sornette, G. D. Reeves, R. Friedel, and H. J. Singer (2001), Which magnetic storms produce relativistic electrons at geosynchronous orbit?, *J. Geophys. Res.*, *106*(A8), 15,533, doi:10.1029/2001JA000052.

Ozeke, L. G., and I. R. Mann (2008), Energization of radiation belt electrons by ring current ion driven ULF waves, *J. Geophys. Res.*, *113*(A2), A02,201, doi:10.1029/2007JA012468.

Paulikas, G. A., and J. B. Blake (1979), *Quantitative Modeling of Magnetospheric Processes*, *Geophysical Monograph Series*, vol. 21, American Geophysical Union, Washington, D. C., doi:10.1029/GM021.

Piel, A. (2011), *Plasma Physics - An Introduction to Laboratory, Space, and Fusion Plasmas*, 398 pp., Springer Science & Business Media, doi:10.1007/SpringerReference_72.

Reeves, G. D., K. L. McAdams, R. H. W. Friedel, and T. P. O'Brien (2003), Acceleration and loss of relativistic electrons during geomagnetic storms, *Geophys. Res. Lett.*, *30*(10), doi:10.1029/2002GL016513.

Reeves, G. D., H. E. Spence, M. G. Henderson, S. K. Morley, R. H. W. Friedel, H. O. Funsten, D. N. Baker, S. G. Kanekal, J. B. Blake, J. F. Fennell, S. G. Claudepierre, R. M. Thorne, D. L. Turner, C. A. Kletzing, W. S. Kurth, B. A. Larsen, and J. T. Niehof (2013), Electron acceleration in the heart of the Van Allen radiation belts., *Science*, *341*(6149), 991–4, doi:10.1126/science.1237743.

Roederer, J. G. G. (1970), *Dynamics of geomagnetically trapped radiation*, *Physics and Chemistry in Space*, vol. 2, 187 pp., Springer Berlin Heidelberg, Berlin, Heidelberg, doi: 10.1007/978-3-642-49300-3.

Rostoker, G., S. Skone, and D. N. Baker (1998), On the origin of relativistic electrons in the magnetosphere associated with some geomagnetic storms, *Geophys. Res. Lett.*, *25*(19), 3701, doi:10.1029/98GL02801.

Schulz, M., and G. Davidson (1988), Limiting energy spectrum of an electron radiation belt, *J. Geophys. Res.*, *93*(A1), 59–76, doi:10.1002/2014JA020250.

Schulz, M., and L. Lanzerotti (1974), *Particle Diffusion in the Radiation Belts*, *Physics and Chemistry in Space*, vol. 9, 368–369 pp., Springer Berlin Heidelberg, Berlin, Heidelberg, doi:10.1016/0031-9201(74)90066-1.

Selesnick, R. S., and J. B. Blake (1997), Dynamics of the outer radiation belt, *Geophys. Res. Lett.*, *24*(11), 1347, doi:10.1029/97GL51409.

Selesnick, R. S., and S. G. Kanekal (2009), Variability of the total radiation belt electron content, *J. Geophys. Res.*, *114*(2), A02,203, doi:10.1029/2008JA013432.

Selesnick, R. S., J. B. Blake, W. A. Kolasinski, and T. A. Fritz (1997), A quiescent state of 3 to 8 MeV radiation belt electrons, *Geophys. Res. Lett*, *24*(11), 1343–1346, doi: 10.1029/97GL51407.

Shprits, Y. Y., R. M. Thorne, R. Friedel, G. D. Reeves, J. Fennell, D. N. Baker, and S. G. Kanekal (2006), Outward radial diffusion driven by losses at magnetopause, *J. Geophys. Res.*, *111*(11), 11,214, doi:10.1029/2006JA011657.

Shue, J.-H., P. Song, C. T. Russell, J. T. Steinberg, J. K. Chao, G. Zastenker, O. L. Vaisberg, S. Kokubun, H. J. Singer, T. R. Detman, and H. Kawano (1998), Magnetopause location under extreme solar wind conditions, *J. Geophys. Res.*, *103*(A8), 17,691–17,700, doi:10.1029/98JA01103.

Southwood, D. J., and M. G. Kivelson (1981), Charged particle behavior in low-frequency geomagnetic pulsations 1. Transverse waves, *J. Geophys. Res.*, *86*(A7), 5643, doi: 10.1029/JA086iA07p05643.

Spence, H., A. J. Boyd, C. Huang, S. S. Smith, M. G. Henderson, R. H. Friedel, B. Larsen, G. D. Reeves, J. B. Blake, S. G. Claudepierre, J. F. Fennell, D. N. Baker, and S. G. Kanekal (2013a), Estimates of Total Radiation Belt Electron Content (TRBEC) and its Time Evolution using the RBSP-ECT Instrument Suite on the Van Allen Probes Mission, *AGU Fall Meet. Abstr.*, p. 01.

Spence, H. E., G. D. Reeves, D. N. Baker, J. B. Blake, M. Bolton, S. Bourdarie, a. a. Chan, S. G. Claudepierre, J. H. Clemmons, J. P. Cravens, S. R. Elkington, J. F. Fennell, R. H. W. Friedel, H. O. Funsten, J. Goldstein, J. C. Green, A. Guthrie, M. G. Henderson, R. B. Horne, M. K. Hudson, J. M. Jahn, V. K. Jordanova, S. G. Kanekal, B. W. Klatt, B. a. Larsen, X. Li, E. a. MacDonald, I. R. Mann, J. Niehof, T. P. O'Brien, T. G. Onsager, D. Salvaggio, R. M. Skoug, S. S. Smith, L. L. Suther, M. F. Thomsen, and R. M. Thorne (2013b), Science goals and overview of the Radiation Belt Storm Probes (RBSP) Energetic Particle, Composition, and Thermal Plasma (ECT) suite on NASA's Van Allen Probes mission, doi:10.1007/978-1-4899-7433-4-10.

Summers, D., C. Ma, N. P. Meredith, R. B. Horne, R. M. Thorne, D. Heynderickx, and R. R. Anderson (2002), Model of the energization of outer-zone electrons by whistler-mode chorus during the October 9, 1990 geomagnetic storm, *Geophys. Res. Lett.*, *29*(24), 2174, doi:10.1029/2002GL016039.

Summers, D., B. Ni, and N. P. Meredith (2007), Timescales for radiation belt electron acceleration and loss due to resonant wave-particle interactions: 2. Evaluation for VLF chorus, ELF hiss, and electromagnetic ion cyclotron waves, *J. Geophys. Res.*, *112*(4), 1–21, doi:10.1029/2006JA011993.

Temerin, M., I. Roth, M. K. Hudson, and J. R. Wygant (1994), New paradigm for the transport and energization of radiation belt particles, *Eos Trans. AGU*, *75*(75), 538.

Thorne, R. M. (2010), Radiation belt dynamics: The importance of wave-particle interactions, *Geophys. Res. Lett.*, *37*(22), n/a–n/a, doi:10.1029/2010GL044990.

Thorne, R. M., and C. F. Kennel (2012), Relativistic electron precipitation during magnetic storm main phase, *J. Geophys. Res*, *76*(19), 4446–4453, doi:10.1029/JA076i019p04446.

Thorne, R. M., S. R. Church, W. J. Malloy, and B. T. Tsurutani (1977), The local time variation of ELF emissions during periods of substorm activity, *J. Geophys. Res.*, *82*(10), 1585–1590, doi:10.1029/JA082i010p01585.

Thorne, R. M., T. P. O'Brien, Y. Y. Shprits, D. Summers, and R. B. Horne (2005), Timescale for MeV electron microburst loss during geomagnetic storms, *J. Geophys. Res.*, *110*(A9), 9202, doi:10.1029/2004JA010882.

Thorne, R. M., W. Li, B. Ni, Q. Ma, J. Bortnik, L. Chen, D. N. Baker, H. E. Spence, G. D. Reeves, M. G. Henderson, C. a. Kletzing, W. S. Kurth, G. B. Hospodarsky, J. B. Blake, J. F. Fennell, S. G. Claudepierre, and S. G. Kanekal (2013), Rapid local acceleration of relativistic radiation-belt electrons by magnetospheric chorus, *Nature*, *504*(7480), 411–414, doi:10.1038/nature12889.

Tsurutani, B. T., and G. S. Lakhina (1997), Some basic concepts of wave-particle interactions in collisionless plasmas, *Rev. Geophys.*, *35*(4), 491, doi:10.1029/97RG02200.

Tsurutani, B. T., and E. J. Smith (1974), Postmidnight Chorus ' A Substorm Phenomenon, *J. Geophys. Res.*, *79*(1), 118–127, doi:10.1029/JA079i001p00118.

Tsyganenko, N. A., and M. I. Sitnov (2005), Modeling the dynamics of the inner magnetosphere during strong geomagnetic storms, *J. Geophys. Res.*, *110*(A3), A03,208, doi:10.1029/2004JA010798.

Turner, D. L., and X. Li (2008), Radial gradients of phase space density of the outer radiation belt electrons prior to sudden solar wind pressure enhancements, *Geophys. Res. Lett.*, *35*(18), 1–5, doi:10.1029/2008GL034866.

Turner, D. L., V. Angelopoulos, Y. Shprits, a. Kellerman, P. Cruce, and D. Larson (2012), Radial distributions of equatorial phase space density for outer radiation belt electrons, *Geophys. Res. Lett.*, *39*(9), 1–7, doi:10.1029/2012GL051722.

Ukhorskiy, A. Y., K. Takahashi, B. J. Anderson, and H. Korth (2005), Impact of toroidal ULF waves on the outer radiation belt electrons, *J. Geophys. Res.*, *110*(A10), 1–12, doi:10.1029/2005JA011017.

Wygant, J. R., J. W. Bonnell, K. Goetz, R. E. Ergun, F. S. Mozer, S. D. Bale, M. Ludlam, P. Turin, P. R. Harvey, R. Hochmann, K. Harps, G. Dalton, J. McCauley, W. Rachelson, D. Gordon, B. Donakowski, C. Shultz, C. Smith, M. Diaz-Aguado, J. Fischer, S. Heavner, P. Berg, D. M. Malsapina, M. K. Bolton, M. Hudson, R. J. Strangeway, D. N. Baker, X. Li, J. Albert, J. C. Foster, C. C. Chaston, I. Mann, E. Donovan, C. M. Cully, C. A. Cattell, V. Krasnoselskikh, K. Kersten, A. Brenneman, and J. B. Tao (2013), The Electric Field and Waves Instruments on the Radiation Belt Storm Probes mission, *Van Allen Probes Mission*, *179*(1), 183–220, doi:10.1007/978-1-4899-7433-4-6.